Development of Quantum Dots as Biosensing Probes

UNDERGRADUATE HONORS RESEARCH THESIS

Presented in Partial Fulfillment of the Requirements for the Bachelor of Science with Honors Research Distinction in the College of Engineering of The Ohio State University

By

Thomas Koizumi Porter

The Ohio State University

April 2020

Honors Thesis Committee

Dr. Jessica Winter, Advisor

Dr. Nicholas Brunelli

Copyrighted by

Thomas Koizumi Porter

2020

Abstract

Quantum dots (QDs) are semiconductor nanoparticles that exhibit size-dependent optical properties. Compared to other common fluorophores such as dyes and fluorescent proteins, QDs possess higher photon emission rates. Additionally, they have broad absorption spectra and narrow, size-tunable emission spectra that enable color multiplexing. Their resistance to photobleaching also makes them suitable for tracking over long periods of time. Thus, QDs possess numerous properties that make them attractive for biosensing applications. However, several concerns must be addressed for their widespread implementation in sensing applications. For instance, the most common QDs contain cadmium, raising concerns of toxicity. Additionally, several groups anecdotally report decreases in fluorescence intensity during QD processing. The research described in this document explores several aspects of these difficulties, including a toxicity characterization of QDs made of alternative nontoxic materials with various surface chemistries. Further, a systematic analysis of QD colloidal stability and fluorescence loss during common processing steps such as dilution, centrifugal filtration, and buffer exchange is discussed. After addressing these difficulties, the utility of QDs are demonstrated in a novel magneto-fluorescent detection and separation platform used on protein and DNA analytes. Finally, the development of novel QD-DNA conjugates and the wide-reaching potential applications of these QD-DNA conjugates are discussed.

Acknowledgments

I wish to first express my deepest gratitude to my advisor, Dr. Jessica O. Winter. She is one of the most inspiring people I have had the pleasure of knowing; I have never been more motivated by anyone even prior to meeting them. Over the past three years, I have been continually impressed by her vast knowledge and skills on a variety of topics, and paying meticulous attention to her comments and work has allowed me to grow significantly. She has always helped me strive for my goals in every way possible, and has helped me pursue opportunities that I could not have previously fathomed.

I would like to thank all members of the Winter Lab during my time at Ohio State. They helped me generate ideas through discussions, and had everlasting patience for me while offering advice on any topics I had concerns about. I would like to specially thank Dr. Abhilasha Dehankar for serving as my primary mentor, helping me grow tremendously as a researcher while putting up with all my mistakes and answering my barrages of questions. I would also like to specially thank Dr. Kil Ho Lee for being a wonderful mentor to me and going out of his way to make sure I was staying on track in all aspects of life.

I would like to thank my research funding: NSF DBI-1555470, as well as several foundations and scholarships that funded my undergraduate studies: Maximus Scholarship, Second-Year Transformational Experience Program, William I. Burt Memorial Scholarship, Ohio House of Science and Engineering Choose Ohio First Scholarship,

Undergraduate Research Scholarship, Amgen Foundation, Barry Goldwater Scholarship and Excellence in Education Foundation, Department of Defense National Defense Education Programs, and Astronaut Scholarship Foundation.

I would like to thank the members of the Joshi Lab (now at Northeastern University), especially Dr. Anton Kan and Dr. Neel Joshi, who hosted me over the summer of 2019, helping me learn about a new field and develop as a researcher.

I would like to thank Dr. Barbara Wyslouzil, Dr. Li-Chiang Lin, and Dr. Nicholas Brunelli for their advice and discussions on topics ranging from life to graduate school and research.

I would also like to thank Dr. Nicholas Brunelli for serving on my thesis committee.

I would like to thank my parents, Chiaki and Stephen Porter, for their unwavering belief and support for me, and my brother Michael Porter for listening to my troubles and always offering me advice from the perspective of an older chemical engineering student.

Finally, I'd like to thank Kei Nishikori for being a constant source of inspiration!

Vita

May 2017-2020.....Undergraduate Research Assistant,
The Ohio State University

June 2019-August 2019.....Amgen Scholar,
Harvard University

May 2020.....B.S. Chemical Engineering,
The Ohio State University

Publications

3. Mahajan KD, Ruan G, Vieira G, Porter T, Chalmers JJ, Sooryakumar R, Winter JO, "Biomolecular Detection, Tracking, and Manipulation using a Magnetic Nanoparticle-Quantum Dot Platform." J. Mater. Chem. B, (2020).

2. Dehankar A*, Porter T*, Johnson JA, Castro CE, Winter JO, (Invited) "Compact Quantum Dot Surface Modification to Enable Emergent Behaviors in Quantum Dot-DNA composites." J. Chem. Phys., 151(14) (2019).

1. Lee KH*, Porter T*, Winter JO, "Fluorescence Loss of Commercial Aqueous Quantum Dots During Preparation for Bioimaging." MRS Communications, 9(2), 702-709 (2019).

* Equally contributing authors.

Fields of Study

Major Field: Chemical and Biomolecular Engineering

Minor Field: Chemistry

Table of Contents

List of Tables

List of Figures

Chapter 1. Introduction

This chapter presents a brief overview of quantum dots, their properties, and the steps needed to prepare them for biological applications.

Quantum Dots – Size Dependent Properties

Quantum dots (QDs) are semiconductor nanoparticles with sizes typically on the order of 1-20 nm.[1] Upon excitation with ultraviolet light, QDs exhibit a size-dependent fluorescence emission, giving them broad utility in sensing applications. As photon absorption occurs, electrons are excited from the valence band to the conduction band, resulting in the formation of an exciton. The recombination of this electron-hole pair can result in energy release in the form of fluorescence.[2]

The size dependence of QD emission is a result of the electronic energy band spacing. Starting with a single atom, electrons occupy atomic orbitals of discrete energy levels. In a nanocluster, where several atoms interact with each other, atomic orbitals split into molecular orbitals that must have different energies according to the Pauli exclusion principle. When enough atoms are interacting as part of a solid, the density of states forms a continuous band, characteristic of bulk materials (Figure 1). Lying at an intermediate size range are nano-sized solids, which have quantized bands that cause them to exhibit behaviors characteristic of both atomic and bulk materials. These bands are centered

around atomic energy levels and first develop in the center, with edges developing last.[3] For semiconductors, where the Fermi level lies between the valence and conduction bands, the band edges dominate electronic energy transitions. Therefore, electronic and optical properties are strongly dependent on the size (number of atoms) of the cluster, as atoms in larger clusters have stronger nearest neighbor interactions that increase the width of the bands.[3]

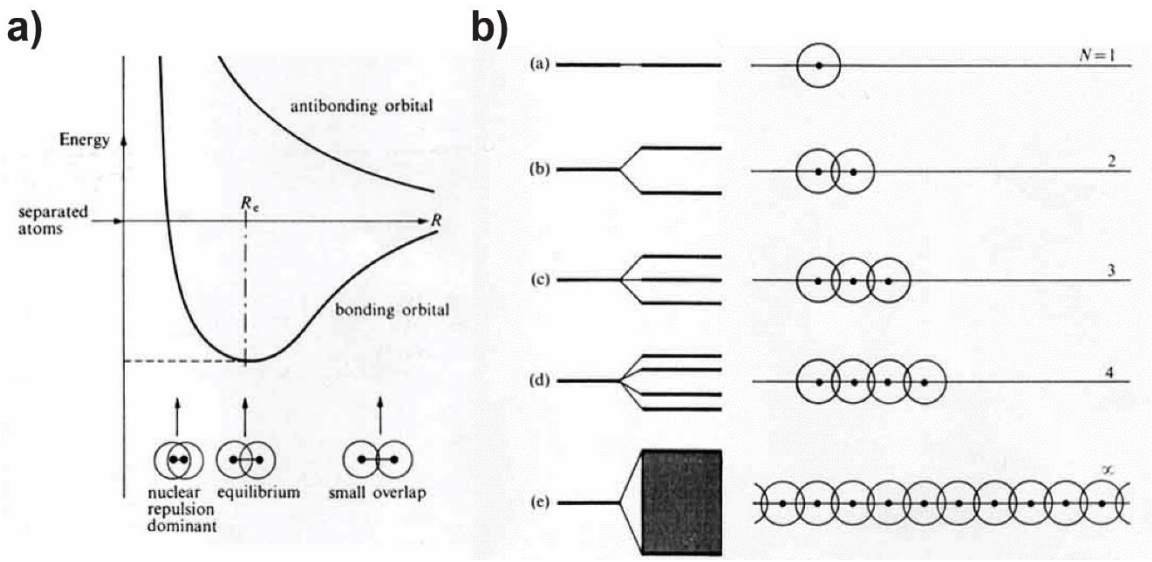

Figure 1 (a) Interaction energy between two atoms as a function of separation distance. (b) As the number of atoms in a cluster increases, the energy states develop into continuous bands. Figure reproduced from Owens and Poole 2008.[4]

Quantum confinement effects, which occur when the size of a QD is less than the Bohr diameter, result in the oscillator strength (transition probability) being concentrated into just a few transitions. Additionally, quantum confinement effects yield higher energy

electronic transitions.[3] Higher energy transitions for quantum confined systems can be explained by the increased binding energy of electron-hole pairs. In a confined system, the exciton size is limited by the QD size. This means that the electron-hole pair is squeezed, resulting in a higher coulombic attraction force.[5] Bandgap widening can be seen using an approximation where a quantum dot can be considered as a box with zero potential inside the box and infinite potential outside the box (particle in a box). The energy spectrum is then given by Equation 1.1

$$E_{n_1,n_2,n_3} = \frac{\hbar^2\pi^2}{2m_e^*}\left(\frac{n_1^2}{a_x^2} + \frac{n_2^2}{a_y^2} + \frac{n_3^2}{a_z^2}\right), n_1, n_2, n_3 = 1,2,3, \ldots \qquad \text{Equation 1.1}$$

Where a_x, a_y, a_z are the dimensions of the box.[5] Evidently, bandgap widening is observed with decreasing particle size.

Quantum Dot Synthesis

For application in biological systems, QDs must be water soluble. The first established QD synthesis methods were entirely aqueous, where salts of the QD components are simply mixed together in the presence of a capping ligand.[6] This is known as the arrested precipitation method. The advantages of this method are that the QDs are already in aqueous phase, and the simplicity of this method lends itself to scalability. However, this method yields highly polydisperse particles with many defects, resulting in poor optical properties (i.e., low quantum yield, broad emission spectra). Today, the most common approach for QD synthesis is known as high temperature precursor decomposition. In this approach, organometallic precursors are heated until they decompose into reactive ions. The precursors are all added together at once with a coordinating ligand, resulting in an

instantaneous nucleation followed by growth via controlled Ostwald ripening. This instantaneous nucleation yields a monodisperse population of nanoparticles with a narrow emission bandwidth.[7] However, QDs prepared via high temperature precursor decomposition must undergo subsequent surface modifications for aqueous phase transfer if biological applications are desired.

CdSe group II-VI QDs are the most common QD core material. However, CdSe nanoparticles alone have low quantum yields (~10%).[2] To overcome this, different capping materials can be grown as a shell around the core to form a core-shell structure.[8] The synthesis of the shell is similar to the core synthesis, where organometallic precursors are injected at a high temperature and grown over top of the cores. If the shell material is a semiconductor with a wider bandgap than the core material (classified as a type-I core-shell structure), enhancement of optical properties is observed. For example, with CdSe/ZnS QDs, quantum yield increases to about 40-50% compared to CdSe alone.[2] In this type of structure, the electrons and holes are confined in the core, and the shell serves to passivate the surface of the core. One effect of the shell is to physically separate the core of the QD (where radiative excitonic recombination is occurring) from the surrounding environment, minimizing interactions such as oxidation that can be detrimental to the optical properties. Additionally, trap states resulting from surface defects and dangling bonds at the surface of the core are reduced, improving quantum yield. Besides quantum yield, other optical properties of the QDs are not significantly changed. Typically, a red shift of about 5-10 nm in the absorbance and emission peaks is observed.[9]

There are a few other important considerations for synthesizing core-shell QDs. For example, when choosing shell materials, the core and shell must crystallize in the same structure but have a small lattice mismatch for epitaxial growth to occur. Additionally, the thickness of the shell must be well controlled. A shell that is too thin does not passivate the surface well. However, a shell that is too thick can generate trap states because of lattice strain resulting from the lattice mismatch with the core.[9]

Post-Synthesis Modifications of Quantum Dots

As mentioned previously, the highest quality QDs are synthesized in organic phase. Thus, one of the first steps in developing QD biosensors is to modify the surface chemistry of the QDs to make them water soluble. There are three common strategies to do this.[10] In one method, known as ligand exchange, the original hydrophobic ligand is substituted with a higher affinity ligand containing a hydrophilic end group that faces outward from the particle. Thiol ligands are commonly used for this strategy.[11] In another approach, a silica shell is grown on top of the QD and the surface can be subsequently modified for different applications.[12] The last general method for QD water solubilization is polymer encapsulation, where QDs are either encapsulated in micelles or hydrophobic polymers derivatized with hydrophilic groups interdigitate with the original QD ligand.[13]

Following aqueous phase transfer, QD surface chemistry is often further modified to enable targeting to specific analytes. Although the specific surface modification varies widely depending on the desired application, several common general conjugation schemes are typically employed. In some cases, electrostatic adsorption of proteins to charged QD surfaces has been used for surface modification.[14] In many other cases, however,

biomolecules are covalently linked to QDs using bioconjugation chemistries. For example, carbodiimide crosslinker chemistry crosslinks carboxylic acids and primary amines to form amide bonds. This approach, although low yielding (<30%), is frequently used for antibody and other protein conjugation schemes. Other common functional groups used in crosslinking include amine-reactive N-hydroxysuccinimide ester groups and sulfhydryl-reactive maleimide groups.[15] More recently, copper-free click chemistry has been used in QD bioconjugation methods because of its high yields (~67%) and reaction specificity.[13] However, click chemistry functional groups typically must first be conjugated via previously mentioned approaches. Even so, reaction yields are often higher in the multi-step click chemistry approach because the small molecules containing click chemistry functional groups are easier to conjugate than larger protein and DNA molecules.

Motivation – QDs in Biosensing Applications

Overall, QDs exhibit a number of useful optical properties for sensing applications that are unique from other fluorophores such as organic dyes and fluorescent proteins. For instance, they have much higher absorbance cross sections, enabling higher photon emission rates that can improve signal-to-noise ratio. The broad absorption spectra and narrow, tunable emission spectra of QDs lend them to multiplexing, as several QDs with distinguishable emission wavelengths can be simultaneously excited with the same wavelength. Additionally, QDs are stable against photobleaching, making them useful for real-time monitoring of processes that occur over longer timescales.[13]

However, several difficulties remain that limit the potential applications of QDs. For example, the most well-studied QDs are cadmium based, and cadmium ions are known to

have several toxic effects in biological systems.[16] In Chapter 2, QDs synthesized from nontoxic alternative materials are discussed, with a focus on toxicity characterization. Next, in Chapter 3, the difficulties of QD fluorescence loss during common preparation steps for biological applications is discussed, using data from QDs of several different vendors to highlight the universality of these problems. In Chapter 4, methods of QD sensing are discussed, and a magneto-fluorescent detection and separation platform for DNA and protein analytes is described. Finally, Chapter 5 describes a conjugation scheme for compact QD-DNA systems with applications in sensing based on fluorescence resonance energy transfer. Conclusions and the future directions building off the work from Chapter 5 are discussed in Chapter 6.

References

1. Murray, C. B., Kagan, C. R. & Bawendi, M. G. Synthesis and Characterization of Monodisperse Nanocrystals and Close-Packed Nanocrystal Assemblies. *Annu. Rev. Mater. Sci.* **30**, 545–610 (2000).
2. Chan, W. C. W. *et al.* Luminescent quantum dots for multiplexed biological detection and imaging. *Current Opinion in Biotechnology* **13**, 40–46 (2002).
3. Alivisatos, A. P. Semiconductor clusters, nanocrystals, and quantum dots. *Science (80-.).* **271**, 933–937 (1996).
4. Owens, F. J. & Poole, C. P. *The Physics and Chemistry of Nanosolids*. (John Wiley & Sons, 2008).
5. Martínez-Duart, J. M., Martín-Palma, R. J. & Agulló-Rueda, F. *Nanotechnology for Microelectronics and Optoelectronics*. *Nanotechnology for Microelectronics and Optoelectronics* (Elsevier Inc., 2006). doi:10.1016/B978-0-08-044553-3.X5000-0
6. Kalyanasundaram, K., Borgarello, E., Duonghong, D. & Grätzel, M. Cleavage of Water by Visible-Light Irradiation of Colloidal CdS Solutions; Inhibition of Photocorrosion by RuO2. *Angew. Chemie Int. Ed. English* **20**, 987–988 (1981).
7. Murray, C. B., Norris, D. J. & Bawendi, M. G. Synthesis and Characterization of Nearly Monodisperse CdE (E = S, Se, Te) Semiconductor Nanocrystallites. *J. Am. Chem. Soc.* **115**, 8706–8715 (1993).
8. Hines, M. A. & Guyot-Sionnest, P. Synthesis and characterization of strongly luminescing ZnS-capped CdSe nanocrystals. *J. Phys. Chem.* **100**, 468–471 (1996).

9. Reiss, P., Protière, M. & Li, L. Core/Shell Semiconductor Nanocrystals. *Small* **5**, 154–168 (2009).
10. Medintz, I. L., Uyeda, H. T., Goldman, E. R. & Mattoussi, H. Quantum dot bioconjugates for imaging, labelling and sensing. *Nature Materials* **4**, 435–446 (2005).
11. Chan, W. C. W. & Nie, S. Quantum Dot Bioconjugates for Ultrasensitive Nonisotopic Detection. *Science (80-.).* **281**, 2016–2018 (1998).
12. Bruchez, M., Moronne, M., Gin, P., Weiss, S. & Alivisatos, A. P. Semiconductor nanocrystals as fluorescent biological labels. *Science (80-.).* **281**, 2013–2016 (1998).
13. Banerjee, A., Pons, T., Lequeux, N. & Dubertret, B. Quantum dots-DNA bioconjugates: Synthesis to applications. *Interface Focus* **6**, (2016).
14. Hedi Mattoussi, *,† *et al.* Self-Assembly of CdSe−ZnS Quantum Dot Bioconjugates Using an Engineered Recombinant Protein. (2000). doi:10.1021/JA002535Y
15. Hermanson, G. T. *Bioconjugate Techniques: Third Edition*. *Bioconjugate Techniques: Third Edition* (Elsevier Inc., 2013). doi:10.1016/C2009-0-64240-9
16. Waalkes, M. P. Cadmium carcinogenesis. *Mutation Research - Fundamental and Molecular Mechanisms of Mutagenesis* **533**, 107–120 (2003).

Chapter 2. Toxicity Assessment of Micelle encapsulated Mn-doped ZnSe Quantum dots

This chapter describes the preparation of nontoxic aqueous quantum dots and analysis of their toxicity using a human liver cancer cell line. This study was funded by NSF DBI-1555470. The Mn-doped-ZnSe synthesis and surface modifications were done by Dr. Qirui Fan, Dr. Abhilasha Dehankar, and Thomas Porter. The toxicity studies on CdSe/ZnS-MPA, CdSe/ZnS micelles and Mn-doped-ZnSe-MPA were conducted by Dr. Qirui Fan. The toxicity studies on Mn-doped-ZnSe micelles and TUNEL assay on Mn-doped-ZnSe-MPA were conducted by Dr. Abhilasha Dehankar and Thomas Porter. TEM imaging of the particles was conducted by Dr. Abhilasha Dehankar. The statistical analysis of the toxicity results was conducted by Dr. Abhilasha Dehankar and Thomas Porter. The first draft of this chapter was authored by Dr. Qirui Fan. The materials and method section and images for the paper were prepared by Thomas Porter and Dr. Abhilasha Dehankar. The final draft for this chapter was edited by Dr. Abhilasha Dehankar.

Introduction

Semiconductor nanocrystals, or quantum dots (QDs), have attracted growing interest over the past two decades. QDs have been used in solar cells, LEDs, lasers, bioimaging, biosensors, and therapeutics.[17–20] Further, QDs are known to possess exceptional brightness, sharp emission peaks, large stokes shifts, and extraordinary photostability in contrast to their traditional fluorescent counterparts – molecular dyes.[21] As a result, QDs present themselves as ideal replacements for low-performing molecular dyes. However,

conventional QDs are synthesized from heavy metal elements such as cadmium, raising concerns about their toxicity both in biological systems and in the environment.[22,23]

As early as 2004, Derfus et al. correlated QDs toxicity with the release of Cd^{2+} *in vitro*[24], and Hoshino et al. first discovered the critical role of QDs surface coating in cytotoxicity[25]. Since then, numerous investigations have been conducted to elucidate the toxicity mechanisms of QDs and to develop strategies toward reducing their toxicity.[22,26–28] Although some of these studies report different or contradicting results, likely because of the varying QDs preparation processes and the complexity of the biological systems (i.e., various cell types[29], cell culture vs. animals[27]), most of them attribute QDs toxicity to the constituent elements and physicochemical properties, such as surface charge, ligand length, and size of the nanoparticles[30]. Therefore, for a comprehensive understanding of QDs toxicity, studying the effects of both NP constituents and physicochemical properties is necessary.

Primarily, the constituent elements (e.g., cadmium) can be extremely toxic and detrimental to various organs. On a cellular level, cadmium causes DNA damage, induces an elevated level of reactive oxygen species (ROS) that leads to apoptosis, and affects other biological activities.[31] Although a layer of ZnS shell can reduce the toxicity of the CdSe QDs[23,24], QDs toxicity is more complex than the mere presence of the cadmium element[32]. Cadmium-free QDs are preferred both for reduced cytotoxicity and for the environment in the long run.[33,34] For example, indium phosphide provides an alternative elemental composition for QDs covering the visible wavelength range, and the InP/ZnS core/shell

QDs have shown reduced toxicity.[35,36] Further, QDs of ZnSe or ZnS nanocrystals doped with manganese (Mn) have also demonstrated decreased toxic effects.[37–43]

The physicochemical properties of QDs synthesized in the organic phase are primarily determined by their phase transfer method (e.g., ligand exchange, micelle encapsulation, or silica coating) and materials (e.g., ligands, coating). Mainly, different coating strategies produce QDs of different sizes and surface chemistries that not only have a direct impact on toxicity but also affect the cellular uptake of nanoparticles and their subsequent subcellular distribution.[30,44–47] Generally, charge produces more dominant effects as compared to ligand length and particle size[30], but in animal studies, size may become a critical factor because of the renal clearance threshold[48].

Recently, we reported the synthesis of Mn-doped ZnSe QDs that are believed to possess more promising super-resolution imaging and magnetic resonance imaging (MRI) features than conventional QDs.[49] These doped QDs displayed a novel tetrapod shape, unlike most spherical shaped Mn-doped QDs that have demonstrated lower toxicity.[38,39,43] To our knowledge, none of the toxicity studies on Mn-doped QDs in the literature were conducted on tetrapod shaped nanocrystals.[38–43] Thus, the interaction and toxicity effects of irregularly shaped cadmium-free nanocrystals on cells were unclear before this study. Also, in the same study, we showed enhanced brightness and photostability of individual assemblies of micelle templated CdSe/ZnS QDs and Mn-doped ZnSe QDs against high-intensity laser radiation desirable for super-resolution imaging.[49] The observed results were attributed to the thicker layer of micellar protection that limited the diffusion of any oxidative species. Thus, micelles prove to be a better barrier compared to conventional ligands. Therefore,

current work presents the first in-depth toxicity analysis of the tetrapod-shaped Mn-doped ZnSe QDs phase-transferred to aqueous phase by micelle encapsulation.

Here, we compared the toxicity effects of our cadmium-free Mn-doped ZnSe QDs on HepG2 human liver carcinoma cell lines with that of commercial CdSe/ZnS core/shell QDs. Additionally, we evaluated these QDs at different physicochemical property conditions, size, and material by studying their toxicity response after aqueous transfer by ligand exchange versus micelle encapsulation. Assays elucidating cell viability and proliferation, ROS generation, and DNA fragmentation were performed considering the commonly observed toxicity pathway for cadmium-based QDs at different concentrations of QDs. Our results show that Mn-doped ZnSe QDs display negligible toxicity and micelle-encapsulation eliminates the toxicity of CdSe/ZnS QDs in the studied concentration range.

Material and Methods

Materials

Zinc stearate (12.5-14%, ZnO), selenium powder (99.999%, ~200 mesh), tetramethylammonium hydroxide pentahydrate (TMAH, 25% w/w in methanol), manganese chloride ($MnCl_2$, 97%), and octadecylamine (ODA, 98%) were purchased from Alfa Aesar. Stearic acid (SA, ≥98.5%), 1-octadecene (ODE, ≥95.0%), 3-mercaptopropionic acid (MPA, ≥99%), and tributyl phosphine (TBP, 97%), acetone (≥99.9%), and poly(vinyl alcohol) (PVA , 13-23 kDa, 87-89% hydrolyzed) were purchased from Sigma-Aldrich. Chloroform was purchased from Fisher Scientific. Poly(styrene-b-ethylene glycol) (PS-PEG-COOH) with a carboxylic acid termination (molecular weight of 18-b-9.5 kDa) was purchased from Polymer Source. Organic

CdSe/ZnS QDs (λ_{em} = 605 nm) dispersed in decane and CdSe/ZnS QDs with carboxylic acid termination (λ_{em} = 605 nm) dispersed in pH 9 borate buffer were purchased from Invitrogen.

Preparation of Mn-ZnSe QDs

Mn-doped ZnSe QDs were synthesized using the following protocol described by Pradhan, N., et al.[50,51]

Synthesis of $MnSt_2$ precursor

Briefly, SA (1.42 g) was dissolved in methanol (10 mL) in a three-neck flask (100 mL) by heating (~50-60 °C) until the solution became transparent. Then, the solution was cooled to room temperature, resulting in the formation of white SA precipitates. Next, 2.3 mL of TMAH diluted with 1.5 mL of methanol was added dropwise to the SA precipitates until their complete dissolution. Then, $MnCl_2$ (0.315 g) dissolved in methanol (3.15 mL) was added dropwise to the transparent solution above under vigorous stirring, producing white precipitates of $MnSt_2$. The $MnSt_2$ precipitate was washed six times with methanol to remove unreacted precursors and dried under vacuum before the synthesis of Mn-doped ZnSe QDs.

Synthesis of Mn-doped ZnSe QDs

In a typical experiment, a Se-TBP stock solution was prepared inside a glove box by dissolving Se (0.63 g) in TBP (2.7 mL). Then, the Se-TBP stock solution (1.5 mL) was injected in a 25 mL three-neck flask containing ODA (1.3 g) inside the glove box and immediately connected to an inert argon (Ar) manifold after removal from the glovebox. The mixture was then heated to ~70˚C under Ar to dissolve the ODA. Next, $MnSt_2$ (0.1g)

and ODE (25 mL) was loaded into a 100 mL three-neck reaction flask. The reaction solution was then heated to 110°C until the solution turned transparent, followed by Ar bubbling at 110°C for 20 minutes. Later, the reaction solution was gradually heated to 290°C under Ar. At 280°C, the entire Se-TBP stock solution was swiftly injected into the reaction solution. After the injection, the reaction temperature was reduced to 260°C for 60 minutes.

Meanwhile, $ZnSt_2$ stock solution was prepared by mixing $ZnSt_2$ (2.5 g), SA (0.5 g), and ODE (12 mL) in a 50 mL flask, followed by heating to ~150°C and degassing under argon. Additionally, ODA-ODE solution was prepared by mixing 2.5g of ODA and 2.5 mL of ODE in a 15 mL flask. After 60 minutes, the reaction temperature was set to 300°C, and the heated $ZnSt_2$ stock solution (4 mL) was swiftly injected into the reaction solution at 290°C. The reaction temperature was then reduced to 260°C, followed by addition of melted ODA-ODE (1 mL) solution. Next, the $ZnSt_2$ stock solution (3 mL per injection) was injected in 15 minute intervals for three injections. Additionally, melted ODA-ODE solution (1 mL) was injected 5 minutes after each $ZnSt_2$ injection. The reaction solution was cooled to room temperature 15 minutes after the final $ZnSt_2$ injection. The unpurified Mn-ZnSe nanocrystals were stored at 4°C.

Purification of Mn-ZnSe QDs

Mn-doped-ZnSe QDs were purified immediately before ligand exchange or micelle encapsulation by employing anti-solvent precipitation. During purification, 100 µL chloroform was added to unpurified QDs heated to 37°C (100 µL) and the mixture was heated to 70°C. Following this, acetone (200 µL) was added to the transparent solution and

the mixture was re-heated to 70°C. The QDs were then centrifuged (20817 rcf, 20 seconds) out of the solution. After removal of the supernatant, the same procedure was repeated two more times, and the final QD pellet was dissolved in chloroform.

Preparation of water-soluble QDs

Synthesis of QD-MPA by ligand exchange

Both water-soluble CdSe/ZnS and Mn-ZnSe QDs were produced from their organic precursors in chloroform via ligand exchange with 3-mercaptopropionic acid (MPA). Organic CdSe/ZnS QDs in decane were first transferred to chloroform using a methanol/isopropanol mixture (2/1 v/v) to precipitate the QDs. For ligand exchange, QDs dissolved in chloroform (300 µL) were mixed with MPA (30 µL) and sonicated for 1 hour. After 1 hour, the solution was centrifuged, and the pellet was washed once in chloroform. Next, the pellet was dissolved in 10 mM NaOH, followed by purification of excess MPA by centrifugal filtration (100 kDa, three times) and recovery. Both the QDs-MPA were sterilized by passing them through a 0.22 µm syringe filter before resuspension in cell medium at the desired concentration.

Synthesis of micelle encapsulated QDs

Micelles encapsulating QD nanoparticles were created using the interfacial instability process. For micelle encapsulation of CdSe/ZnS QDs, QDs (0.35 mg/mL, 100 µL) and PS-PEG-COOH (20 mg/mL, 10 µL) in chloroform were mixed together in a 15 mL centrifuge tube, followed by addition of PVA (5 mg/mL, 3 mL) dissolved in water to form an emulsion. The emulsion was then bath sonicated for an hour to achieve uniform emulsion droplets. The chloroform in the emulsion was subsequently evaporated over time in an

aluminum dish on a rocker, forming micelle-encapsulated QDs in the aqueous solution. Empty micelles were prepared by the same procedure using chloroform (100 µL) devoid of QDs. For Mn-doped-ZnSe QDs, first, the native ligand was exchanged with octanethiol by employing the procedure used for MPA ligand exchange. The QDs were subsequently washed twice with an acetone/methanol mixture (60/40 v/v 1st wash, 50/50 v/v 2nd wash) to remove excess octanethiol. For micelle encapsulation of Mn-ZnSe QDs, QDs (1.3 mg/mL, 50 µL) and PS-PEG-COOH (20 mg/mL, 10 µL) in chloroform were mixed in a 10 mL glass vial, followed by addition of PVA (5 mg/mL, 3 mL) dissolved in water. The mixture was then probe sonicated for 2 mins, and the chloroform in the resulting emulsion was evaporated over time in an aluminum dish on a rocker to form a clear solution of micelle encapsulated QDs. Both the micelles encapsulated QDs were sterilized by passing them through a 0.22 µm syringe filter. The sterilized micelles encapsulated QDs were then washed five times using a 100 kDa centrifugal filter to remove excess PVA before resuspension in cell medium at the desired concentrations.

Toxicity assays

HepG2 cells were used to evaluate QD toxicity *in vitro*. Cells were cultivated in improved minimum essential medium (MEM) with 10% FBS, 1% penicillin/streptomycin (10k U/mL), and 0.2% mycozap at 37°C, 5% CO2. Cells were fed every other day and passaged at ~ 80% confluency.

MTT assay

MTT tests were performed with the Vybrant® MTT Cell Proliferation Assay Kit (V-13154, Life Technology). Briefly, cells were seeded in 96 well plates at 5,000 cells per well with

five replicas at each concentration level. As prepared nanoparticle samples were diluted to experimental concentration with concentrated cell medium. After 24 h incubation, cell medium was removed, and 50 µL of nanoparticle solution was added to the plate and incubated with the cells for 24 h. Then, the nanoparticles were removed, and 100 µL of phenol red-free cell medium and 10 µL of 12 mM MTT solution was added to each sample and control well in the plate and incubated for four hours. Finally, 10% SDS solution was added to the plate to dissolve the formazan (converted from MTT by viable cells), and the product was evaluated at 570 nm using a microplate reader.

ROS assay

The ROS assay was performed with CellROX® Green Reagent (C10444, Life Technologies). Cell culture and nanoparticle incubation were identical to the MTT assay, except the cell seeding density of 20,000 cells/well. The stock ROS reactive dye solution was added to the cell medium at a final concentration of 12.5 µM. The dye was incubated for 30 min before washing with PBS twice. Then, the plate was measured using a fluorescent microplate reader under the FITC filter setting.

TUNEL assay

The apoptosis study was performed using the Click-iT® Plus TUNEL kit, employing Alexa Fluor® 488 (C10617, Life Technologies) kit. Cell culture and nanoparticle incubation were as described in the ROS assay (3 replicas at each QD concentration), and stock solutions were prepared according to the manufacturer's instructions. After treating cells with nanoparticles for 24 h, the cells were washed with PBS, fixed with paraformaldehyde, permeabilized with Triton X-100. Treatment for one hour with 10 unit/mL of DNase (Life

Technologies, 18068-015) was used as a positive control. Cells were then treated with EdUTP nucleotide mixture and TdT (terminal deoxynucleotidyl transferase), labeled with Alexa 488 through copper (I) catalyzed click chemistry, and measured using a fluorescent microplate reader under the FITC filter setting.

Statistical Analysis

One-way ANOVA was used to determine statistically different assay readouts among different concentrations of the same type of QDs, with $p<0.05$. If the mean readouts were found to be statistically different, a Dunnett's test was conducted to compare each sample to its control, with $p<0.05$. For MTT and ROS assays, three replicate plates with five repeats of each concentration and controls were measured per plate. ROS consisted of two controls – a positive and negative control, whereas MTT consisted of only one negative control. Within each plate, the five repeat measurements per concentration or control were averaged. The average readouts of blank wells were then subtracted from the average of sample and control wells to determine the absolute measurement of each concentration and control, respectively. Next, within each plate, the calculated absolute readouts were normalized against the absolute control value. Statistical tests were conducted on these normalized values from each plate. Standard deviations were calculated and normalized within each plate from the five replicate measurements, and then a pooled standard variance was determined from the three plates for concentration/control. For the TUNEL assay, only one plate with three replicate measurements of each concentration, a positive control, and a negative control was measured. Readouts from blank wells were subtracted

from the sample measurements, and statistical tests were conducted on the three replicate values of each sample. The final values were then normalized to the averaged control value.

Results and Discussion

Selection of commercial QDs for toxicity analysis

One of the primary goals of this investigation was to evaluate the effectiveness of micelle templates compared to conventional surface ligands on CdSe/ZnS QDs. However, it is evident from the literature that different CdSe/ZnS QDs may possess different toxicity depending on their size and surface ligands.[30] Thus, it was essential to choose the CdSe/ZnS QDs that are capable of producing a significant difference in toxicity signal in a limited amount of time for the study. Therefore, we first performed a primary response screening of diverse sizes of commercial CdSe/ZnS QDs from different vendors at different concentrations to identify the most toxic QDs. For this study, we performed an MTT assay to measure the viabilities of cells treated with different sized aqueous QDs from two different vendors (QD560, QD580, QD600 from vendor 1 and QD605 from vendor 2) at two different concentrations. Results showed lower cell viability in vendor 2 QDs as compared to vendor 1 QDs even at higher concentrations (Figure 2). Assessing the origin of these differences was beyond the scope of this investigation. Regardless, vendor 2 QD605 displayed the highest potential to serve as the control CdSe/ZnS QDs for observing coating-based toxicity differences and were selected for detailed toxicity analysis.

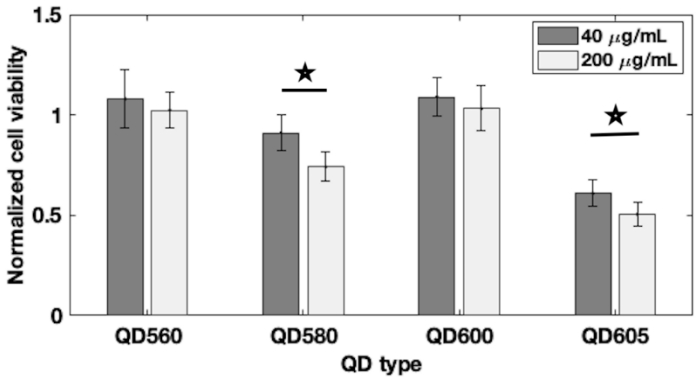

Figure 2 MTT test of different types of CdSe/ZnS QDs (QD560, QD580, QD600 are from Vendor 1, at 40 μg/ml and 200 μg/ml, respectively; and QD605 is from Vendor 2, at 20 μg/ml and 100 μg/ml, respectively). QDs with an asterisk show statistically significant differences in cell viabilities at different concentrations

Characterization of phase-transferred Mn-doped ZnSe QDs

Mn-doped ZnSe QDs were synthesized in-house by a nucleation-doping strategy introduced by Pradhan. et. al. in the organic phase.[50] The resulting Mn-doped ZnSe QDs displayed an absorption shoulder at ~440 nm and an emission peak at 575 nm.[49] Notably, the Mn-doped QDs produced are tetrapod-shaped, in contrast to spheres or elongated rods. Despite their poor performance evident from the decreased colloidal stability, fluorescence preservation, and high non-specific binding observed in MPA-coated QDs, MPA ligands have been the most commonly used ligands in the toxicity study literature.[23–25,32,47] Additionally, PEO (or PEG) in PS-PEG-COOH is known for reducing non-specific interaction with proteins, and negative surface charges such as carboxylic acid (-COOH) have demonstrated lower toxicity than positively charged NPs.[30] Therefore, Mn-doped

ZnSe (Figure 3) and CdSe/ZnS QDs were transferred to the aqueous phase either by ligand exchange with MPA for comparison with existing literature or via micelle encapsulation with amphiphilic polymer, PS-PEG-COOH.

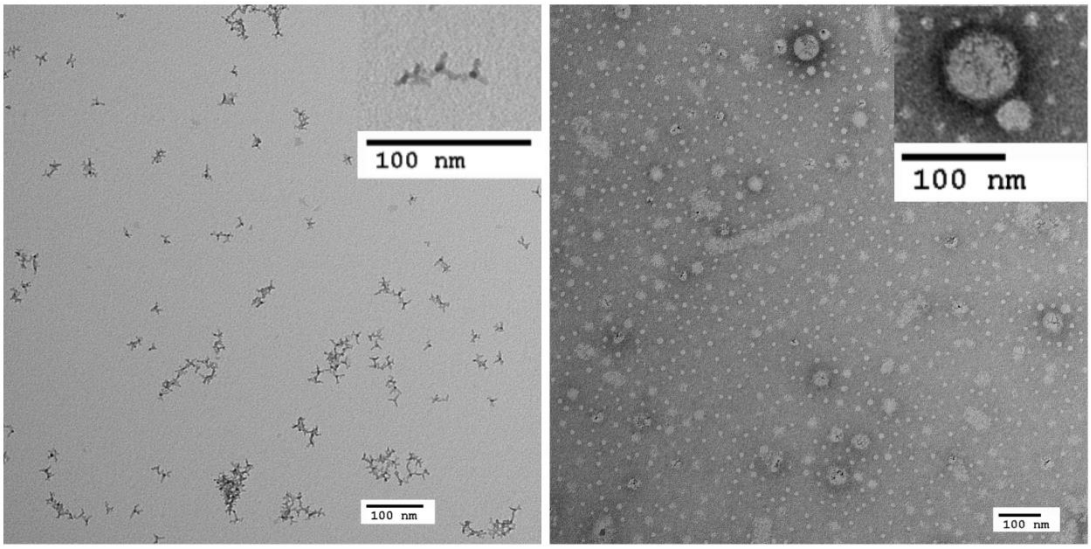

Figure 3 MPA coated Mn-ZnSe QDs (Mn-ZnSe-MPA, left), Micelle encapsulated Mn-ZnSe QDs (Mn-ZnSe-Micelle, right)

Before advancing toward in-depth toxicity analysis, preliminary studies described below were conducted to account for the toxicity effects from the constituent materials involved in micelle encapsulation. Micelle formation via interfacial instability employed in the current study involves the dissolution of QDs and polymers in chloroform during the encapsulation process. However, Chloroform is highly toxic. As a result, it is necessary to confirm that chloroform in the final composite is below the acceptable limit for biological

application despite its volatility and low miscibility (8.09 g/L at 20°C) in water. A quantitative colorimetric assay (data not shown) was applied to determine the final chloroform concentration in the solution used for treating the cells.[52] Results indicate the presence of < 5.7 ppm chloroform, which is considerably below the permissible occupational exposure limit of 50 ppm according to the Occupational Safety and Health Administration.

Additionally, PVA was used during micelle preparation as an emulsifier. MTT assay was conducted on cells exposed to varying concentrations of PVA to account for toxicity effects of PVA present in the micelle dispersions after purification. No significant changes were observed in cell viabilities after PVA treatment, indicating negligible cytotoxicity (Figure 22). Similarly, the toxicity effects of empty micelles were investigated by treating the cells at varying concentrations of micelles prepared in the absence of QDs. MTT assay showed no reduction in cell viabilities after treatment with empty micelles, suggesting insignificant toxicity effects (Figure 23).

As mentioned in our previous work, the micelle templated QDs have sizes ranging from 30-50 nm.[49] However, larger nanoparticles possess a high tendency toward aggregation. Although our QD micelles displayed good stability in normal conditions, signs of aggregation appeared after concentrating them by high-speed centrifugation (e.g., 20k rcf) or centrifugal filtration (using 100kDa filters). Concentrations of QD-micelles are frequently increased during toxicity studies to achieve desired concentrations for treating cells. For example, CdSe/ZnS micelles were first concentrated to 250 µg/mL by centrifugal filtration and then diluted into the cell medium at the desired concentration for toxicity

studies. MTT assay was performed on cells treated by different concentrations of CdSe/ZnS micelles by dilution from 250 µg/mL versus 35.0 µg/ml. To account for the effect of toxicity because of over-concentration. MTT results for dilution from 250 µg/mL showed a cell viability of 90% at 12.5 µg/mL, and 53% at 25.0 µg/mL (Figure 24) whereas negligible toxicity was observed in QD-micelles diluted from 35.0 µg/ml (Figure 4). Observed toxicity for treatment by diluting highly concentrated micelles may be attributed to deformations in the QD or micelle structures during the aggregation promoting the leakage of the toxic elements of CdSe/ZnS QDs into the cellular solution. Therefore, all micelle solutions were prepared at 35.0 µg/mL solution for the remainder of this study.

Effect on cell viability and proliferation

All toxicity studies were conducted on the human hepatic cell line HepG2 cells after treating them with MPA or micelle templated QDs for 24 hours. Initially, MTT assays were performed on the cells treated with QDs at concentrations ranging from 1.56 - 25.0 µg/mL. The effect on cell viability was determined by comparison with the viabilities of untreated cells (Figure 4). Results for CdSe/ZnS-MPA QDs displayed a statistically significant decrease in the MTT signal at a concentration as low as 3.13 µg/mL. The cell viability decreased further with increasing concentration. Additionally, although the average viability of the 1.56 µg/mL wells did not show a statistically significant difference as compared to untreated cells, the possibility of a negative impact on cells below the detection limit of this assay cannot be eliminated. The observed effects on cell viability can be correlated to the toxic nature of cadmium ions as evident from previous studies.

Although ZnS shell coating can alleviate the release of the cadmium ions, the thickness and the quality of the coating may offer varying degrees of protection.[23,24]

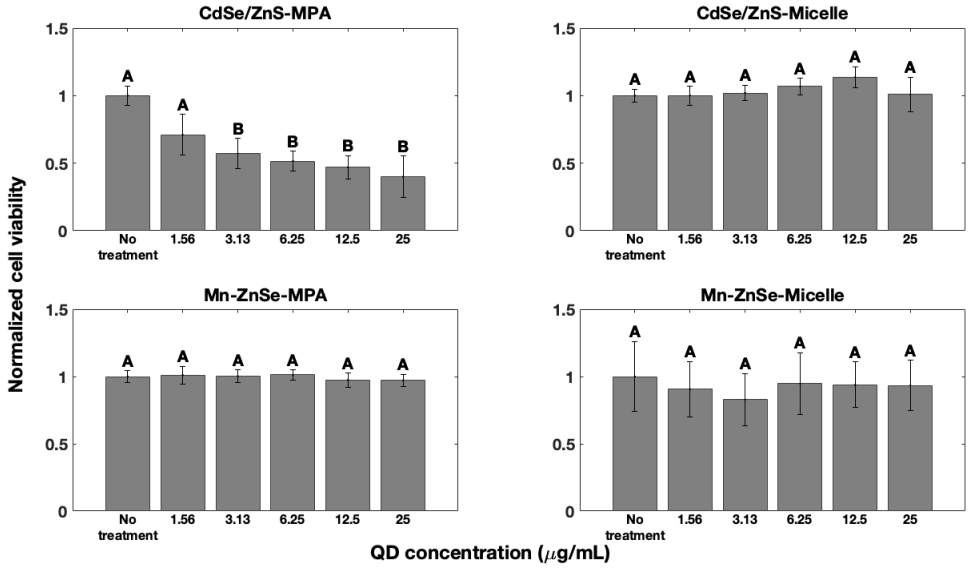

Figure 4 MTT assay on 4 types of QDs: CdSe/ZnS-MPA: MPA coated CdSe/ZnS QDs; CdSe/ZnS-Micelle: Micelle encapsulated CdSe/ZnS QDs; Mn-ZnSe-MPA: MPA coated Mn-doped ZnSe QDs; Mn-ZnSe-Micelle: Micelle encapsulated Mn-doped ZnSe QDs. Cell viabilities of QD concentration with different letter show statistically significant difference from control.

In contrast, the tetrapod-shaped Mn-doped ZnSe QDs with MPA ligands did not show significant cell viability reduction at any of the tested concentrations. The observed results were analogous to other investigations that demonstrated minimal toxicity of Mn-doped QDs. For example, Drobintseva et al. observed that exposing the human mononuclear

lymphocytes to Mn-doped ZnSe QDs did not cause cell morphology change.[40] Zhou et al. conjugated Mn-doped ZnSe/ZnS QDs with nano-hydroxyapatite (80-120 nm nanorods) and did not observe significant toxicity at 200 μg/ml for HepG2 cells (Note: The molar QD concentration in this study is probably much lower than our QDs because of the large size of the tested nanorods).[38] Mohammad et al. synthesized Mn-doped ZnS QDs, and showed close to 100% cell viability at a 25 μg/mL particle concentration over a 24 hour incubation period, but showed decreased viability for higher concentrations.[43] Despite the differences in the doped QD compositions and the synthesis routes, these studies suggest lower toxicity of Mn-doped QDs over conventional CdSe/ZnSe QDs, complementary to our observations.

Further, the micelle templated CdSe/ZnS, as well as Mn-doped ZnSe QDs, also showed no reduction in cell viability for 24-hour incubation. Micelle encapsulation for aqueous transfer of QDs retaining the native surface ligands of QDs offers an additional layer of protection. Thus, unlike the ligand exchange process that displaces the native ligands (e.g., octadecylamine and trioctylphosphine oxide in our QDs) and promotes the introduction of surface defects by stripping of surface cations[53,54], micelle encapsulation preserves the integrity of the nanocrystals. Also, the thick polymer layer may decrease the rate of constituent ions being released out of the micelles over time. Our previous study has shown that micelle-templating offers protection against high intensity induced photobleaching of QDs.[49] Here, the MTT result suggests that micelle protection could also be applied to cell

toxicity reduction. These findings are in agreement with Yong et al. that reported phospholipid-PEG micelle coated QDs as safe at a dosage as high as 150~200 μg/mL.[28]

Lastly, the observed effect on cell viability is cumulative of cellular uptake efficiency and particle toxicity. Cellular uptake is dependent on particle size and surface charge.[46] Thus, the size difference between the micelles (~30-40 nm) and the MPA QDs (<10 nm) may affect the efficiency of the endocytosis and exocytosis processes.[55] However, cellular uptake exhibits a stronger dependence on the surface charge compared to size.[46] Since both MPA and PS-PEG-COOH display carboxylic acid groups on their surfaces, their cellular uptake may be considered to be at comparable levels. Additional analysis of cellular uptake is beyond the scope of this investigation.

Reactive oxygen species formation

Changes in cell viability is a cumulative effect of changes in the amount and the metabolic rates of cells. Thus, negligible changes in cell viability may occasionally be observed despite significant changes in the cellular metabolic rates. Changes in metabolic rates have often been correlated to the presence of oxidative stress by the generation of ROS.[56] Further, cadmium-based cytotoxicity has also been associated with the generation of reactive oxygen species (ROS).[31] Therefore, ROS assay was performed on cells treated with QDs to further investigate the toxicity of Mn-doped QDs and the mechanism of CdSe/ZnS-MPA toxicity. The differences in the generation of ROS after NP treatment were determined by comparison with untreated cells (Figure 5). Menadione stimulates the production of ROS in cells and was employed as a positive response control. The micelle

templated CdSe/ZnS QDs and MPA coated and micelle encapsulated Mn-doped QDs did not produce significantly different ROS signal as compared to the untreated cells (alpha = 0.05, $p < 0.05$) whereas significantly higher ROS signal was produced in menadione treated cells. Thus, results indicate that MPA coated Mn-doped ZnSe and micelle encapsulated QDs do not increase the ROS in HepG2 cells.

Interestingly, ROS signal for the CdSe/ZnS-MPA QDs was also not significantly different from menadione treated cells, unlike many different studies that have observed enhanced production of ROS in toxic QDs.[57,58] However, many other studies also report an obscure correlation between ROS generation and QD toxicity. For example, Lovrić et al. observed that NAC (N-acetyl-L-cysteine), a ROS inhibitor, could partially reduce QD toxicity, but another antioxidant Trolox did not prevent cellular damage.[47] In another study, Nagy et al. found that pretreating cells with NAC did not rescue cell viability even after lowering ROS production.[30] Nagy et al. correlated the observed toxicity to up-regulation and down-regulation of certain genes, suggesting the presence of other toxicity pathways independent of ROS production.[30] Thus, observed results in our study suggest that CdSe/ZnS-MPA may be causing cellular toxicity from a different pathway beyond the extent of the current study.

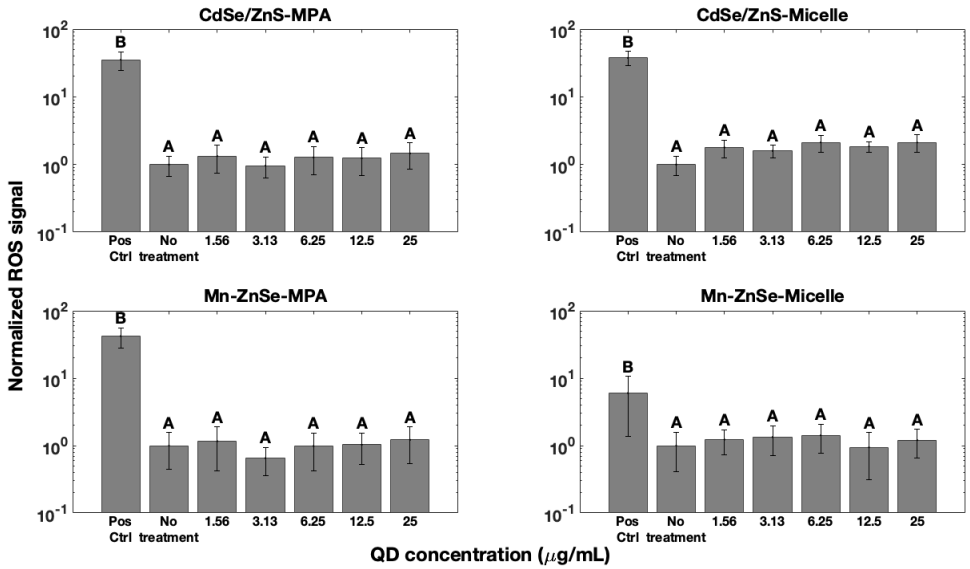

Figure 5 ROS assay on 4 types of QDs: CdSe/ZnS-MPA: MPA coated CdSe/ZnS QDs; CdSe/ZnS-Micelle: Micelle encapsulated CdSe/ZnS QDs; Mn-ZnSe-MPA: MPA coated Mn-doped ZnSe QDs; Mn-ZnSe-Micelle: Micelle encapsulated Mn-doped ZnSe QDs. Normalized ROS signals of QD concentration with different letters show statistically significant differences from the control.

DNA fragmentation

Another factor that indirectly affects cell viability is the number of dead cells. Death of cells by toxicity effects is generally associated with an apoptotic pathway and can be detected by DNA fragmentation. Further, Cadmium can also damage DNA and replace the iron and copper from key cytoplasmic proteins and membrane proteins, in addition to generating ROS and causing apoptosis.[31] Therefore, TUNEL assay was conducted on QD treated cells to detect DNA fragmentation. The differences in DNA breakages was detected

by comparing the TUNEL signal of QD treated cells with untreated cells as the control and DNase treated cells as the positive control (Figure 6). TUNEL signal of QD treated cells was not significantly different from untreated cells, whereas a significant increase was observed for DNase treated cells, indicating negligible changes in DNA fragmentation on the treatment of HepG2 cells with all the tested QDs. For CdSe/ZnS-MPA QDs, it is possible that the release of cadmium ions was enough to impede cell metabolism and proliferation, but not enough to produce a detectable DNA fragmentation signal. A Live/Dead flow-cytometry assay (L34951, Invitrogen) was performed on the CdSe/ZnS-MPA QDs treated cells at concentrations of 6.25 ug/mL and 25.0 µg/mL to test this possibility. Analysis of the assay results displays an effective decrease in the percentage of living cells at 25 µg/mL as compared to 6.25 ug/mL from 82% to 78% with a corresponding increase in the number of injured cells (data not shown). Thus, the results of live/dead assay support that the decrease observed in cell viability in MTT assay is a consequence of an increase in the number of injured cells with lower metabolic activity, which are most likely in the preliminary stages leading up to apoptosis. However, further investigations are necessary to exactly determine the cell signaling mechanism causing damage to the cell membrane after QD treatment.

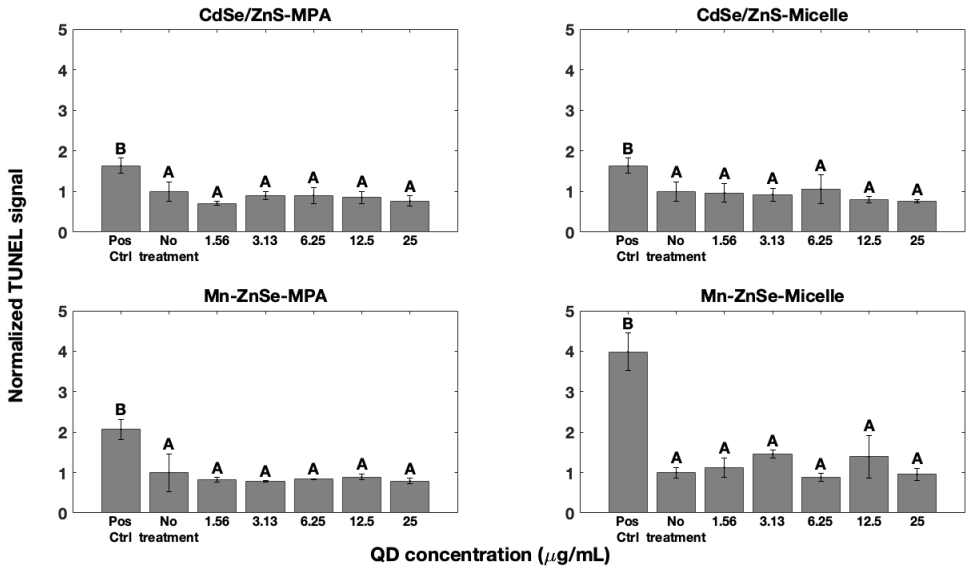

Figure 6 TUNEL assay on 4 types of QDs: CdSe/ZnS-MPA: MPA coated CdSe/ZnS QDs; CdSe/ZnS-Micelle: Micelle encapsulated CdSe/ZnS QDs; Mn-ZnSe-MPA: MPA coated Mn-doped ZnSe QDs; Mn-ZnSe-Micelle: Micelle encapsulated Mn-doped ZnSe QDs. Normalized TUNEL signals of QD concentration with different letter show statistically significant difference from control.

Conclusions

In summary, here we compared the cytotoxicity of the tetrapod-shaped Mn-doped ZnSe QDs and conventional CdSe/ZnS QDs, both prepared either through MPA ligand exchange or PS-PEO-COOH micelle encapsulation. The Mn-doped ZnSe QDs did not show any significant decrease in cell viability or increase in ROS production and DNA fragmentation for both types of coatings at the tested concentrations, in contrast to CdSe/ZnS-MPA QDs,

suggesting that they are inherently less toxic. Further, micelle-templated CdSe/ZnS QDs displayed similar behavior to Mn-doped ZnSe QDs, whereas a concentration-dependent decrease in cell viability was observed in CdSe/ZnS-MPA QDs, indicating that micelles encapsulation is a better aqueous phase-transfer alternative to ligand-exchange for QDs. Therefore, coupled with their excellent optical properties, micelle templated Mn-doped ZnSe QDs serve as promising candidates for biological imaging and diagnostic applications.

References

17. Carey, G. H. *et al.* Colloidal Quantum Dot Solar Cells. *Chemical Reviews* **115**, 12732–12763 (2015).
18. Shirasaki, Y., Supran, G. J., Bawendi, M. G. & Bulović, V. Emergence of colloidal quantum-dot light-emitting technologies. *Nature Photonics* **7**, 13–23 (2013).
19. Biju, V. Chemical modifications and bioconjugate reactions of nanomaterials for sensing, imaging, drug delivery and therapy. *Chemical Society Reviews* **43**, 744–764 (2014).
20. Hildebrandt, N. *et al.* Energy transfer with semiconductor quantum dot bioconjugates: A versatile platform for biosensing, energy harvesting, and other developing applications. *Chemical Reviews* **117**, 536–711 (2017).
21. Resch-Genger, U., Grabolle, M., Cavaliere-Jaricot, S., Nitschke, R. & Nann, T. Quantum dots versus organic dyes as fluorescent labels. *Nature Methods* **5**, 763–775 (2008).
22. Hardman, R. A toxicologic review of quantum dots: Toxicity depends on physicochemical and environmental factors. *Environmental Health Perspectives* **114**, 165–172 (2006).
23. Kirchner, C. *et al.* Cytotoxicity of colloidal CdSe and CdSe/ZnS nanoparticles. *Nano Lett.* **5**, 331–338 (2005).
24. Derfus, A. M., Chan, W. C. W. & Bhatia, S. N. Probing the Cytotoxicity of Semiconductor Quantum Dots. *Nano Lett.* **4**, 11–18 (2004).
25. Hoshino, A. *et al.* Physicochemical properties and cellular toxicity of nanocrystal quantum dots depend on their surface modification. *Nano Lett.* **4**, 2163–2169 (2004).
26. Lewinski, N., Colvin, V. & Drezek, R. Cytotoxicity of nanopartides. *Small* **4**, 26–49 (2008).
27. Tsoi, K. M., Dai, Q., Alman, B. A. & Chan, W. C. W. Are quantum dots toxic? Exploring the discrepancy between cell culture and animal studies. *Acc. Chem.*

Res. **46**, 662–671 (2013).
28. Yong, K. T. *et al.* Nanotoxicity assessment of quantum dots: From cellular to primate studies. *Chemical Society Reviews* **42**, 1236–1250 (2013).
29. Manshian, B. B. *et al.* Cell type-dependent changes in CdSe/ZnS quantum dot uptake and toxic endpoints. *Toxicol. Sci.* **144**, 246–58 (2015).
30. Nagy, A. *et al.* Comprehensive analysis of the effects of CdSe quantum dot size, surface charge, and functionalization on primary human lung cells. *ACS Nano* **6**, 4748–4762 (2012).
31. Rani, A., Kumar, A., Lal, A. & Pant, M. Cellular mechanisms of cadmium-induced toxicity: A review. *International Journal of Environmental Health Research* **24**, 378–399 (2014).
32. Chen, N. *et al.* The cytotoxicity of cadmium-based quantum dots. *Biomaterials* **33**, 1238–1244 (2012).
33. Pelley, J. L., Daar, A. S. & Saner, M. A. State of academic knowledge on toxicity and biological fate of quantum dots. *Toxicol. Sci.* **112**, 276–96 (2009).
34. Rocha, T. L., Mestre, N. C., Sabóia-Morais, S. M. T. & Bebianno, M. J. Environmental behaviour and ecotoxicity of quantum dots at various trophic levels: A review. *Environment International* **98**, 1–17 (2017).
35. Brunetti, V. *et al.* InP/ZnS as a safer alternative to CdSe/ZnS core/shell quantum dots: In vitro and in vivo toxicity assessment. *Nanoscale* **5**, 307–317 (2013).
36. Lin, G. *et al.* In vivo toxicity assessment of non-cadmium quantum dots in BALB/c mice. *Nanomedicine Nanotechnology, Biol. Med.* **11**, 341–350 (2015).
37. Liu, J. *et al.* Aqueous synthesis and bio-imaging application of highly luminescent and low cytotoxicity Mn2+-doped ZnSe nanocrystals. *Mater. Lett.* **65**, 2139–2141 (2011).
38. Zhou, R. *et al.* Low-toxic Mn-doped ZnSe@ZnS quantum dots conjugated with nano-hydroxyapatite for cell imaging. *Nanoscale* **6**, 14319–14325 (2014).
39. Plumley, J. B. *et al.* Noncytotoxic Mn-doped ZnSe/ZnS quantum dots for biomedical applications. in *Colloidal Nanoparticles for Biomedical Applications IX* **8955**, 895513 (SPIE, 2014).
40. Drobintseva, A. O. *et al.* Colloidal CdSe and ZnSe/Mn quantum dots: Their cytotoxicity and effects on cell morphology. *St. Petersbg. Polytech. Univ. J. Phys. Math.* **1**, 272–277 (2015).
41. Swift, B. J. F. & Baneyx, F. Microbial uptake, toxicity, and fate of biofabricated ZnS:Mn nanocrystals. *PLoS One* **10**, e0124916 (2015).
42. Yang, Y. *et al.* Hepatotoxicity assessment of Mn-doped ZnS quantum dots after repeated administration in mice. *Int. J. Nanomedicine* **10**, 5787 (2015).
43. Mohammad, F. & Al-Lohedan, H. A. Toxicity assessment of engineered Mn–ZnS quantum dots in vitro. *J. Mater. Sci.* **51**, 9207–9216 (2016).
44. Chang, E., Thekkek, N., Yu, W. W., Colvin, V. L. & Drezek, R. Evaluation of quantum dot cytotoxicity based on intracellular uptake. *Small* **2**, 1412–1417 (2006).
45. Clift, M. J. D. *et al.* The impact of different nanoparticle surface chemistry and size on uptake and toxicity in a murine macrophage cell line. *Toxicol. Appl.*

Pharmacol. **232**, 418–427 (2008).
46. Peng, L. *et al.* Cellular uptake, elimination and toxicity of CdSe/ZnS quantum dots in HepG2 cells. *Biomaterials* **34**, 9545–9558 (2013).
47. Lovrić, J. *et al.* Differences in subcellular distribution and toxicity of green and red emitting CdTe quantum dots. *J. Mol. Med.* **83**, 377–385 (2005).
48. Soo Choi, H. *et al.* Renal clearance of quantum dots. *Nat. Biotechnol.* **25**, 1165–1170 (2007).
49. Xu, J. *et al.* Micelle-templated composite quantum dots for super-resolution imaging. *Nanotechnology* **25**, 195601 (2014).
50. Pradhan, N. & Peng, X. Efficient and color-tunable Mn-doped ZnSe nanocrystal emitters: Control of optical performance via greener synthetic chemistry. *J. Am. Chem. Soc.* **129**, 3339–3347 (2007).
51. Pradhan, N., Battaglia, D. M., Liu, Y. & Peng, X. Efficient, stable, small, and water-soluble doped ZnSe nanocrystal emitters as non-cadmium biomedical labels. *Nano Lett.* **7**, 312–317 (2007).
52. Ross, J. H. A Color Test for Chloroform and Chloral Hydrate. *J. Biol. Chem.* **58**, 641–642 (1923).
53. Anderson, N. C., Hendricks, M. P., Choi, J. J. & Owen, J. S. Ligand exchange and the stoichiometry of metal chalcogenide nanocrystals: Spectroscopic observation of facile metal-carboxylate displacement and binding. *J. Am. Chem. Soc.* **135**, 18536–18548 (2013).
54. Shen, Y., Tan, R., Gee, M. Y. & Greytak, A. B. Quantum yield regeneration: Influence of neutral ligand binding on photophysical properties in colloidal core/shell quantum dots. *ACS Nano* **9**, 3345–3359 (2015).
55. Oh, N. & Park, J. H. Endocytosis and exocytosis of nanoparticles in mammalian cells. *International Journal of Nanomedicine* **9**, 51–63 (2014).
56. Salin, K. *et al.* Individuals with higher metabolic rates have lower levels of reactive oxygen species in vivo. *Biol. Lett.* **11**, (2015).
57. Lovrić, J., Cho, S. J., Winnik, F. M. & Maysinger, D. Unmodified cadmium telluride quantum dots induce reactive oxygen species formation leading to multiple organelle damage and cell death. *Chem. Biol.* **12**, 1227–1234 (2005).
58. Ipe, B. I., Lehnig, M. & Niemeyer, C. M. On the generation of free radical species from quantum dots. *Small* **1**, 706–709 (2005).

Chapter 3. Fluorescence Loss of Commercial Aqueous Quantum Dots during Preparation for Bioimaging

This chapter describes a systematic evaluation of fluorescence loss of quantum dots from several common vendors during typical procedures employed during their preparation for bioimaging. This study was funded by NSF DBI-1555470. Experimental design and fluorescence and absorbance data collection was done by Dr. Kil Ho Lee and Thomas Porter. Quantum yield calculations and statistical analysis was conducted by Thomas Porter. The introduction was written by Dr. Jessica Winter, the materials and methods was written by Thomas Porter, and the remaining sections were written by Dr. Kil Ho Lee. Dr. Kil Ho Lee produced the figures. This chapter is published in Lee KH*, Porter T*, Winter JO, "Fluorescence Loss of Commercial Aqueous Quantum Dots During Preparation for Bioimaging." MRS Communications, 9(2), 702-709 (2019).[59] *Equally contributing authors.

Introduction

The introduction of quantum dots (QDs) for biological imaging in 1998[12,60] was thought to herald a coming revolution in the field. QDs, crystalline semiconductor nanoparticles, exhibit many properties conducive to imaging because of their small size. Broad excitation spectra enable imaging of multiple colors with a wide variety of excitation sources. High absorption cross sections enable improved photon generation compared to molecular fluorescent dyes.[61] Narrow emission spectra and size-tunable fluorescence are ideal for

multiplexed applications that require several distinct colors to be distinguished in the visible spectrum. Building on these initial reports, QD labels were demonstrated for *in vitro*[62] and *in vivo*[63] labeling applications across many organismal models. However, researchers were poised for a revolution that never came. Although QD products have been introduced by a variety of vendors, there are no clinically approved QDs, and fluorescent dyes remain the mainstay of biological imaging.

One obvious limitation to the clinical adoption of QDs is their toxicity.[64] The most popular QDs for imaging applications are composed of CdSe cores with ZnS passivating shells (CdSe/ZnS). Cadmium is a heavy metal that yields chronic toxicity and carcinogenesis in humans, disrupting DNA repair, hindering mitochondrial respiration, and interfering with systems that employ cations of similar charge (e.g., Zn^{2+}, Mn^{2+}) as co-factors.[16] Despite the fact that studies in primate models yielded no observable effects over 90 days, most of the administered dose remained in the organs of the reticuloendothelial system[65], suggesting the potential for long term effects. Thus, clinicians are reluctant to employ QDs in humans. This problem has been addressed in recent years by the introduction of "green" QDs composed of alternate materials[66], such as Mn-doped ZnSe[50], that eliminate Cd metal from the nanocrystal. Some of these are even commercially available. However, despite these improvements, QDs remain niche products, primarily used for experiments requiring high numbers of multiplexed imaging targets or specific emission wavelengths.

Other possible limitations to QD use in biological imaging are anecdotal reports of poor optical properties. Although QDs have shown increased resistance to photobleaching compared with molecular dyes[60,63], several researchers have observed QD fluorescence

loss throughout the bioconjugation process.[67,68] In particular, losses in fluorescence resulting from dilution, dissolution in biological buffers (particularly containing salts), and following purification procedures, such as centrifugal filtration or dialysis, have been observed. However, a comprehensive analysis has not yet been performed. Further, the mechanisms of QD failure are uncertain. QDs can undergo surface oxidation resulting in the release of free Cd^{2+} and generating fluorescence quenching defects at the nanocrystal surface.[61] However, QDs exposed to high salt concentrations can also undergo aggregation as a result of reduced Debye charge screening of the ionic ligands on their surfaces.[69] Further, recent reports for organic phase QDs[53], suggest that ligand equilibrium dynamics play a strong role in fluorescence loss mechanisms.

Here, we investigated fluorescence loss resulting from QD bioconjugation processes. The most commonly employed QDs for biological applications are composed of CdSe/ZnS coated with organic compounds (e.g., polymers) to promote solubility in aqueous media.[10] Further, these QDs are often modified with antibodies or other biomolecules to permit targeting to specific biomarkers, typically via 1-Ethyl-3-(3-(dimethylamino)propyl)carbodiimide (EDC)-mediated bioconjugation to –COOH groups on their surfaces.[15] Therefore, we examined aqueous, CdSe/ZnS QDs functionalized with carboxylic acid terminal groups (-COOH) from 4 vendors.

In a typical preparation for biological imaging[70], QDs received from the manufacturer are first transferred into a conjugation buffer. Common buffers employed include borate and 2-(N-morpholino)ethanesulfonic acid (MES) buffer. Transfer can be via simple dilution, especially if a small volume of QDs is diluted into a much larger buffer phase, or via

exchange, typically using centrifugal filtration and re-suspension. Then, conjugation chemicals and conjugate are added and incubated for a specified period of time. Following incubation, some preparations require neutralization by addition of an excess of a compound that reacts with the conjugation chemicals. The final product is then purified, usually by centrifugal filtration, dialysis, or gel filtration.

In this work, we evaluated aggregation and fluorescence quantum yield (QY) reduction during the initial steps of the bioconjugation process, specifically, dilution in the original buffer used by the manufacturer, purification via centrifugal filtration, and dissolution in buffers commonly employed for bioconjugation.

Aggregation was evaluated by measuring changes in the fluorescence of the supernatant following centrifugation cycles, whereas QY was evaluated using fluorometry. Thus, for each sample, we evaluated fluorescence loss attributed to reduced concentration, reductions in QY, and material loss to aggregation. The majority of studies employed red QDs (λ_{em} = 600-630 nm) for consistency; however, some green QDs (λ_{em} = 545 nm) were also evaluated to identify differences across emission wavelengths. In some cases, multiple lots were examined to evaluate lot-to-lot variation. These data provide important guidance on optimization strategies for QD bioconjugation and labeling protocols.

Materials and Methods

Materials

To avoid potential conflicts of interest, the vendors used in this study are not disclosed. Red CdSe/ZnS core-shell quantum dots (QDs) (600 nm < λ_{em} < 630 nm) functionalized

with carboxylic acid were purchased from 4 vendors. Green QDs (λ_{em} = 545 nm) were purchased from one of these vendors. All QDs employed were shipped and stored in aqueous media, either pH 9, 50 mM borate buffer or pure water. Amicon ultra 0.5 mL centrifugal filters (cat. No. UFC505024, 100kDa) were purchased from MilliPoreSigma. MES Buffered Saline Packs (cat. No. 28390) and BupH™ Borate Buffer Packs (cat No. 28384) were purchased from ThermoFisher Scientific. Rhodamine 6G (cat. No. 252433) was purchased from Sigma-Aldrich.

UV-Visible Absorbance Spectroscopy

UV-visible absorbance spectroscopy was used to estimate concentrations (against standard curves) of reference dye and QD solutions for quantum yield calculations. Absorbance spectra were obtained using a Genesys 6 UV-Vis spectrophotometer. Background subtraction was performed by scanning an equal volume (400 µL) of fresh solvent inside a Hellma absorption cuvette (path length 10 mm).

Fluorescence Excitation and Emission Spectroscopy

Fluorescence spectroscopy was performed to obtain the fluorescence emission and excitation spectra of reference dye and QD solutions. For both excitation and emission measurements, 80 µL of sample solution was analyzed using a sub-micro quartz cuvette. Fluorescence spectra were obtained with a PTI QuantaMaster™ 40 steady state spectrofluorometer (lamp power: 75W, detector voltage: 1100V). Emission spectra were collected using an excitation wavelength of 488 nm, unless otherwise specified.

Quantum Yield (QY) Calculations

To evaluate fluorescence loss resulting from altered QD material properties, QY was calculated via comparison to a rhodamine 6G reference dye, which has an expected QY of 95% in ethanol.[71] Rhodamine 6G in ethanol was chosen because its excitation wavelength (488 nm) does not interfere with the range of emission wavelengths for the QDs tested (500 nm to 700 nm). Fluorescence emission spectra for QDs were obtained by excitation at the first excitonic peak, λ_{ex}, resulting in maximal emission or at 488 nm, as specified below. The latter excitation wavelength was employed to collect a full emission spectrum without bleed through of excitation light. From the collected spectra, QD QY was calculated using Equation 3.1.[72]

$$QY_{QD} = QY_{ref} \frac{I_{QD}}{I_{ref}} \frac{\lambda_{ex\,QD}}{\lambda_{ex\,ref}} \frac{A_{ref}}{A_{QD}} \frac{\eta_{QD}^2}{\eta_{ref}^2} \quad \text{Equation 3.1}$$

where QY_{QD} is the measured quantum yield of the QDs, QY_{ref} is the quantum yield of the reference dye (i.e. 0.95 for Rhodamine 6G), I_{QD} and I_{ref} are the integrated fluorescence intensities (for QDs and a reference, respectively) calculated by the area under the curve obtained using the spectrofluorometer, $\lambda_{ex\,QD}$ and $\lambda_{ex\,ref}$ (for QDs and a reference, respectively) are the excitation wavelengths used to obtain the emission spectra, A_{QD} and A_{ref} (for QDs and a reference, respectively) are the absorbances obtained using UV-Vis spectrophotometry at the excitation wavelengths, and η_{QD} and η_{ref} are the refractive indices for the solvent containing QDs and the reference, respectively. For excitation at the first peak of the excitation spectra, where bleed through into the emission spectra occurs, I_{QD} was obtained by measuring half of the emission curve from the maximum peak and

multiplying the measured area under the curve by 2. For QDs excited at 488 nm, I_{QD} was obtained by calculating the area under the full emission curve.

Aggregation

Fluorescence losses resulting from particle aggregation in solution were identified by centrifugation. When QDs aggregate, they form large clusters that precipitate easily. Thus, QDs in a 1.5 mL test tube were subjected to centrifugation at low speed (4000 rpm) for 1 min. The fluorescence of the supernatant was measured to determine the amount of fluorescence lost to pellet formation, indicating the extent of aggregation.

Evaluating the Effect of Dilution in Original Solvent

QDs from 4 vendors were shipped at different concentrations in different solvents. Thus, to evaluate the effect of dilution, QDs were diluted across a range of concentrations using the original solvent, either Milli-Q water or pH 9, 50 mM borate buffer. The original concentrations from all vendors were too high to obtain absorbance and/or fluorescence spectra without saturating detectors. Thus, initially, QY was evaluated for QDs diluted in their original solvents to absorbance values between 0.01 and 0.1 at the longest wavelength absorption maxima, which was sufficient to prevent saturation of UV-Vis and fluorescence detectors.[73] Then, further dilution using the original solvents for each sample was performed across a range of concentrations corresponding to an absorbance range of 0.01 to 0.1. QY values were compared to those at the original dilution using the student t-test. All samples were prepared and analyzed at $N \geq 3$.

Evaluating the Effect of Purification via Centrifugal Filtration

To evaluate the effect of purification methods, specifically centrifugal filtration, on QD fluorescence loss, QD fluorescence was evaluated before and after purification via this method. Filtration was conducted by washing 400 µL of QD solution diluted with the original solvent (i.e. water, pH 9, 50 mM borate buffer) to the highest concentration tested in the dilution study using Amicon ultra 0.5 mL centrifugal filter devices at 12,000 rcf for 3 minutes. Then, concentrated QDs were immediately resuspended to the original volume of 400 µL in the original solvent. Filtration was repeated up to 3 times, and QY was measured after each repeat. QY values were then compared to those before filtration using the student t-test. All samples were prepared and analyzed at $N \geq 3$.

Effect of Buffer Exchange

Centrifugal filtration was also used for buffer exchange studies. QDs were processed as above, except, after removing the original solvent, QDs were washed with MilliQ water before dispersion into a new buffer. For QDs shipped in water, QDs were resuspended in new buffer after only one washing cycle. For QDs shipped in other solvents, three washing cycles were performed prior to dispersion into the new buffer. Buffers tested included pH 4.7, 0.1 M MES buffer and pH 9, 50 mM borate buffer because they are commonly used in bioconjugation procedures. In addition, pH 7.3, 50 mM borate buffer was tested to examine the effect of buffer ionic strength on QD stability. QY values were then compared to those before buffer exchange using the Student's t-test. All samples were prepared and analyzed at $N \geq 3$.

Results and Discussion

Initial QY Calculations

QDs received from vendors were highly concentrated. Thus, samples were diluted to avoid saturation of detectors for initial measurements. QY was then determined at this initial concentration using excitation wavelengths corresponding to the first excitation peak and also at 488 nm (to prevent excitation bleed through in the emission spectrum) (Figure 25 (a) summary and (b) full spectra).

Measured QYs ranged from ~ 60% or 40% for green and red QDs, respectively, to as little as ~ 5% (red QDs). All vendors provided expected QY values for their QDs, although the methods of measurement were not indicated. QY values measured by our methods, following dilution and compared to a known reference, were substantially lower than reported values in all but 2 cases (Red, vendors #2 and 3). This may result from the methodology employed (i.e., QY measurement against a reference vs. use of the integrating spheres[74]), which prevented evaluation at the as shipped concentration. QYs of > 50% are generally desired for imaging applications.[75] Nonetheless, QDs with QY < 10% have been successfully employed for cell labeling[76], suggesting that even products with low QY may still result in successful imaging results. We also observed only slight differences in QY values regardless of the excitation energy employed (i.e., first excitation peak vs. 488 nm), with the largest difference observed for Vendor #1 Red. Thus, we do not believe that excitation wavelength contributes to this discrepancy between measured and reported values. In subsequent experiments, an excitation wavelength of 488 nm was employed to permit the full emission spectra to be collected without excitation bleed through.

Effect of Dilution with Original Solvent

Most bioconjugation and labeling protocols require dilution of QD stock solutions before use. QD stability is critically linked to the local environment, and in particular, the ionic strength of the media.[77] The presence of proteins and other additives in cell culture medium and serum can further alter this response.[78] Thus, we evaluated the influence of dilution on QD fluorescence losses resulting from aggregation and reduced QY. To decouple fluorescence QY losses resulting solely from dilution from those resulting from buffer incompatibility, we first evaluated QD fluorescence loss upon dilution with the original aqueous solvent in which QDs were shipped and stored. QDs were diluted across a range of concentrations consistent with absorbance values between 0.01 and 0.1 at the longest wavelength absorption maxima, with maximal concentration values corresponding to those used in Figure 25 (Figure 7**,** Figure 26).

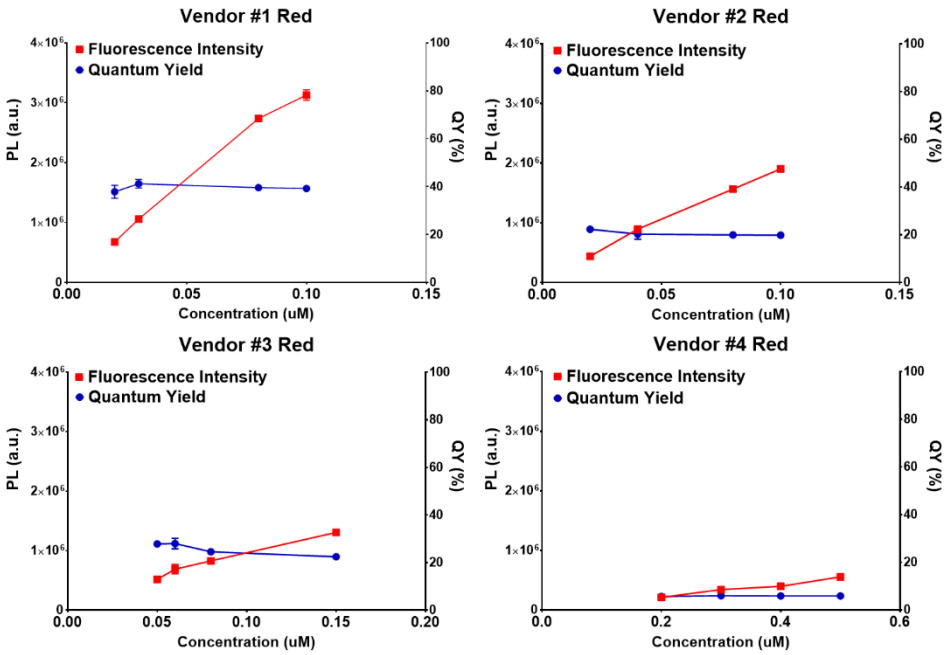

Figure 7 Photoluminescence intensity (PL) and QY of red QDs from four vendors as a function of concentration. Fluorescence intensity is concentration dependent and thus is expected to decline with dilution, whereas QY is not.

Fluorescence intensity, which is correlated to the total number of photons emitted, is concentration dependent, and thus should decline with dilution. However, QY, which reflects the number of photons emitted over those absorbed, is concentration independent, provided that QDs are not affected by the local aqueous environment. As expected, fluorescence intensity for all vendors declined with dilution (Figure 7). Also, for QY, no statistical difference ($\alpha = 0.05$) was observed across the samples and dilutions investigated; suggesting that the borate buffer and water in which products were shipped did not influence QD surfaces and their photoluminescence emission sites. Further, no aggregation was observed, suggesting colloidal stability in these original aqueous solutions.

To enhance rigor of our analysis, we repeated these experiments with a second lot of material. Unfortunately, only one vendor (Vendor #1) had multiple lots available for purchase, thus our analysis was limited to products from Vendor #1 (Figure 26). The expected QY reported by the manufacturer for Lot 2 was higher than that of Lot 1 by 6%. However, the measured QYs for these two lots were not statistically different ($\alpha = 0.05$) across the range of concentrations investigated. Thus, the second lot displayed a slightly greater difference from the manufacturer's reported QY. No aggregation was observed in these studies. Therefore, in this limited evaluation, we did not observe substantial lot-to-lot variability, although further investigation of many lots from each of the vendors would be required to conclusively evaluate this variable.

Next, we evaluated the influence of emission wavelength on fluorescence loss. CdSe/ZnS QD fluorescence derives in part from the nanocrystal surface[3], which is much less stable than the interior of the nanocrystal. Thus, smaller QDs (emitting toward the blue end of the spectrum), which have higher surface to volume ratios, are expected to exhibit a greater propensity for QY loss as a result of surface defects than larger QDs (toward the red end of the spectrum). Therefore, we evaluated fluorescence loss upon dilution for green-emitting carboxylate-functionalized CdSe/ZnS QDs (λ_{em} =545 nm) from Vendor #1. For these materials, the manufacturer's reported QY was lower than that of red QDs (Lot 1) by 25%, but the measured QY was higher than that of red QDs (Figure 26 (B) vs. Figure 25 (a)). Consistent with our previous results, QY measured after dilution was lower than the manufacturer's reported value. Although the difference between the manufacturer's reported QY and the measured QY after dilution was lower than that observed for red QDs,

green QDs showed a larger standard deviation in QY values. This could potentially result from the larger surface to volume ratio of green QDs, reducing stability. However, no aggregation was observed across these experimental conditions, suggesting colloidal stability was maintained.

Effect of Centrifugal Filtration

Most bioconjugation protocols require concentration and purification steps[70], and for QDs, centrifugal filtration devices are often used for these purposes. Purification can result in reduced fluorescence intensity, in part from loss of sample in the filter, but also from increased solution ionic strength, which lowers colloidal stability.[77] Thus, we investigated fluorescence losses resulting from centrifugal filtration and up to 3 washing steps. For these experiments, samples were investigated at the highest concentration tested in the dilution study and were washed with the aqueous media in which they were shipped and stored. Because of possible material losses during filtration (i.e., entrapment in the filter), absorbance for QY calculations was determined at the beginning of each filtration cycle. Thus, the reported values are concentration-corrected.

All samples experienced reductions in total fluorescence intensity (Figure 8**,** Figure 27), in some cases by as much as 96% (Vendor 4), which could result from either loss in the filter or reduction in QY. Specific investigation of QY indicated modest declines (Table 1), suggesting that much of the reduction in fluorescence intensity reflects material loss on the filter. Sample QY was generally stable against a single filtration cycle; however, samples from Vendors 2-4 displayed statistically significant reductions in QY with increasing numbers of washes. QDs from Vendor 1 displayed mixed results, although they were more

resistant to QY reduction than all competing vendors. QDs from Red Lot #1 demonstrated a statistically significant reduction in QY after 3 washes, whereas as Red Lot #2 and the Green Lot did not demonstrate reduced QY across the three washes performed. For green QDs; however, sample-to-sample variation, reflected by their relatively larger standard deviations, was consistently observed (Table 1). This is consistent with the larger variations observed in our dilution study as well. However, conclusive results would require a larger study with multiple lots from each vendor. As in our previous studies, aggregation was not observed across all experiment conditions, suggesting colloidal stability in original aqueous media was not affected by centrifugation or filtration steps.

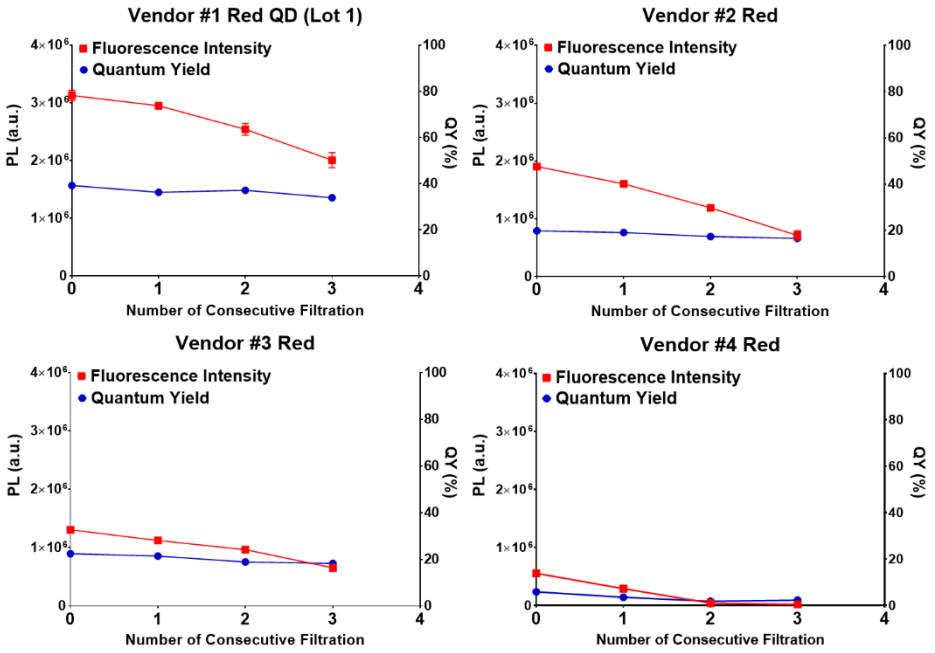

Figure 8 Photoluminescence (PL) intensity and QY of red QDs from four vendors (fixed concentration) after centrifugal filtration repeated up to 3 times.

Table 1 QY of QDs Following Centrifugal Filtration and QDs in Different Buffers

Filtration	**Vendor 1 Red, Lot 1** (0.1 µM)	**Vendor 1 Red, Lot 2** (0.1 µM)	**Vendor 1 Green** (0.25 µM)	**Vendor 2 Red** (0.1 µM)	**Vendor 3 Red** (0.06 µM)	**Vendor 4 Red** (0.5 µM)
Pre-Wash°	39.2 ± 0.9	40.0 ± 2.7	54.8 ± 4.7	19.82 ± 2.1	22.5 ± 0.5	5.9 ± 0.1
Wash 1	36.3 ± 0.9	41.4 ± 1.4	57.3 ± 2.8	19.06 ± 0.6	21.4 ± 0.3	3.5 ± 0.3*
Wash 2	37.1 ± 0.4	41.9 ± 1.2	57.4 ± 5.0	17.4 ± 0.3*	18.9 ± 0.4*	1.8 ± 0.2*
Wash 3	33.9 ± 0.8*	40.9 ± 0.9	55.8 ± 3.3	16.6 ± 0.6*	18.3 ± 0.3*	2.3 ± 1.5*
Buffer	**Vendor 1 Red Lot 1** (0.1 µM)	**Vendor 1 Red Lot 2** (0.1 µM)	**Vendor 1 Green** (0.25 µM)	**Vendor 2 Red** (0.1 µM)	**Vendor 3 Red** (0.06 µM)	**Vendor 4 Red** (0.5 µM)
Borate pH 9, 50 mM	33.9 ± 0.8	41.0 ± 0.9	55.8 ± 3.3°	24.12 ± 0.8*	17.2 ± 0.7*	3.1 ± 0.1*
Water	36.4 ± 0.5*	33.7 ± 0.6*	52.1 ± 2.0*	19.8 ± 0.2	22.5 ± 0.5	3.5 ± 0.3
MES pH 4.7, 0.1 M	Aggregation	Aggregation	Aggregation	13.6 ± 0.7*	17.3 ± 0.05*	1.1 ± 0.2*

°As reported in Figures 1,S2; *indicates statistical difference ($\alpha = 0.05$) from pre-wash values

*indicates statistical difference ($\alpha = 0.05$) between QY before and after buffer exchange

Because QY values are concentration corrected, these losses cannot be attributed to product loss during washing. Thus, the most likely cause for reduced QY during centrifugal filtration is loss of surface ligand, which is a well-documented problem during solution exchanges.[68] However, QY reductions were not observed with sample dilution, which would have been expected if ligand loss were driven by equilibrium reactions alone. We hypothesize that ligand loss could occur during centrifugal filtration, but not dilution, because of the additional shear forces applied during this process. This hypothesis could be further confirmed by quantitative NMR experiments to examine ligands on the QD

surface.[79] An alternative possible cause of reduced QY is surface oxidation[80], which could be evaluated using x-ray photoelectron spectroscopy or cathodoluminescence[81]. It is notable; however, that the surface changes that resulted in reduced QY did not result in reduced colloidal stability as no aggregation was observed throughout the study. These data suggest that filtration steps should be limited in number to reduce QY losses throughout the purification process.

Effect of Buffer Exchange

Bioconjugation protocols are typically performed in buffers such as MES[70], although some QD vendors recommend borate buffer. Biological buffers inherently present solutions with different pH and ionic strength than water, and as such could affect colloidal stability.[77] Thus, we examined the effect of QD dissolution in: water; pH 9, 50 mM borate buffer (i.e., recommended by one vendor for bioconjugation); and pH 4.7, 0.1 M MES buffer (consistent with common bioconjugation protocols[70]) to examine the effect of dispersing QDs in solvents with different pH and ionic strengths. Buffer exchange was performed using centrifugal filtration to reduce the volume of the original solvent, followed by dispersion in the new solvent. Three washes in the new solvent were performed before measurement to ensure removal of residual solvent. QD concentrations employed were consistent with those used in the centrifugal filtration study.

Products generally displayed highest QYs in the buffers in which they were supplied (i.e., either water or borate buffer) (Figure 9 and Table 1). Thus, there were no trends across all 4 vendors indicating an ideal buffer that maximized QY for all products. However, dissolution in MES buffer, recommended in many bioconjugation protocols, yielded

decreased stability or statistically significant declines in QY for all products tested. QDs from Vendor 1, regardless of lot number or color, aggregated instantaneously in MES buffer (Figure 28). QDs from vendors 2 and 4 did not demonstrate visible aggregation, but fluorescence emission peaks were red-shifted, suggesting aggregation. QYs for QDs from these two vendors were also reduced, although by levels roughly consistent with those observed in response to centrifugal filtration (3 washes), suggesting that these QY losses most likely result from centrifugal filtration processes and not buffer incompatibility. QDs from Vendor 3 did not present observable aggregation or red-shifted emission peaks; however, there was a slight, statistically significant decline in QY compared to that in other buffers. This decline was consistent with that observed during centrifugal filtration studies, and most likely can be attributed to purification rather than buffer incompatibility. To evaluate the effect of pH, in a more limited set of samples, we examined QD compatibility with pH 7.4, 50 mM borate buffer, which was recommended by one of the vendors as a conjugation buffer (Figure 29). QD samples from Vendor 1 (Lot 2) and Vendor 2 were stable in pH 7.4 borate buffer, consistent with prior results using pH 9, 50 mM borate, and did not demonstrate statistically significant differences in QY from measurements conducted in their original buffers.

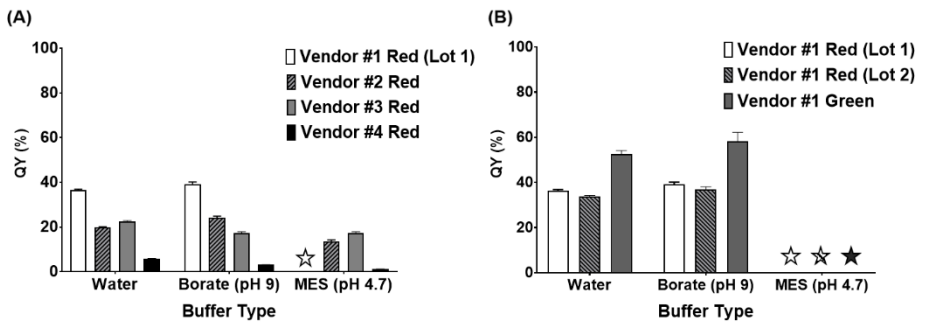

Figure 9 QY of (a) red QDs from four vendors in different buffers and (b) from vendor 1: red QDs, lots 1 and 2 and green QDs. Star indicates that significant aggregation was observed, precluding measurement of QY.

Colloidal stability is typically inversely proportional to ionic strength, with increasing ionic strength yielding greater Debye screening and therefore reduced colloidal particle stability.[77] However, the buffers used in this study had ionic strengths of 4.7 mM and 104.1 mM for MES and pH 9 borate buffers, respectively. Thus, QDs in borate buffer would be expected to demonstrate the least colloidal stability, which is contradictory to our findings. These results indicate that buffer incompatibility, separate from that attributed to ionic strength, can induce aggregation of commercial QD products (Vendors 1, 2, and 4 in MES buffer), and should be carefully considered when designing QD conjugation protocols.

Conclusion

This study evaluated the colloidal stability and QY of –COOH terminated CdSe/ZnS QDs from 4 commercial vendors. These materials were chosen because they are the most

common QDs employed in biological imaging studies. Three processes required in bioconjugation protocols were examined: dilution in the manufacturer's original buffer, purification via centrifugal filtration, and dilution in biological buffers employed in bioconjugation protocols. Across the range of concentrations investigated, all products investigated demonstrated unchanged QY and no aggregation upon dilution in the solvent in which they were shipped. Further, although limited investigation was performed, no lot to lot variation was observed. However, the measured QYs for nearly all vendors were lower than those reported by the manufacturers. This may result from the method of measurement. The most significant declines in QY were observed in response to centrifugal filtration, with declines increasing as a function of increasing number of wash cycles. The most significant declines in colloidal stability were observed in MES buffer. These data suggest caution in developing bioconjugation protocols, which should employ the minimum number of purification and washing cycles. Further, in this limited study, ionic strength was not a predictor of QD stability in a given buffer. Thus, care should be taken to evaluate stability experimentally when developing a new protocol. These results provide some of the first systematic investigation of stability and QY for commercial QD products during preparation steps for biological use.

References

59. Lee, K. H., Porter, T. & Winter, J. O. Fluorescence loss of commercial aqueous quantum dots during preparation for bioimaging. *MRS Commun.* **9**, 702–709 (2019).
60. Chan, W. C. W. & Nie, S. Quantum dot bioconjugates for ultrasensitive nonisotopic detection. *Science (80-.).* **281**, 2016–2018 (1998).
61. van Sark, W. G. J. H. M., Frederix, P. L. T. M., Bol, A. A., Gerritsen, H. C. & Meijerink, A. Blueing, Bleaching, and Blinking of Single CdSe/ZnS Quantum

Dots. *ChemPhysChem* **3**, 871–879 (2002).
62. Wu, X. *et al.* Immunofluorescent labeling of cancer marker Her2 and other cellular targets with semiconductor quantum dots. *Nat. Biotechnol.* **21**, 41–46 (2003).
63. Dubertret, B. *et al.* In vivo imaging of quantum dots encapsulated in phospholipid micelles. *Science (80-.).* **298**, 1759–1762 (2002).
64. Shiohara, A., Hoshino, A., Hanaki, K. I., Suzuki, K. & Yamamoto, K. On the cyto-toxicity caused by quantum dots. *Microbiol. Immunol.* **48**, 669–675 (2004).
65. Ye, L. *et al.* A pilot study in non-human primates shows no adverse response to intravenous injection of quantum dots. *Nat. Nanotechnol.* **7**, 453–458 (2012).
66. Grim, J. Q., Manna, L. & Moreels, I. A sustainable future for photonic colloidal nanocrystals. *Chem. Soc. Rev.* **44**, 5897–5914 (2015).
67. Banerjee, A. *et al.* Fast, Efficient, and Stable Conjugation of Multiple DNA Strands on Colloidal Quantum Dots. *Bioconjug. Chem.* **26**, 1582–1589 (2015).
68. Aldana, J., Wang, Y. A. & Peng, X. Photochemical instability of CdSe nanocrystals coated by hydrophilic thiols. *J. Am. Chem. Soc.* **123**, 8844–8850 (2001).
69. Zhang, Y., Chen, Y., Westerhoff, P. & Crittenden, J. C. Stability and removal of water soluble CdTe quantum dots in water. *Environ. Sci. Technol.* **42**, 321–325 (2008).
70. Hermanson, G. T. *Bioconjugate techniques*. (Academic Press, 1996).
71. Kubin, R. F. & Fletcher, A. N. Fluorescence quantum yields of some rhodamine dyes. *J. Lumin.* **27**, 455–462 (1982).
72. Velapoldi, R. A. Considerations on organic compounds in solution and inorganic ions in glasses as fluorescent Standard Reference Materials. *J. Res. Natl. Bur. Stand. (1934).* **76A**, 641 (1972).
73. Wu, Y. *et al.* The development of quantum dot calibration beads and quantitative multicolor bioassays in flow cytometry and microscopy. *Anal. Biochem.* **364**, 180–192 (2007).
74. Gaigalas, A. K. & Wang, L. Measurement of the fluorescence quantum yield using a spectrometer with an integrating sphere detector. *J. Res. Natl. Inst. Stand. Technol.* **113**, 17–28 (2008).
75. Deerinck, T. J. The Application of Fluorescent Quantum Dots to Confocal, Multiphoton, and Electron Microscopic Imaging. *Toxicol. Pathol.* **36**, 112–116 (2008).
76. Winter, J. O., Liu, T. Y., Korgel, B. A. & Schmidt, C. E. Recognition Molecule Directed Interfacing Between Semiconductor Quantum Dots and Nerve Cells. *Adv. Mater.* **13**, 1673–1677 (2001).
77. Pfeiffer, C. *et al.* Interaction of colloidal nanoparticles with their local environment: The (ionic) nanoenvironment around nanoparticles is different from bulk and determines the physico-chemical properties of the nanoparticles. *Journal of the Royal Society Interface* **11**, 20130931–20130931 (2014).
78. Moore, T. L. *et al.* Nanoparticle colloidal stability in cell culture media and impact on cellular interactions. *Chem. Soc. Rev.* **44**, 6287–6305 (2015).
79. Wang, F., Tang, R. & Buhro, W. E. The trouble with TOPO; identification of

adventitious impurities beneficial to the growth of cadmium selenide quantum dots, rods, and wires. *Nano Lett.* **8**, 3521–3524 (2008).
80. Van Sark, W. G. J. H. M. *et al.* Photooxidation and photobleaching of single CdSe/ZnS quantum dots probed by room-temperature time-resolved spectroscopy. *J. Phys. Chem. B* **105**, 8281–8284 (2001).
81. Rodriguez-Viejo, J. *et al.* Cathodoluminescence and photoluminescence of highly luminescent CdSe/ZnS quantum dot composites. *Appl. Phys. Lett.* **70**, 2132–2134 (1997).

Chapter 4. Biomolecular detection, tracking, and manipulation using a magnetic nanoparticle-quantum dot platform

This chapter describes a magneto-fluorescent detection and separation platform based on quantum dots and superparamagnetic iron oxide nanoparticles applied to protein and DNA. This study was funded by NSF CMMI-0900377, DMR-1206745, EEC-0914790, DMR-0820414, the U. S. Army Research Office under Contract W911NF-10-1-053; the Ohio State University Nanoscale Science and Engineering Center for Affordable Nanoengineering of Polymeric Biomedical Devices, Materials Science and Engineering Research Center for Emergent Materials, and the Institute for Materials Research; a ‘‘Thousand Young Global Talents’’ award from the Chinese Central Government; Nanjing University; and the ‘‘Tian-Di’’ Foundation, College of Modern Engineering and Applied Sciences, Nanjing University, China. Preparation of nanoparticle probes was conducted by Dr. Kalpesh Mahajan and Dr. Gang Ruan. Fabrication of magnetic traps was conducted by Dr. Greg Vieira. Dr. Kalpesh Mahajan, Dr. Gang Ruan, and Dr. Greg Vieira contributed to experimental design, data collection and analysis, and writing. Mean-squared displacement data analysis, figure production, and final editing of the manuscript was conducted by Thomas Porter. The introduction was written by Thomas Porter and edited by Dr. Jessica Winter. This chapter is published as a manuscript in Mahajan KD, Ruan G, Vieira G, Porter T, Chalmers JJ, Sooryakumar R, Winter JO, “Biomolecular Detection, Tracking, and Manipulation using a Magnetic Nanoparticle-Quantum Dot Platform.” J. Mater. Chem. B, (2020).[82]

Introduction

Fluorescence and magnetism have long been used for real-time detection and quantification of molecules. Efforts to improve these technologies have typically focused on increasing sensitivity, specificity, and multiplexing capability. Quantum dots (QDs), with their broad absorption cross-section, narrow emission spectra, and photostability, have attracted significant attention for fluorescent labelling applications.[83] For sensing, QDs have been applied using techniques such as Förster resonance energy transfer (FRET),[84] fluorescence ratiometry, electrochemiluminescence, and photo-electrochemistry.[85] Concurrently, superparamagnetic iron oxide nanoparticles (SPIONs) have been applied in imaging, manipulation, and biosensing.[86] For sensing, SPIONs are most commonly used to 1) move and/or concentrate a targeted entity or 2) to detect analytes based on their paramagnetic properties. For both applications, SPION properties are critical features, combined with the magnitude of the magnetic energy gradient and/or detection instrument.[87] For example, analytes can be detected directly via superconducting quantum interference devices (SQUID) analysis of SPION-labelled entities.[88] However, these platforms typically lack multiplexing capability, and are hence unable to perform simultaneous sensing and manipulation operations. Further, the current practical size for individual SPIONs used in these applications is ~ 20 nm.[89] However, many individual, small SPIONs can also be combined into a larger aggregate to achieve an effective increase in magnetic volume.[90]

Recently, several groups have developed multimodal detection probes that combine QDs and SPIONs for simultaneous molecular sensing and manipulation.[91] Detection mechanisms can include QD fluorescence quenching by electron and energy transfer

mechanisms or direct fluorescent labelling, whereas magnetic capability is employed for analyte separation. However, many of these schemes employ heterofunctional composite nanoparticles (NPs), such as core-shell structures,[92,93] which can yield false positive binding events. Such platforms may lack sensitivity and specificity.

Based on our development of polymer micelle-NP encapsulant composite materials, we developed a versatile technology that utilizes SPION and QD micelles and engineered magnetic fields to simultaneously manipulate and track different biomolecules in parallel. This approach groups together several individual QD or SPION encapsulants, increasing QD fluorescence signal[94] and the cumulative magnetic volume[90]. In this approach, individual micelles containing multiple QDs or SPIONs are conjugated to molecules that detect the analyte, but do not target each other. These micelle "bricks" are thus assembled into hierarchical structures by binding target analyte "mortars" (Figure 10), whose size is limited by the available analyte concentration. This approach permits detection via fluorescent signals, measurement of hierarchical structure size, and magnetic quantification, a tri-fold duplication of signals that could be used for internal quality control. Further, unlike approaches that rely on detection alone, this approach permits isolation and quantification of target biomolecules. False positives are reduced by the requirement of both fluorescent and magnetic micelle binding events to register a detection event.

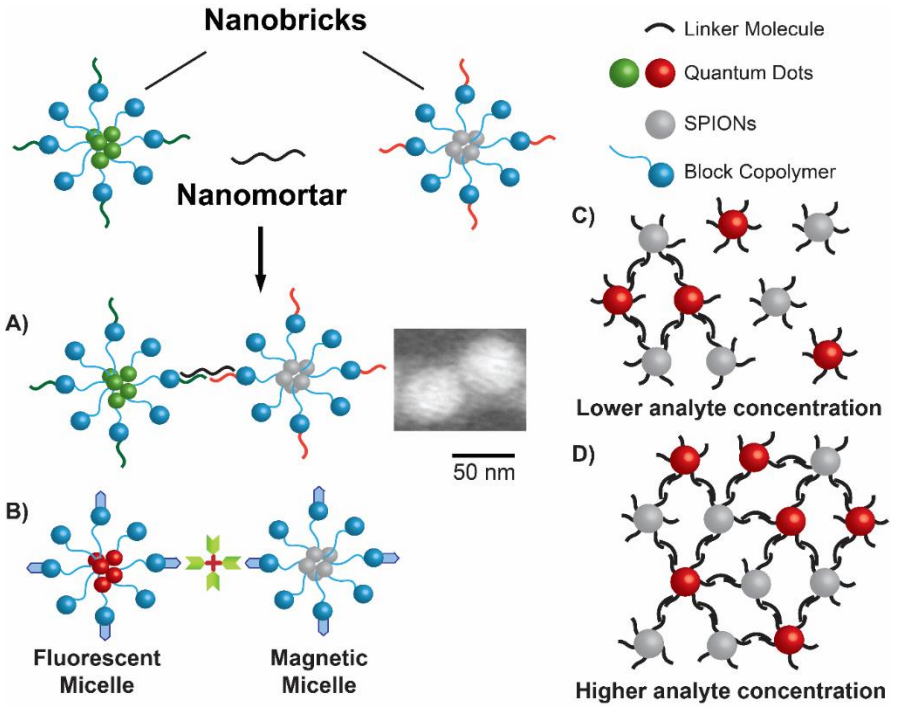

Figure 10 Micelle-Based Aggregation Assay. A detection event occurs when a fluorescent micelle and magnetic micelle both bind to (A) DNA or (B) protein analytes, forming a (C, D) hierarchical material. As analyte concentration increases, additional micelles join the aggregate. Green and red QD micelles were used for ssDNA and protein analytes, respectively.

Here, we implemented this scheme to detect model streptavidin protein and p53 DNA analyte molecules via assembly of QD-SPION composite materials. The resulting fluorescent and magnetic structures were transported, manipulated, and separated via user-controlled magnetic fields that acted on SPION constituents, whereas fluorescent QD components permitted analysis and quality control through real-time optical characterization. To determine sensitivity, we compared analyte concentration against a

fluorescence standard curve, whereas to measure specificity we examined detection of complimentary DNA vs. DNA with 1 or 2 base pair mismatches. Parallel and sequential separation of different biomolecules was also demonstrated by concurrent or sequential addition of functionalized SPION micelles. Thus, this approach complements existing detection platforms by enabling simultaneous separation and detection, which can be multiplexed to simultaneously detect both proteins and DNA, and provides multiple potential measurement modalities for internal quality control.

Materials and Methods

Materials

Quantum dots supplied in decane (λ_{em} = 545 nm (green), Cat No. Q21791MP and λ_{em} = 605 nm (red), Cat No. Q21701MP), N-(3-Dimethylaminopropyl)-N'-ethylcarbodiimide hydrochloride (EDC) (Cat No. 22980), sulfo-N-hydroxysuccinimide (sulfo-NHS) (Cat No. 24510), and pentyl-amine biotin (Cat No. 21345) were purchased from ThermoFisher Scientific (Waltham, MA). 5nm SPIONs (Cat No. SOR-05-50) were purchased from Ocean NanoTech (San Diego, CA). Carboxyl-terminated poly(styrene-b-ethylene oxide) PS(9500)-b-PEO(18000) (Cat No. P5755-SEOCOOH) was purchased from Polymer Source, Inc. (Dorval, QC, Canada). Poly(vinyl alcohol) (PVA, 13,000-23,000 Dalton, 87-89% hydrolyzed, Cat No. 363170), MES buffer (2-(N-morpholino)ethanesulfonic acid (Cat No. M8902), and ssDNA were purchased from Sigma Aldrich (St. Louis, MO). Thiol

functionalized methoxy polyethylene glycol (Cat No. MPEG-SH-5000) was purchased from Laysan Bio, Inc (Arab, AL).

Micelle Synthesis

As described previously[94,95], the interfacial instability approach was used to synthesize micelles containing either QDs or SPIONs. For QDs, stock solutions as supplied by the manufacturer in decane were first transferred to chloroform. QDs (100 µl) were precipitated by adding 450 µl of a 1:2 isopropanol: methanol solution. The pellet was then re-suspended in chloroform to a concentration of 0.1 µM. SPIONs were directly dissolved in chloroform at 3.45 µM. Carboxyl-terminated poly(styrene-b-ethylene oxide) PS(9500)-b-PEO(18000) at 36.4 µM in chloroform was used to encapsulate NPs. The aqueous phase consisted of poly(vinyl alcohol) (PVA) dissolved in water at 5 mg/ml. Micelles were generated by mixing 10 µl polymer solution and 200 µl of QD or SPION solution with 800 µl of the aqueous PVA phase via sonication. Mixtures were left to evaporate for 1-2 hours; formation of a clear, transparent solution indicated successful encapsulation and micelle formation. Micelles can be stable for weeks to months, depending on synthesis conditions.[96]

Micelle Bioconjugation

As model systems, biotin was used to capture avidin proteins and p53 DNA was used as a DNA analyte. For avidin protein detection, both QD (red) and SPION micelles were functionalized with biotin. For p53 DNA detection, QD (green) and SPION micelles were functionalized with distinct ssDNA sequences (Table 2) that do not bind each other, but hybridize with the same target DNA sequence derived from the mRNA of the tumor

suppressor protein p53 (NCBI ref. seq. NM_000546.4). In addition, capture experiments were conducted with single and double mutation sequences to assess specificity. Mutation locations were chosen randomly, but were excluded from ssDNA locations near NP attachment points.

Table 2 NP and Analyte DNA Sequences

ssDNA	*Sequence*[a]
QD	NH_2C_6-TGAAACGCAAGCCCGA
SPION	CCCTGACCTAACCGCC-C_7NH_2
Target	ACTTTGCGTTCGGGCTGGGACTGGATTGGCGG
1 bp mut.	ACTTTG**T**GTTCGGGCTGGGACTGGATTGGCGG
2 bp mut.	ACTTTG**T**GTTCGGGCTGGGACTGGATTGG**A**GG

[a]Mut. = Mutations, indicated with bold characters. Same colours indicate complimentary sequences.

Micelles were modified with either protein or ssDNA using N-(3-Dimethylaminopropyl)-N'-ethylcarbodiimide hydrochloride (EDC) chemistry.[15] First, carboxylated micelles synthesized in water were re-suspended in pH 5.7 MES buffer. Then, this solution was mixed with EDC, sulfo-NHS, and pentyl-amine biotin or ssDNA at a molar ratio of 1:1000:2500:100 corresponding to micelles: EDC:sulfo-NHS:Biotin or ssDNA. After overnight incubation at room temperature, conjugated micelles were purified by dialysis against distilled, deionized water.

Transmission Electron Microscopy (TEM)

Samples were prepared by placing 10 µL of sample onto a silicone pad. Transfer to formvar/carbon-coated nickel grids was achieved by exposing the grids to the sample droplet for 2 minutes. Samples were negatively stained using phosphotungstic acid (PTA, 1%) by placing the grid on a 10 µl droplet for 2 minutes. Excess PTA was removed with

filter paper. Micelles and micellar aggregates were then imaged using a FEI Tecnai G2 Bio Twin TEM.

Dynamic Light Scattering (DLS)

Hydrodynamic particle size was characterized using dynamic light scattering (Brookhaven Instruments Corporation, BI 200SM). Sample concentration was adjusted by addition of water to obtain a scattered light intensity between 10 and 200 kCPS (kilo-counts per second) at a laser wavelength of 633 nm and a detection angle of 90°. Number weighted size was measured for each sample. The size of the micelle composites for each analyte concentration was measured in triplicate, and each replicate was measured three times; the average value was recorded.

Fluorescence Imaging

Samples were imaged using a 100x oil immersion objective on an Olympus IX71 fluorescent microscope. A 100 W mercury lamp was used to generate excitation at λ_{ex} = 488 nm, and a long-pass emission filter was employed to collect emission signal. Images were collected with an Olympus DP70 CCD camera or an EMCCD camera (Photometrics, AZ) with Metamorph software. All image processing and analysis were performed using NIH ImageJ software.

Fluorescence Intensity Quantification and Measurement of Limit of Detection

QD and SPION micelles were used as prepared, at an estimated concentration of 7×10^{-10} M. For each experiment, micelles were incubated with analyte (10^{-10} - 10^{-18} M) for ~ 20 min. Then, micelle aggregates were viewed on an Olympus IX71 fluorescence microscope equipped with an Evolve Photometrics EMCCD camera. A stream acquisition of 50 images

was recorded for each location, and at least 3 locations were analyzed for each concentration. Each fluorescent spot was circled in ImageJ and the total fluorescence intensity was determined. The highest value of total fluorescence intensity among 50 frames was recorded to eliminate interference from QD blinking among constituent particles. This value was compared to that obtained for a single micelle using the same procedure to determine the number of QD micelles bound. The first fluorescence concentration that could be distinguished from that of the control with no analyte was reported as the limit of detection.

Particle Tracking

Hierarchical aggregate trajectories were analyzed using MTrackJ plugin[97] available in ImageJ. Particle sizes were obtained from the mean square displacement (MSD) using the Stokes-Einstein equation as described previously.[98] Briefly, the 2D mean squared displacement was calculated by tracking the location of fluorescent aggregates. The diffusion coefficient was then calculated as follows:

$$\boldsymbol{MSD = 4Dt} \quad \text{Equation 4.1}$$

where $\boldsymbol{D}$ is the diffusion coefficient, and $\boldsymbol{t}$ is time.[99] Then, the Stokes-Einstein equation was applied to determine particle size:

$$\boldsymbol{D = \frac{k_b T}{3\pi\mu d_p}} \quad \text{Equation 4.2}$$

where $\boldsymbol{D}$ is the diffusion coefficient, $\boldsymbol{k_b}$ is Boltzmann's constant, $\boldsymbol{T}$ is the temperature, $\boldsymbol{\mu}$ is the viscosity, and $\boldsymbol{d_p}$ is the particle diameter.

Fabrication of Magnetic Traps

Nano-composites were trapped and manipulated using a nano-scale magnetic platform consisting of patterned wires or disks in the presence of programmable magnetic fields (Figure 30). The wires and disks were patterned on silicon wafers using electron beam lithography. Two layers of e-beam resist (methylmethacrylate and polymethyl methacrylate) were spin-coated onto the silicon wafer, baked, and exposed to electron beams which draw the desired patterns. Following development, a 40 nm-thick layer of magnetic material was deposited using magnetron sputtering. (The magnetic material used was chosen based on magnetic coercivity. For wires, $Co_{0.5}Fe_{0.5}$ was chosen so that magnetic domains would remain mostly unchanged during experiments, whereas for disks, $Ni_{0.8}Fe_{0.2}$ was chosen so that disk magnetic domains could be easily rotated.) The e-beam resist and excess magnetic material were lifted off with acetone. The wires (but not disks) were initially magnetized in a desired orientation by applying a temporary ~1 kOe external magnetic field. To minimize surface adhesion and non-specific binding, a 1 nm seed layer of $Ni_{0.8}Fe_{0.2}$ and a 5 nm layer of Au was sputtered atop the entire surface, followed by self-assembly of a thiol-bound PEG monolayer.

Magnetic Manipulation of Particles and Assemblies

The trapping platform consisted of a patterned silicon wafer as well as four electromagnets and one wire coil (Figure 31). Programmable electrical currents passing through the electromagnets and coil were used to control magnetic fields in three dimensions. The four electromagnets applied field components in the plane of the wafer, whereas the wire coil surrounded the wafer and applied an out-of-plane field component. The out-of-plane field

served to strengthen or weaken traps that existed at wire vertices or at the peripheries of disks, whereas the in-plane fields guided the movement of particles manipulated across the silicon wafer.[100] The wafer was placed beneath a 100x oil immersion objective lens in an Olympus microscope, where fluorescence imaging was performed. Images and videos were recorded using an Olympus DP70 CCD camera.

For each experiment, QD and SPION micelles were used as prepared, at an estimated concentration of 7×10^{-10} M. Analyte concentration (i.e., 10^{-10} M) was chosen such that the magnetic strength of the micelle aggregates was sufficient to easily manipulate them. Micelles and analytes were incubated together for ~ 20 min. prior to magnetic capture. Three different experiments were performed. In the first experiment, magnetic manipulation of magnetic-fluorescent aggregates formed in the presence of ssDNA analytes was demonstrated on both disk and nanowire platforms to provide proof of concept. In the second experiment, avidin and ssDNA analytes were added together with their respective complementary particles and simultaneous magnetic manipulation of DNA and protein on a nanowire platform was shown. In the third experiment, avidin and ssDNA analytes were added sequentially and sequential manipulation of protein and DNA analytes was shown on a nanowire platform.

Results and Discussion

Hierarchical Assembly of Micelle "Bricks" with Analyte "Mortar"

Multiple QD or SPION NPs were incorporated into individual micelles through the self-assembly of amphiphilic polymers in an aqueous environment.[94,95] QD micelle sizes were extensively analyzed previously.[94] SPION micelles were spherical and ~40 nm in diameter

(i.e., 42 ± 13 nm) as confirmed by DLS and transmission electron microscopy TEM (Figure 11), consistent with sizes of QD micelles. This approach overcomes some limitations of using individual SPIONs by aggregating multiple SPIONs together to increase overall magnetic volume and therefore magnetic susceptibility.

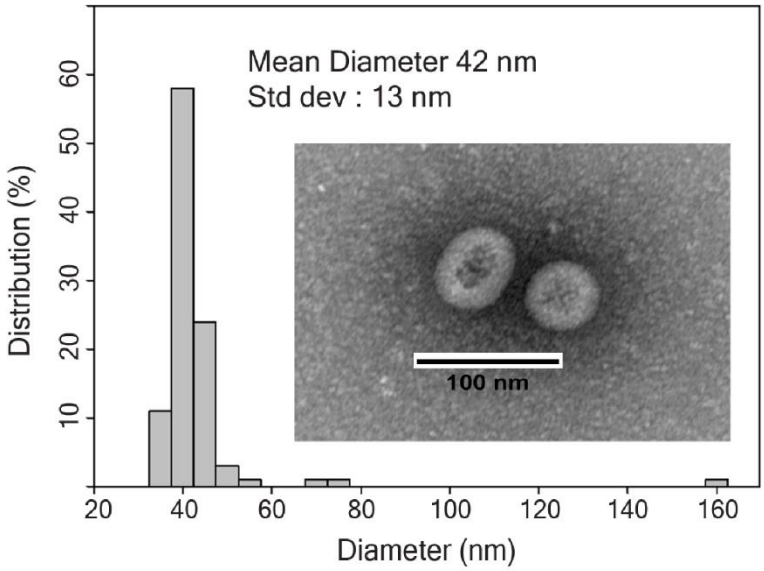

Figure 11 Dynamic light scattering (DLS) and transmission electron microscopy (TEM) analysis of SPION micelle size indicated an average size of 42 ± 13 nm, similar to that of QD micelles.

Individual micelle "nano-bricks" were assembled into hierarchical structures using analyte "nano-mortars" comprised of avidin proteins or ssDNA derived from the p53 mRNA sequence. These hierarchical structures, containing both fluorescent QD and magnetic SPION micelles (e.g., Figure 10 schematic) were ~50-200 nm in diameter. Using ssDNA analytes for proof of concept, aggregate size and fluorescence intensity were demonstrated

to be dependent on the concentration of the analyte mortar (Figure 12). QD fluorescence intensity was correlated with aggregate size as measured via aggregate particle tracking, and few aggregates > 100 nm were observed (Figure 32). At micelle concentrations of ~ 10^{-10} M, nanoassemblies could be formed in solutions as dilute as 10^{-16} M (i.e., 0.1 fM) (i.e., fluorescence limit of detection), which is improved compared to similar magnetic aggregation assays (e.g., 100 pM[101]). These results are also consistent with state-of-the art QD assays that, unlike our aggregation-based system, are based on Förster Resonance Energy Transfer (FRET) (e.g., ~ fM[102]).

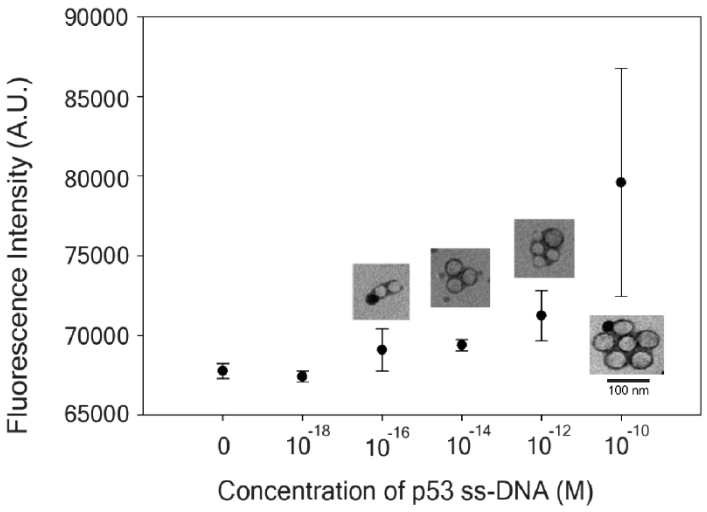

Figure 12 Nanoassembly size increases with increasing target biomolecule concentration (i.e., "nanomortar", here, p53 single stranded DNA). Insets: Representative TEM images of nanoassemblies at the corresponding concentrations of p53 single stranded DNA. (Micelle concentration ~ 7 x 10^{-10} M)

Magnetic Collection of Assemblies and Analyte Detection

The proposed approach permits not only detection, but also magnetic isolation of analytes through the use of user-controlled magnetic fields. Engineered magnetic gradients[95,100] exerted forces on nanoassembly constituent SPIONs to generate motion in a desired direction. Controlled motions across a surface were the result of adding a tunable, weak electromagnetic field to the strong, arrayed magnetic field gradients of a micro-patterned magnet chip.[95,100] As an example, assembly circular motion was induced using micropatterned magnetic disk arrays (Figure 13A, Appendix E Supplementary Video 1), and translational motion was induced via vertex-to-vertex hopping along micropatterned magnetic zigzag wires (Figure 13B, Appendix E Supplementary Video 2). Typically, ~85% of the fluorescent spots trapped at magnetic vertices (e.g., hybridized nanoassemblies) responded to the modulation of the tunable weak electromagnetic field by moving with similar velocity vectors. Nanoassemblies that did not move in a synchronized fashion were most likely agitated by occasional liquid flow. Although not investigated here, this suggests that liquid flow could also be exploited to provide additional transport modalities through microfluidics, potentially permitting platform integration with existing lab-on-a-chip devices.

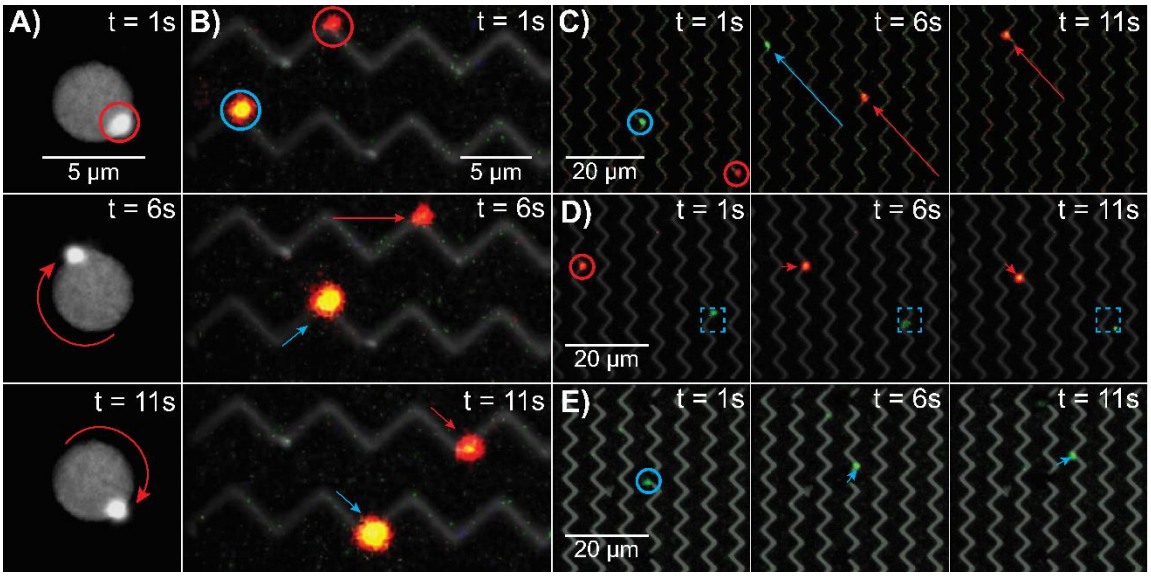

Figure 13 Trapping, transport, and manipulation of composite nanoassemblies (A) on micro-disks, (B) micro-wires, and (C-E) with multiplexing (i.e., still frame images from Appendix E Supplementary Videos 1-5). In (A) and (B), fluorescent-magnetic nanoassemblies (molecular target: p53 ssDNA, 10^{-10} M) moved around micro-disks and between zigzag micro-wires, respectively, via investigator-controlled modulation of the magnetic field. (C) Red avidin protein (10^{-10} M) and green p53 DNA (10^{-10} M) nanoassemblies were simultaneously transported via investigator-controlled vertex-to-vertex hopping. (D, E) Sequential separation of protein and DNA-based nanoassemblies. (D) Red, magnetic avidin protein nanoassemblies were transported via investigator-controlled vertex-to-vertex hopping, whereas green, non-magnetic p53 DNA nanoassemblies (lacking the magnetic SPION component) moved only as a result of Brownian motion or liquid flow. (E) Green, magnetic p53 DNA nanoassemblies were then formed on the same sample by the addition of complimentary DNA-SPIONs, which were transported via investigator-controlled vertex-to-vertex hopping. The arrows in (A-E)

indicate movement of nanoassemblies from the previous frame and are color-coded to represent distinct assemblies.

Key to this approach is the ability to tune the electromagnetic field via user input, with simultaneous optical readout (via QD fluorescence) of the assembly response. In contrast to manipulation approaches based on scanning probe microscopy[103] and synthetic chemistry[104], the strong and stable fluorescence of QDs[105] enables direct visualization and detection of nanoassembly motion in situ with a fluorescence microscope. The ability to visualize transport and assembly directly also provides a method of quality control in detection. For example, positive detection events required both QD fluorescence and magnetic mobility to indicate nanoassembly formation and thus analyte detection.

These properties were used to assess the sensitivity and specificity of the process. Assemblies that underwent motion in a magnetic field could be characterized via their fluorescence intensity. As a first experiment, ssDNA analyte assemblies were tracked via their fluorescence (Figure 10A). As analyte concentration was increased, assembly size and fluorescence intensity increased (Figure 10C, Figure 10D, Figure 12). Reliable assembly of clusters ranged from 2 to 27 micelles in solutions containing ~300-1000 biomolecules in the 5 µl samples used in this study. Biomolecular detection was achieved without any amplification steps (e.g., polymerase chain reaction), and benefitted from the significant signal amplification arising from multiple QDs encapsulated in each QD micelle. Although future work should investigate random sequences and sensitivity of avidin detection in complex solutions containing additional proteins, no detection event

(i.e., magnetic motion and corresponding fluorescent signal) was recorded for a 32-nucleotide sequence (i.e., p53 ssDNA) with double or single base pair mismatches (Table 2). The high sensitivity and specificity achieved with this small sample volume may be attributed to combining the strong local magnetic field gradients of micro-patterned arrays, which permit isolation of small numbers of biomolecules, and the high fluorescence intensity of constituent QDs, which provide quantitative read-out, into an integrated system.

Multiplexed Collection of Protein and DNA Analytes

This approach also permits simultaneous isolation of both protein and DNA on the same platform. Because constituent QDs exhibit size-dependent fluorescence, a large absorption cross-section, and broad excitation spectra[105], nanoassemblies may be color-coded and their motion simultaneously observed with a single filter set.[95] Color-coded QD-SPION nanoassemblies containing either avidin (red, $\lambda_{emission}$ = 605 nm) or p53 ssDNA (green, $\lambda_{emission}$ = 545 nm) mortars were generated. Red protein and green DNA nanoassemblies were co-transported via investigator-controlled, vertex-to-vertex motions, confirming the ability of this technology to manipulate two types of molecular targets simultaneously (Figure 13C, Figure 14A, Appendix E Supplementary Video 3). These experiments demonstrate that the intrinsic photoluminescent properties of the QD element may be used to visualize multiplexed control of materials transport. In contrast, observation of rapid, dynamic events using molecular dyes would be infeasible because of the time required to collect and superimpose multiple images from separate color channels.

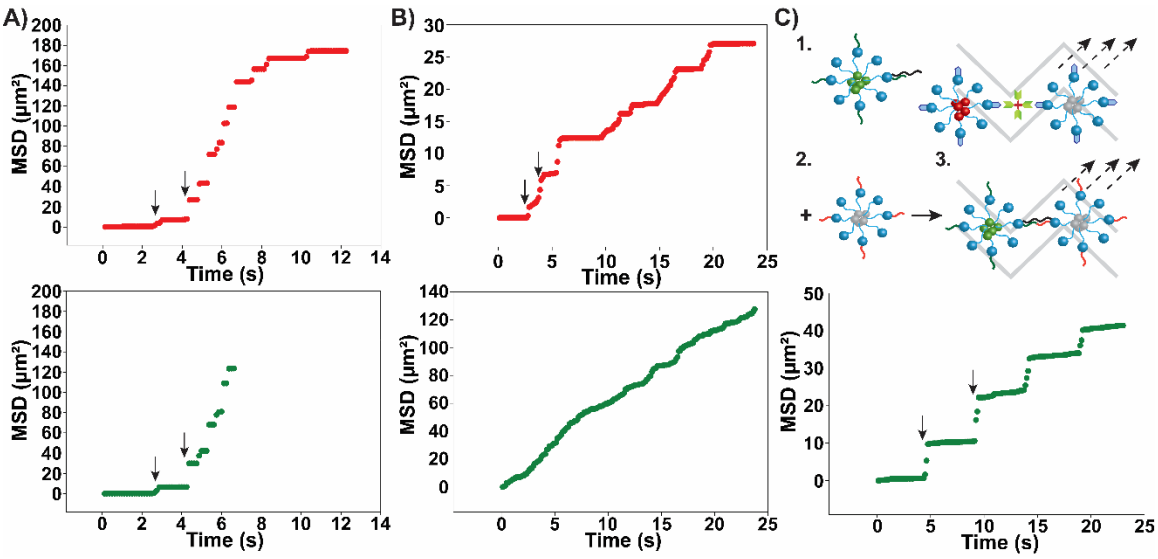

Figure 14 Mean squared displacement (MSD) vs. time for protein (red, upper panel) and DNA (green, lower panel) nanoassemblies. Representative arrows in panels indicate points at which MSD vs. time deviates from the linear trends expected from diffusion alone as a result of vertex-to-vertex hopping induced by user-controlled magnetic fields. Panels A, B, and C correspond to analysis of Figure 13C, D, and E, respectively. (A) Simultaneous transport of protein and DNA assemblies (upper and lower panels) is indicated by deviations from linear MSD (arrows). (B) Sequential magnetic transport of protein assemblies in the presence of DNA assemblies that are not transported is indicated by deviations from linear MSD in the red (upper), but not green (lower) panels. (C) However, when complementary SPIONs are added to green assemblies (lower panel), deviations are restored. Schematic (upper panel) in (C) depicts the process of sequential separation of protein and DNA assemblies.

In addition to simultaneous transport, specific molecules can also be separated from each other. The feasibility of multiplexed separation with simultaneous visualization was confirmed by separating protein and DNA on the same platform. Here, nanoassemblies were sequentially separated using the micro-patterned magnet array (zigzag wire formation) following addition of the complementary SPION-micelle conjugate (i.e., biotinylated-SPION micelles for avidin protein and p53 ssDNA-SPION micelles for p53 DNA). After a short incubation period (~10-30 min), red QD-avidin-SPION nanoassemblies were transported across a distance of 20 μm via investigator-controlled vertex-to-vertex hopping, whereas green QD-p53 DNA-nanoassemblies (containing no magnetic SPION component) remained near their original location, as their motion was subject only to thermal fluctuations, and not magnetic forces from the wires (Figure 13D, Figure 14B, Appendix E Supplementary Video 4).

Some movement resulting from Brownian motion and occasional liquid flow was observed in green p53 DNA composites, which was clearly distinguishable from vertex-to-vertex hopping. Vertex-to-vertex movement by user-controlled magnetic fields was differentiated from movement by diffusion by plotting mean squared displacement (MSD) against time (Figure 14B). MSD vs. time behavior is linear for assemblies undergoing Brownian motion alone (Equation 4.1). In contrast, assemblies undergoing magnetic transport exhibited deviations from linearity during magnetic trapping events at wire vertices. Thus, the motion of assemblies containing only QDs could be clearly distinguished from the motion of assemblies containing both QDs and SPIONs.

Trapping and transport of the red QD-avidin-SPION nanoassemblies (and the lack of trapping and transport for the green assemblies) was confirmed using the color-coded fluorescence signals, suggesting feasibility of one-component separation from a mixed solution. An aqueous solution of p53 ssDNA-SPION-micelles was then added to create green QD-p53-SPION nanoassemblies. Following incubation (~10-30 min), these assemblies were transported similarly to avidin-assemblies using investigator-controlled vertex-to-vertex motion, (Figure 13C and E, Appendix E Supplementary Video 5), thus demonstrating feasibility of separation of different molecules/assemblies from the same solution. Whereas a number of competing technologies also use color-coded signals to identify many different molecules (e.g., Nanostring[106] or Western blots), this approach has the ability to identify and selectively transport and separate different molecules/assemblies. This result is enabled by the sandwich structure (Figure 10) employed for fluorescent-magnetic nanocomposite formation, which takes advantage of the specificity of biomolecular assemblies. Manipulation of analytes at lower concentrations may be feasible by increasing the magnetic strength of the particles.[90] Further, detection speed (i.e., 20 min incubation time) could be reduced by increasing the excess concentration of micelles employed to accelerate binding kinetics.

Conclusions

In this proof of concept work, we demonstrated a magneto-fluorescent detection/ separation platform that (1) performs rapid, sensitive, and specific separation of DNA and/or protein from a 5 µl solution (Speed: Minutes, Limit of Detection: ~0.1 fM via fluorescence, < 0.1 nM via magnetic capture; Sensitivity: No signal for single and double

basepair DNA mutations), (2) continuously visualizes individual molecular separation trajectories, and (3) enables multiplexed imaging and separation of analytes. This approach thus permits hierarchical assembly of structures, with the ability to transport, manipulate, and capture those assemblies in an integrated, parallel, and multiplexed manner. In contrast to force microscopy approaches, individual components are combined using a programmable self-assembly method that does not require external intervention or sequential placement to generate higher-order structures. Thus, directional changes can be induced non-invasively. For future applications, these results should be validated in more complex media, using clinical samples and guidelines. This technology could also be enhanced by incorporation of microfluidics for more sophisticated control of flow on the magnetic arrays and to enable future integration with existing lab-on-a-chip technologies. Thus, this technology platform may enable new opportunities in nanoassembly, molecular separation and analysis, and biomolecular research.

References

82. Mahajan, K. D. *et al.* Biomolecular detection, tracking, and manipulation using a magnetic nanoparticle-quantum dot platform. *J. Mater. Chem. B* (2020). doi:10.1039/c9tb02481f
83. Gao, X., Chan, W. C. W. & Nie, S. Quantum-dot nanocrystals for ultrasensitive biological labeling and multicolor optical encoding. *J. Biomed. Opt.* **7**, 532 (2002).
84. Clapp, A. R. *et al.* Fluorescence Resonance Energy Transfer between Quantum Dot Donors and Dye-Labeled Protein Acceptors. *J. Am. Chem. Soc.* **126**, 301–310 (2004).
85. Wu, P., Hou, X., Xu, J. J. & Chen, H. Y. Ratiometric fluorescence, electrochemiluminescence, and photoelectrochemical chemo/biosensing based on semiconductor quantum dots. *Nanoscale* **8**, 8427–8442 (2016).
86. Gloag, L., Mehdipour, M., Chen, D., Tilley, R. D. & Gooding, J. J. Advances in the Application of Magnetic Nanoparticles for Sensing. *Advanced Materials* **31**, e1904385 (2019).
87. Fratzl, M. *et al.* Magnetophoretic induced convective capture of highly diffusive

superparamagnetic nanoparticles. *Soft Matter* **14**, 2671–2681 (2018).
88. Wang, J., Li, H., Cho, E. Y., Lefebvere, J. C. & Cybart, S. A. Measurement of Magnetic Nanoparticles Using High Transition Temperature Superconducting Quantum Interference Devices. *IEEE Trans. Appl. Supercond.* **29**, 1–4 (2019).
89. Yeap, S. P., Leong, S. S., Ahmad, A. L., Ooi, B. S. & Lim, J. On size fractionation of iron oxide nanoclusters by low magnetic field gradient. *J. Phys. Chem. C* **118**, 24042–24054 (2014).
90. Nabar, G. M., Winter, J. O. & Wyslouzil, B. E. Nanoparticle packing within block copolymer micelles prepared by the interfacial instability method. *Soft Matter* **14**, 3324–3335 (2018).
91. Rong, G., Tuttle, E. E., Neal Reilly, A. & Clark, H. A. Recent Developments in Nanosensors for Imaging Applications in Biological Systems. *Annu. Rev. Anal. Chem.* **12**, 109–128 (2019).
92. Li, L. *et al.* Facile synthesis of magnetic fluorescent nanoparticles: adsorption and selective detection of Hg(ii) in water. *J. Mater. Chem. C* **6**, 2360–2369 (2018).
93. Wu, L. *et al.* Detection of malachite green in fish based on magnetic fluorescent probe of CdTe QDs/nano-Fe3O4@MIPs. *Spectrochim. Acta Part A Mol. Biomol. Spectrosc.* **196**, 117–122 (2018).
94. Ruan, G. & Winter, J. O. Alternating-color quantum dot nanocomposites for particle tracking. *Nano Lett.* **11**, 941–945 (2011).
95. Ruan, G. *et al.* Simultaneous magnetic manipulation and fluorescent tracking of multiple individual hybrid nanostructures. *Nano Lett.* **10**, 2220–2224 (2010).
96. Lee, K. H., Yang, G., Wyslouzil, B. E. & Winter, J. O. Electrohydrodynamic Mixing-Mediated Nanoprecipitation for Polymer Nanoparticle Synthesis. *ACS Appl. Polym. Mater.* **1**, 691–700 (2019).
97. Meijering, E., Dzyubachyk, O. & Smal, I. Methods for cell and particle tracking. in *Methods in Enzymology* **504**, 183–200 (Academic Press Inc., 2012).
98. Duong, A. D., Ruan, G., Mahajan, K., Winter, J. O. & Wyslouzil, B. E. Scalable, semicontinuous production of micelles encapsulating nanoparticles via electrospray. *Langmuir* **30**, 3939–3948 (2014).
99. Wong, M. H. *et al.* Lipid Exchange Envelope Penetration (LEEP) of Nanoparticles for Plant Engineering: A Universal Localization Mechanism. *Nano Lett.* **16**, 1161–1172 (2016).
100. Vieira, G. *et al.* Magnetic Wire Traps and Programmable Manipulation of Biological Cells. *Phys. Rev. Lett.* **103**, 128101 (2009).
101. Schrittwieser, S. *et al.* Homogeneous Biosensing Based on Magnetic Particle Labels. *Sensors* **16**, 828 (2016).
102. Stanisavljevic, M., Krizkova, S., Vaculovicova, M., Kizek, R. & Adam, V. Quantum dots-fluorescence resonance energy transfer-based nanosensors and their application. *Biosensors and Bioelectronics* **74**, 562–574 (2015).
103. Neuman, K. C. & Nagy, A. Single-molecule force spectroscopy: Optical tweezers, magnetic tweezers and atomic force microscopy. *Nature Methods* **5**, 491–505 (2008).
104. Bissell, R. A., Córdova, E., Kaifer, A. E. & Stoddart, J. F. A chemically and

electrochemically switchable molecular shuttle. *Nature* **369**, 133–137 (1994).
105. Rosenthal, S. J., Chang, J. C., Kovtun, O., McBride, J. R. & Tomlinson, I. D. Biocompatible quantum dots for biological applications. *Chem. Biol.* **18**, 10–24 (2011).
106. Geiss, G. K. *et al.* Direct multiplexed measurement of gene expression with color-coded probe pairs. *Nat. Biotechnol.* **26**, 317–325 (2008).

Chapter 5. Compact Quantum Dot Surface Modification to Enable Emergent Behaviors in Quantum Dot-DNA composites

This chapter describes the synthesis of compact quantum dot-DNA conjugates and proof-of-concept experiments demonstrating their potential utility in biosensing applications. This study was funded by NSF DBI-1555470. The aqueous transfer and optimization of carbodiimide chemistry for this study was conducted by Dr. Abhilasha Dehankar and Thomas Porter. The click chemistry scheme for this study was devised by Thomas Porter. The fluorescence resonance energy transfer studies were performed by Dr. Abhilasha Dehankar and DNA origami conjugation was performed by Dr. Joshua Johnson. The first draft of this chapter was authored by Dr. Abhilasha Dehankar. Writing and figure production was done by Dr. Abhilasha Dehankar and edited by Thomas Porter. This chapter is published as a manuscript in Dehankar A*, Porter T*, Johnson JA, Castro CE, Winter JO, (Invited) "Compact Quantum Dot Surface Modification to Enable Emergent Behaviors in Quantum Dot-DNA composites." J. Chem. Phys., 151(14) (2019).[107] *equally contributing authors.

Introduction

Modification of quantum dots (QDs) with single-stranded deoxyribonucleic acid (ssDNA) oligonucleotides is critical to their use in many applications, such as microarray detection[108], Förster resonance energy transfer (FRET)-based biosensing[109], and bio-imaging[110]. Additionally, the rise of DNA nanotechnology has enabled precise organization of inorganic nanoparticles (NPs), permitting next-generation optoelectronic

and photonic devices to be realized via exploitation of NP emergent behaviors.[111] However, the requirements for QDs conjugated to ssDNA (i.e., ssDNA-QDs) often exceed those of other biological QD conjugates, including the need for stability in solutions of wide pH range and high ionic strength. In particular, conjugation to DNA origami nanostructures can require stability in solutions with 5-20 mM Mg^{2+} concentrations.[112,113] Many applications also demand precise control over the number of ssDNAs conjugated, with some applications necessitating a single ssDNA per particle, whereas in other cases high degrees of multivalency are desired.[114,115] For applications that focus on distance dependent emergent behaviors between QDs or other NPs, such as FRET[116] or fluorescence quenching, all of this must be achieved while minimizing coating thickness. Thus, methods that enable precise control of ssDNA conjugation to compact QDs are needed to realize their full potential in a wide variety of fields ranging from biomedical imaging to photonics.

Because high quality QDs are primarily manufactured in the organic phase, ssDNA modification approaches necessarily require solubilization in aqueous media. Methods to obtain ssDNA-QDs can be divided into three main approaches[117,118]: (i) ssDNA incorporation in the QD crystal lattice during synthesis, (ii) direct attachment of ssDNA to the QD surface, and (iii) covalent attachment of ssDNA to the functional groups of ligands on QD surfaces. However, these methods suffer from several limitations, such as requiring a large excess of expensive ssDNA[119], lack of control over ssDNA density[119], thick surface coatings that limit capability to achieve emergent interactions[120], or loss of colloidal stability[121,122]. For example, the most common approach employed, which is also used in commercial products, consists of QD modification with a thick polymer coating that

intercalates with organic ligands on the QD surface; ssDNA attachment is achieved via low yield carbodiimide chemistry routes.[123] These approaches may maintain QD colloidal and photo-stability, but at the expense of a thick (i.e., > 3 nm increase in radius) coating and low control over ssDNA density.

Several methods have been introduced to address challenges in QD conjugation, many of which rely on the high affinity of cysteine groups for the QD surface.[124,125] Recently, a cysteine-rich peptide, γ-phytochelatin-3 (PC3), was demonstrated to provide a compact coating (i.e., ~0.8-0.9 nm increase in radius) for aqueous QDs.[126] PC3 is applied through exchange with native organic ligands, and presents multiple functional groups (4 -COOH and 1- NH_2 per chain) available for conjugation in its final form. PC3-QDs demonstrate strong stability across a wide pH range (i.e., pH 5-10) and at high ionic strength (i.e., up to 1.5 M NaCl).[126] These properties are enabled by the flat conformation adopted by PC3 molecules, with multiple thiol bonds to the QD surface and preferable orientation of remaining –COOH and $–NH_2$ functional groups outward toward the surrounding media. However, to the best of our knowledge, PC3-QDs have only been employed in streptavidin-biotin conjugation schemes that generate large increases in composite thickness (i.e., ~6 nm increase in radius). Whereas PC3 –COOH and $–NH_2$ groups are readily incorporated into low yield (~ 30%) carbodiimide-based conjugation schemes[123], PC3-QDs lack functional groups required to take advantage of emerging biorthogonal conjugation methods, especially alkyne-azide “click” reactions. Click chemistry approaches provide a reliable means to achieve stoichiometric conjugation as a result of highly selective and efficient cycloaddition under mild conditions.[115]

Here, we combined PC3 passivation methods with copper-free alkyne-azide click chemistry to yield compact QDs conjugated to ssDNAs with precision. As model systems, we employed CdSe/ZnS QDs, most commonly used for biomedical imaging, and poly-thymine (poly-T) ssDNA sequences, which minimize non-specific interactions with ssDNA strands and the QD surface. We also extended this work to mixed base-pair (mbp) sequences. Photophysical properties and ssDNA conjugation efficiency were quantified using absorption and fluorescence spectroscopy. Then, we demonstrated ssDNA functionality using two model systems that require compact QDs as a result of distance dependent behaviors or steric limitations. First, we explored implementation of ssDNA-QDs as energy donors to gold nanoparticles (AuNPs) modified with complementary ssDNA, a system that demands close interactions between both particles and precise ssDNA conjugation to form QD-AuNP dimers. Next, we templated ssDNA-QDs on DNA origami hinge platforms through site-specific self-assembly, a sterically more demanding application. These data demonstrate methods for ssDNA-QD conjugation that result in a compact final product with potential for controllable conjugation yield, providing a possible platform technology for DNA-based QD devices.[113,119]

Materials and Methods

Chemicals

CdSe/ZnS QDs (catalog no. CZ540-10, CZ560-10, CZ600-10) were purchased from NN-Labs, LLC. (Fayetteville, Arizona). Gold nanoparticles (AuNPs) (catalog no. GP01-15-20)

were purchased from NANOCS, LLC. (New York, NY). Phytochelatin-3 (PC3) was custom synthesized and purchased from LifeTein, LLC. (Hillsborough, New Jersey). Azide and thiol modified oligonucleotides (ssDNAs) with optional fluorophore modification for bioconjugation were custom-ordered from Integrated DNA Technologies (Coralville, IA) (see Table 3 for sequences). Sulfo-dibenzocyclooctyne amine (sDBCO) was purchased from Click Chemistry Tools, LLC (Scottsdale, AZ) (catalog no. 1227).

QD Aqueous Transfer

Aqueous QD transfer was conducted using the "loops-trains-tails" approach via modification of the process described by Xu et al.[126] Briefly, manufacturer-supplied QDs in toluene were transferred to chloroform. QDs in toluene (2 µM, 113 µL) were precipitated using methanol (100 µL) and re-dispersed in chloroform (37.5 µL). Then, pyridine (187.5 µL) was added to the freshly solvated QDs (6 µM), followed by chloroform evaporation by heating. This step exchanges some of the native octadecylamine ligands on QD surface with pyridine. As a precaution, QDs were then centrifuged (20817*g*, 1 min) to remove any aggregates. Negligible precipitation was observed. After centrifugation, the supernatant containing suspended QDs (~1 µM, 450 µL in pyridine) was mixed with PC3 (40 mg/mL, 100 µL in DI water), which formed a single-phase solution. Immediately, ligand exchange with PC3 was triggered by increasing solution pH above 10 by addition of tetramethylammonium hydroxide (TMAOH) (25 wt% in MeOH, Millipore Sigma catalog No. 334901), leading to the precipitation of QDs in pyridine. The solution was quickly vortexed and then centrifuged to form a pellet. The pellet was dispersed in DI water and

dialyzed overnight against 1x phosphate buffered saline (PBS) (0.1 M NaH_2PO_4, 0.15 M NaCl, pH 7.2, ThermoFisher Scientific Cat# 28372) using a 20K molecular weight cut-off (MWCO) Slide-A-Lyzer Mini Dialysis Unit (Rockford, IL) to remove excess, unbound PC3. The dialyzed PC3-QD suspension was stored at 4°C until use.

QD Oligonucleotide Conjugation

Aqueous PC3-QDs were conjugated to oligonucleotides via click chemistry in two steps. First, PC3-QDs were conjugated to sDBCO using zero-length cross-linker carbodiimide chemistry. (Note: Carbodiimide chemistry has much higher yields for small molecules, such as the sDBCO molecules employed here, compared to ssDNA molecules most likely because of electrostatic and steric limitations. Also, sDBCO are inexpensive and can therefore be added in large excess.) Briefly, PC3-QDs were exchanged into 2-(N-morpholino)ethanesulfonic acid (MES, ThermoFisher Scientific Cat # 28390) buffer (0.1 M, pH 5) using a 7K MWCO Zeba spin column (Pierce, IL) according to manufacturer's protocol. PC3-QDs (70 µL, 2.5 µM) in MES were mixed with large excess of 1-Ethyl-3-(3-dimethylaminopropyl)carbodiimide (EDC, Thermo Fisher Scientific, catalog No. 77149) and sulfo-N-hydroxysuccinimide (sulfo-NHS, Thermo Fisher Scientific, catalog No. 24525) (EDC:sulfo-NHS:QD = 50,000:50,000:1, final EDC and sulfo-NHS concentration = 100 mM) and incubated for 25 minutes. Next, activated QDs were exchanged into PBS (0.1 M, pH 7.2) using a 40K MWCO Zeba spin column and mixed with sulfo-DBCO (QD: sDBCO = 1: 5000) and vortexed for 4 hours at room temperature. Excess sDBCO was separated from sDBCO-QD conjugates using a 40K MWCO Zeba spin column equilibrated with PBS buffer (0.1 M, pH 7.2).

In the second step, azide-terminated oligonucleotides were conjugated to purified sDBCO-QDs via strain-promoted alkyne-azide cycloaddition click reaction. sDBCO-QDs in PBS (1.5 μM QDs, determined using a Nanodrop 100 spectrophotometer) were mixed with azide-terminated oligonucleotides (QD:ssDNA = 1:30) and allowed to react overnight at 37 °C. Unconjugated oligonucleotides were separated from ssDNA-QD conjugates using 30kDa Amicon centrifugal filters (3 washes with 1x PBS at 7000 rcf, 3 minutes each). QD-DNA conjugates were stored in 1x PBS buffer with 2 wt% dissolved polyethylene glycol 20 kDa (PEG-20k, Millipore Sigma, Cat. # 95172) at 4°C until use.

AuNP Oligonucleotide Conjugation

AuNP quenchers were conjugated to thiol-terminated oligonucleotides using an instantaneous, low pH-assisted conjugation protocol.[127] Thiol-modified oligonucleotides received in stable disulfide forms (100 μM, 50 μL) were first reduced by reaction with 20 μL of freshly-prepared 0.5 M DTT solution in sodium phosphate buffer (0.5 M, pH 8.4) for 1 hour at room temperature. Reduced oligos were purified from DTT using a size exclusion chromatography column (GE NAP-10) according to the manufacturer's protocol. The concentration of reduced oligos was determined by UV-vis spectroscopy by comparing their absorbance at 260 nm (ssDNA peak) with a standard curve. Then, AuNPs were mixed with reduced oligos (AuNP:oligo = 1:225) for 1 minute at room temperature. Next, citrate buffer (500 mM, pH 3) was added to a final citrate buffer concentration of 10 mM and allowed to react for 3 minutes. The solution was then purified from unconjugated, excess

ssDNA and exchanged into 1x PBS buffer using a 100 kDa Amicon centrifugal filter. The ssDNA-AuNP conjugates were stored in 1x PBS at 4°C until use.

QD-DNA-AuNP composite formation

QDs and AuNPs presenting complementary ssDNA (Table 3) were mixed in desired ratios in PBS with 2 wt% PEG-20k at a fixed QD concentration of 3 nM and allowed to self-assemble overnight at 4°C. For control experiments, QDs and AuNPs presenting non-complementary ssDNA were mixed following the same method. Both the samples were prepared using green QDs (i.e., CZ540) and 15 nm AuNPs at QD:AuNP molar ratios of 2:1, a final QD concentration of 3 nM, and a PEG concentration of 2% w/v in physiological 0.1 M phosphate buffer saline (PBS) at pH 7. Samples were stored overnight before fluorescence measurement.

Table 3 QD and AuNP DNA Sequences Employed

NP	ssDNA	5’	Sequence	3’
QD	T_{16}	Azide (N_3)	TT TTT TTT TTT TTT TT	
QD	T_{16}-Cy5	Azide (N_3)	TT TTT TTT TTT TTT TT	Cy5Sp
QD	12mbp-Cy5	Azide (N_3)	GT GCA TGT AAC G	Cy5Sp
QD	T_{10}	Azide (N_3)	TT TTT TTT TT	Cy5Sp
AuNP	A_{20}	C6-thiol	AA AAA AAA AAA AAA AAA AAA	
AuNP	T_{14}	C6-thiol	TT TTT TTT TTT TTT	

QD-DNA origami conjugation

Briefly, DNA origami hinges were assembled in a solution of 20 nM m13mp18 bacteriophage scaffold DNA, 200 nM of each staple strand, 1 mM EDTA (Ethylenediaminetetraacetic acid), 5 mM NaCl (Sodium Chloride), 5 mM Tris (tris(hydroxymethyl)aminomethane), and 18 mM $MgCl_2$ (Magnesium chloride) as

previously described.[128] ssDNA-QDs dissolved in 12.5 mM $MgCl_2$ were mixed with DNA origami hinges presenting complementary ssDNA on both arms at QD:Hinge ratios of 5:1 and incubating at 55°C for 10 minutes before cooling to room temperature. QD-DNA origami hinge conjugates were purified by gel electrophoresis (i.e., 2% agarose, 0.5X (Tris, Boric acid, Ethylenediaminetetraacetic acid (EDTA), TBE), 11 mM $MgCl_2$) before transmission electron microscopy (TEM) imaging.

Absorbance

Absorbance measurements were used to confirm conjugation and determine NP concentrations. Absorption spectra were collected using a Genesys 6 UV-Visible or Nanodrop 1000 spectrophotometer.

Fluorescence

Fluorescence analysis using a PTI QuantaMaster fluorometer was performed to calculate quantum yields (QY), monitor QD bioconjugation to dye-labeled molecules, and analyze fluorescence quenching between QDs and AuNPs. Quantum yield was calculated using the equation described in Ref. 129:

$$\Phi_{QD} = \Phi_{st} \times \frac{F_{QD}}{F_{st}} \times \frac{f_{st}(\lambda_{ex})}{f_{QD}(\lambda_{ex})} \times \frac{\eta_{QD}^2}{\eta_{st}^2} \quad \text{Equation 5.1}$$

where, Φ_x, F_x, $f_x(\lambda_{ex})$ and η_x are the quantum yield, spectrally-integrated fluorescence flux, absorption factor, and refractive index of the medium, respectively, and subscripts QS and St refer to the QD sample and a standard (Rhodamine 6G, ThermoFisher Scientific, Cat. No.252433), respectively.

For experiments optimizing conjugation, NH_2-terminated dye molecules were employed and successful conjugation was monitored by measuring the fluorescence spectra of samples after purification. The presence of both QD and dye fluorescence peaks indicated successful conjugate formation. Efficiency of ssDNA conjugation was monitored by employing dye-labeled ssDNA, such that the oligonucleotide sequence was sandwiched between the -NH_2 group and the dye molecule (i.e., NH_2-ssDNA-dye). Presence of both QD and dye fluorescence peaks in purified samples indicated successful reaction. For determining number of ssDNA conjugated per QD, dye-tagged ssDNA was also used. The intensity of QD and dye-ssDNA fluorescence peaks were compared to their respective standard curves to calculate the ratio of ssDNA per QD. All measurements were conducted at concentrations that provided measurable signal for both QDs as well as conjugated ssDNA-dye molecules (~150 nM).

Fluorescence quenching between QD and AuNP pairs was analyzed by comparing the fluorescence of hybridized QD-AuNP complexes (complementary sequence) with the fluorescence of unhybridized QD/AuNP solutions (non-complementary sequence) at the same concentration in 2 wt. % PEG-20K at QD:AuNP ratio of 2:1 and at 3 nM ssDNA-QD. PEG-20K molecules were included to enable depletion stabilization of complexes.

Transmission electron microscopy (TEM)

QDs, AuNPs, and corresponding conjugates were imaged using an FEI Tecnai G2 Bio Twin TEM. Aqueous samples were deposited on ultrathin carbon coated copper grids, 300

mesh (Ted Pella, Redding, CA). For imaging QD-DNA origami conjugates, TEM grids were negatively stained with 2% uranyl formate as previously described.[130]

Gel electrophoresis

Gel electrophoresis was performed to validate ssDNA conjugation and to determine its efficiency using Cy5 dye-tagged ssDNA. During gel electrophoresis, unpurified ssDNA-QD samples (100 µM, 15 µL), ssDNA, and PC3-QDs were analyzed using a 2 wt% agarose gel prepared in TE buffer at 110 V for 45 minutes. After completion, QD and dye-tagged ssDNA fluorescence was assessed using an Imager-Typhoon Trio (GE Healthcare) scanner with the Cy2-FRET and Cy5 excitation settings, respectively. Gel images were analyzed using NIH ImageJ to determine QD and ssDNA locations in the gel. The gel analysis feature of ImageJ was used to measure the ratio of fluorescence from conjugated versus unconjugated ssDNA to calculate the conjugation efficiency (conj%). The amount of ssDNA per QD was then calculated by:

$$\frac{ssDNA}{QD} = conj\% \times \left(\frac{ssDNA\ added}{QD\ added}\right) \quad \text{Equation 5.2}$$

Results and Discussion

Photophysical properties and yield of PC3-QDs following aqueous phase transfer

The highest quality QDs are manufactured in the organic phase; thus, they must first be transferred into the aqueous phase prior to ssDNA conjugation. Here, PC3 ligands were used to solubilize QDs because they exhibit numerous sulfur groups that form strong multidentate linkages to the QD surface and outward-facing -COOH and $–NH_2$ functional

groups that increase the colloidal stability through electrostatic repulsion and provide sites for ssDNA attachment.[126] Successful PC3 coating and QD phase transfer was performed using a modified version of the method described by Xu et al.[126] in which QDs were not precipitated before dissolution in pyridine, reducing QDs losses resulting from this step (see Appendix D). With this modified approach, nearly 100% phase-transfer yield was observed.

In contrast to prior reports[126], PC3-QDs exhibited a small red-shift in peak emission wavelength (λ_{em}) (~ few nm) after the transfer process (Figure 15, Table 4), which was more pronounced for smaller QDs than larger ones (i.e., $\lambda_{540} > \lambda_{560} > \lambda_{600}$). Size-dependent differences most likely reflect the reduced stability of smaller QDs, which have greater surface to volume ratio. Differences with respect to prior reports likely result from the native surface ligands employed: octadecylamine (ODA) in the current study versus trioctylphosphine oxide (TOPO).[126] Primary amine ligands, such as ODA, exert compressive stress on the QD lattice in contrast to TOPO, which exerts a tensile stress.[131] The compressive stress of ODA is also responsible for the high QY of ODA-coated QDs. As a result, ligand exchange of ODA with PC3 may be accompanied by stretching of the QD lattice, effectively increasing the size of PC3-QDs and yielding a red-shift in emission wavelength. As is typical of aqueous phase transfer processes, QY was also reduced from that observed for organic QDs (Table 4) and was slightly lower than that reported for TOPO-capped QDs transferred via PC3 (i.e., 47%), most likely as a result of released lattice strain.

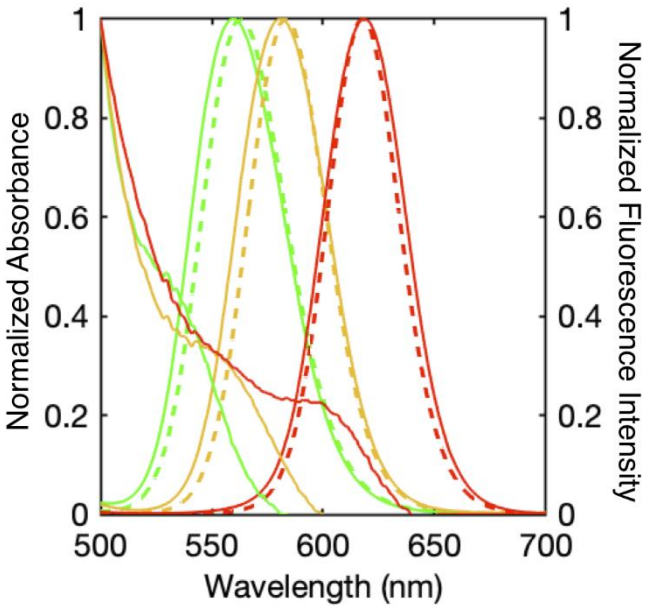

Figure 15 Absorbance and fluorescence spectra of QDs (green: λ_{em} = 540 nm, orange: λ_{em} = 560 nm, and red: λ_{em} = 600 nm) before (solid) and after (--) transfer to aqueous phase via PC3 ligand exchange. Note: Absorbance is only provided for samples prior to PC3 exchange because of PC3 signal interference.

Table 4 Photophysical properties of QDs before and after aqueous transfer

Color	λ_{ex} (nm)	λ_{em}(organic) (nm)	QY% (organic)	λ_{em}(aqueous) (nm)	QY% (aqueous)
Green	540	559	78	563	17
Orange	560	581	70	583	20
Red	600	618	69	617	32

ssDNA Conjugation to PC3-QDs using Click Chemistry

Initially, we attempted to conjugate ssDNA molecules to PC3-QDs using carbodiimide chemistry as described previously for streptavidin conjugation[126]; however, we were unsuccessful (Figure 33, and Table 6). Thus, we adopted a click chemistry approach. However, PC3-QDs inherently lack alkyne or azide groups necessary for this reaction. PC3-QDs display two functionalities, $-NH_2$ and -COOH groups, that could be used to add "click"-able groups via homo-bifunctional NHS-ester or carbodiimide zero-length crosslinker chemistries, respectively.[132] However, the wide availability of azide-terminated oligonucleotides and greater number of -COOH groups on PC3-QDs strongly favors their use for alkyne modification.

Thus, PC3 –COOH groups were first modified with sDBCO using carbodiimide chemistry (Figure 16), which is much more efficient for small molecules than the ssDNAs previously attempted. QD colloidal stability was enhanced by use of sDBCO instead of DBCO, and PEG -20k enabled depletion stabilization (Figure 34). This approach overcomes limitations of carbodiimide conjugation processes by enabling rigid and selective conjugation pathways in the latter part of the nested conjugation. Bio-orthogonal chemistry, specifically, click chemistry, proceeds via an alkyne-azide cycloaddition reaction that has been demonstrated to be highly reproducible and efficient under mild reaction conditions.[115] Further, unlike the carbodiimide chemistry, click chemistry enables specific reaction between alkyne-azide groups without side-reactions, such as hydrolysis seen in carbodiimide alternatives.[133]

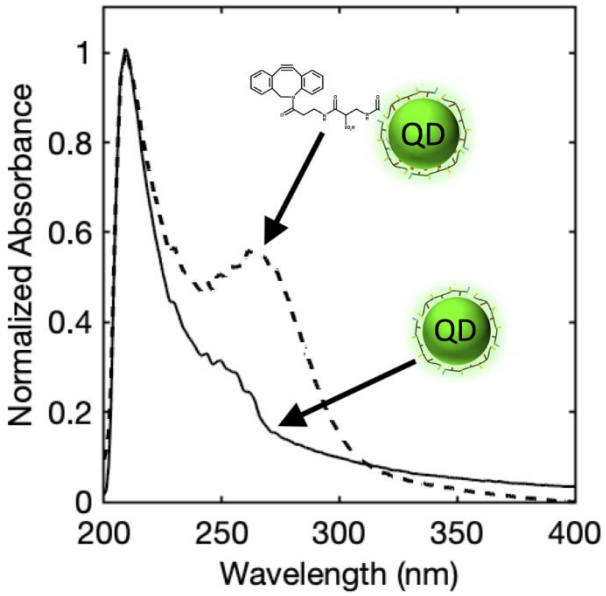

Figure 16 Absorbance spectra of PC3-QDs (solid) and sDBCO-PC3-QDs (--) formed via carbodiimide chemistry. sDBCO peak = ~260 nm.

To generate ssDNA-QD conjugates, sDBCO-QDs were reacted with N_3-terminated ssDNA. Reaction progress was monitored using ssDNAs modified with both N_3 and Cy5 fluorophores (Table 3). Fluorescence peaks for both QDs and Cy5 dye were observed in purified conjugates, indicating successful reaction (Figure 17a), which was further confirmed by gel electrophoresis (Figure 17b, c) (Note: The mobility difference of free Cy5-ssDNA in ssDNA and ssDNA-QD (U) lanes likely results from differences in buffer conditions during gel electrophoresis, as has previously been observed for ssDNA strands[134]). Fluorescence and gel electrophoresis analysis indicated a density of ~0.5 ssDNA per QD using this approach; thus, some QDs were devoid of ssDNA. This may result from inconsistencies inherent in the "shotgun" carbodiimide chemistry employed in sDBCO attachment. With a target of ~ 1 ssDNA per QD desired to achieve dimerization

with AuNPs and avoid uncontrolled assembly, this was a satisfactory result. This procedure was used to reproducibly conjugate ssDNA to QDs of different sizes (i.e., λ_{540} or λ_{600}) and with ssDNAs of different lengths (i.e., 10, 12, 16 bp) and sequences (i.e., mbp or poly-T), indicating its robustness (Figure 35, Figure 36).

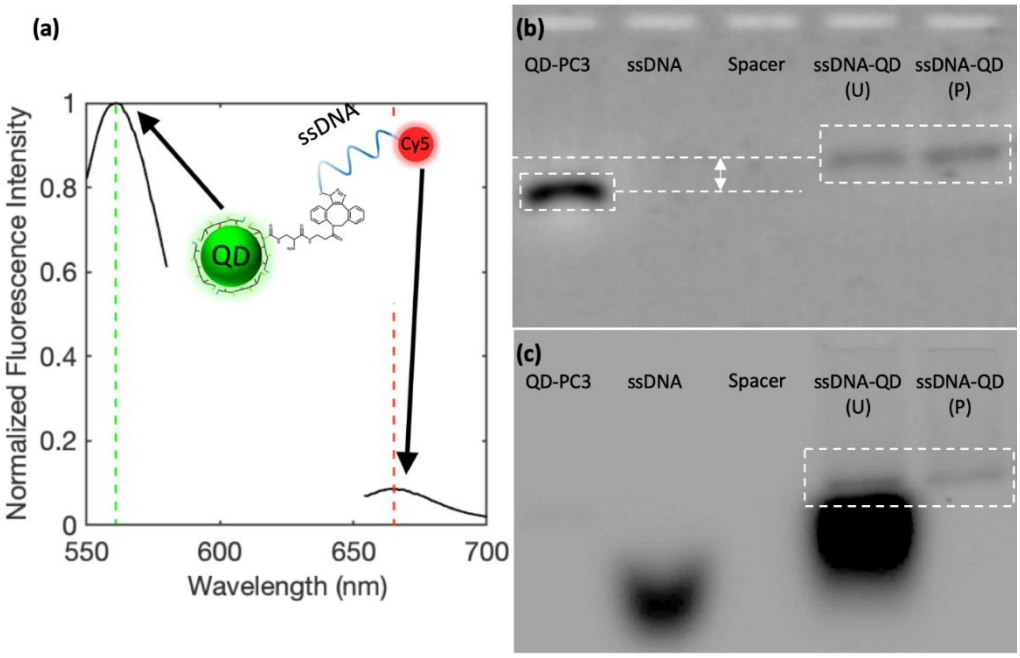

Figure 17 (a) Fluorescence spectra of ssDNA-QDs formed via click chemistry. ssDNA is functionalized with a Cy5 fluorophore for detection. (QDs: λ_{ex} = 350 nm, λ_{em} = 561 nm; Cy5-ssDNA: λ_{ex} = 649 nm, λ_{em} = 664 nm). Electrophoretic characterization of ssDNA-QD conjugates imaging using the (b) QD excitation wavelength (i.e., Cy2-Cy3-FRET setting on typhoon scanner) and (c) Cy5-ssDNA excitation wavelength (i.e., Cy5 setting on typhoon scanner). The large dashed boxes in (b) and (c) indicate the same gel location. U = Unpurified ssDNA-QD conjugates, P = Centrifugal filter purified ssDNA-QD conjugates. (Note: A spacer lane was introduced to avoid overlap of ssDNA signal from the free ssDNA, lane 2, and unpurified ssDNA-QDs, lane 4.)

ssDNA-QDs as Fluorescence Donors

To evaluate the effectiveness of ssDNA-QDs, we next evaluated them in a fluorescence quenching application. In close-proximity to AuNPs, near-field effects emerge that modify QD fluorescence through static or dynamic charge or energy transfer[135], FRET[136], surface field enhancement[137], or nanometal surface energy transfer (NSET)[111,116]. Near-field effects are extremely sensitive to interparticle spacing and decay as a function of $1/s^n$ ($n \geq 1$). DNA offers tremendous potential to finely, reversibly, and reproducibly tune QD devices for these applications. Further, unlike many coatings used for QD aqueous solubilization[120,138], the compact nature of the PC3 coating enables QDs to interface more intimately with the surrounding environment (i.e., within ~1 nm) while maintaining stability in physiological and high-salt conditions.

Generally, changes in colloidal QD fluorescence in the presence of AuNPs can be broadly divided in two categories: (i) those arising from the inner-filter effect (IFE) and (ii) those arising from near-field effects.[135] The IFE is an apparent decrease in fluorescence intensity resulting from attenuation of the excitation or emission beam at high concentration or in the presence of a highly absorbing material (e.g., AuNPs). Thus, the IFE effect results in a decrease in fluorescence intensity that is not a true quenching response and is not indicative of formation of DNA-hybridized NP pairs. The IFE can be empirically eliminated by decreasing sample OD < 0.05[139]; however, this was not possible here because decreasing the OD of the sample containing AuNPs < 0.05 resulted in QD fluorescence below the spectrophotometer detection limit. Alternatively, steady-state QD fluorescence can be monitored in the presence of AuNPs initially and as complexes form[111,116]. ssDNA-QDs

(T_{16}-QD) were incubated with non-complementary ssDNA-AuNPs (T_{14}-AuNPs), which should not form hybridized pairs (NC), and complementary ssDNA-AuNPs (A_{20}-AuNPs) (C). Their fluorescence was compared (Figure 18), and the % decline of the entire sample was calculated as:

$$\% \, PL_{Quench} = 1 - \frac{F_{AuNP-c}}{F_{AuNP-nc}} \qquad \text{Equation 5.3}$$

where F_{AuNP-c} and $F_{AuNP-nc}$ are the steady-state peak fluorescence intensity of hybridized QD-AuNP composites and the non-complementary ssDNA- QD and -AuNP mixture, respectively.

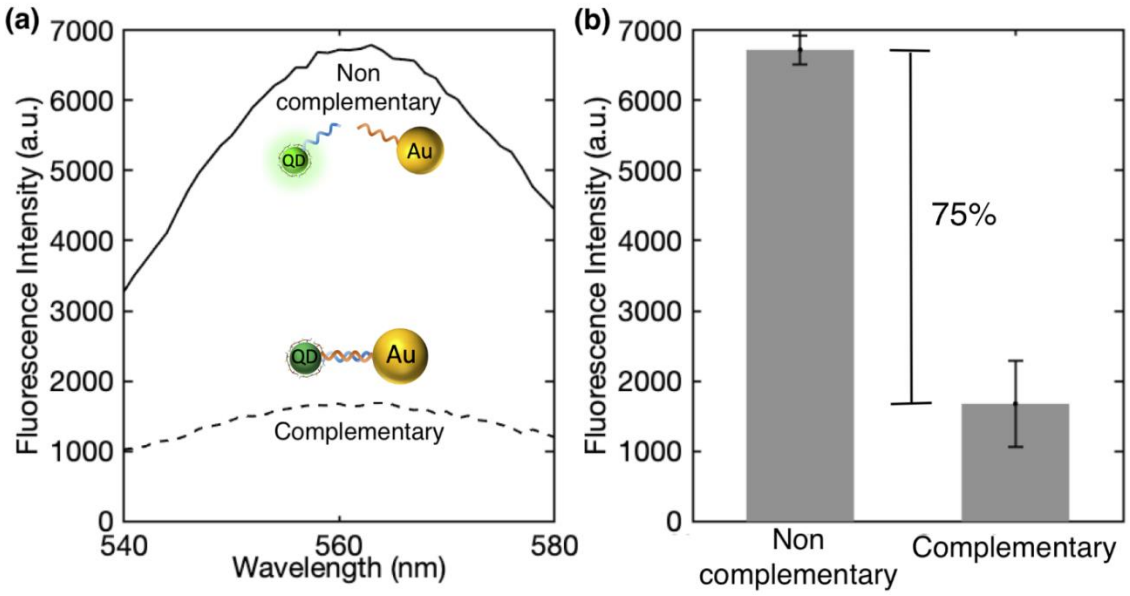

Figure 18 (a) Fluorescence spectra of samples containing non-complementary ssDNA-QDs and ssDNA-AuNPs (solid) and complementary ssDNA-QD and ssDNA-AuNP conjugates forming QD-DNA-AuNP composites, (b) Bar-plot of the non-complementary and complementary fluorescence peak intensities (560 nm) for N = 3 samples.

A ~75% decline in fluorescence was observed for hybridized complementary samples compared to mixtures of QDs and AuNPs presenting non-complimentary ssDNA (Figure 18). However, this observation alone does not necessarily correlate to the quenching per hybridized NP pair, as the solution likely consists of a mixture of free and modified QDs based on fluorescence and electrophoresis results of ssDNA/QD. Given these factors, the change in QD fluorescence attributable to hybridization with AuNPs (S) can be represented as follows[135]:

$$F_c = \chi_{AuNP} \cdot F_{nc} \cdot S + (1 - \chi_{AuNP}) F_{nc} \quad \text{Equation 5.4}$$

$$S = \frac{F_c - (1-\chi_{AuNP})F_{nc}}{\chi_{AuNP} \cdot F_{nc}}$$ Equation 5.5

where F_c and F_{nc} are the measured fluorescence of samples incubated with C and NC AuNPs, respectively, and χ_{AuNP} is the fraction of AuNP-hybridized QDs.

The latter was determined experimentally by centrifuging C and NC solutions and measuring supernatant fluorescence after removing the large, high-density AuNPs and their conjugates. χ_{AuNP} is then equal to: $\frac{F_{nc}^{super} - F_c^{super}}{F_{nc}^{super}}$. The first term of Equation 5.4 denotes the contribution of hybridized composites to the fluorescence signal, whereas the second term denotes the contribution of free, non-hybridized QDs. Based on this analysis (Table 5), ~84% of the QDs in the solution formed hybridized AuNP-QD pairs, resulting in a near-field effect of 0.11 and an effective quenching of ~ 89.3% per QD, calculated as: $100(1 - S)$.

Table 5 FRET in QD-DNA-AuNP composites

Sample	% F_{loss}, Bulk	% hybridized	S	% F_{loss}, S
QD-16(AT)DNA-AuNP	75.0	0.84	0.11	89.3

F = fluorescence, S = near field effect in AuNP-hybridized QDs, % F_{loss}, Bulk is percent loss in fluorescence of the entire sample consisting of AuNP-hybridized and free QDs, % F_{loss}, S is the percent of fluorescence loss resulting from near field effects in AuNP-hybridized QDs.

This analysis suggest that near field effects are the dominant cause of fluorescence loss in C solutions. Further, these results most likely originate from energy transfer between NPs. It has been previously demonstrated that static or dynamic charge or energy transfer,

surface field enhancement, and NSET are negligible at low concentrations[135], for AuNPs ≤ 30 nm in diameter[140], and for small polarizability differences for fluorophore-quencher pairs4, respectively. Thus, the most likely explanation for reduced fluorescence intensity via near field mechanisms is enhanced fluorescence quenching resulting from the significant spectral overlap between the emission of green QDs and AuNP absorbance and the reduced separation distance achieved by DNA hybridization[141]. At the QD:AuNP ratio (2:1) employed, quenching efficiency was significantly greater than that reported in studies using organic dye quenchers (i.e., < 30% at donor:acceptor ratios of 1:1) because of the high absorption cross-section of AuNPs.[84,142] Comparable quenching efficiencies can still be achieved using organic quenchers by placing them very close to the QD surface[143]; however, such systems suffer from poor performance because of photobleaching. Further, the quenching efficiency observed here was also greater than that reported for many previous QD-AuNP systems[144], most likely as a result of reduced inter-NP spacing enabled by DNA hybridization versus the use of large biomolecules (i.e., proteases) or because of low spectral overlap in those systems. Further, the current system displayed comparable or even slightly higher quenching efficiency than QD-ssDNA-AuNP systems with similar spectral overlap, despite increased ssDNA chain length (i.e., 16 base pairs (bp) in the current system versus 7-10 bp in prior reports[116,145]). This difference can be attributed to the thinner coating provided by PC3 on the QD surface that reduces inter-NP spacing.

Nevertheless, quenching efficiency was lower than theoretical; ~99% efficiency would be expected for the QDs and AuNPs used in this system (i.e., See Appendix D calculations for details: absorbance spectral overlap = 1.34×10^{19} $M^{-1}cm^{-1}nm^4$, interparticle

spacing(s) = 6.7 nm (calculated based on DNA chain length), Förster radius (R_o) = 16.6 nm). This may be explained by quenching efficiency dependence on donor valency (n), i.e., number of donors per quencher[146]:

$$S_{FRET} = \frac{nR_o^6}{nR_o^6+s^6}$$ Equation 5.6

where S_{FRET} and R_o are the quenching efficiency and Förster radius, respectively.

The current system presents variable valency (i.e., some QDs do not contain ssDNA) because of differences in ssDNA number per QD. Although most QDs formed hybridized pairs with AuNPs, which were in excess, 16% failed to do so. Improved control over ssDNA conjugation through further optimization of click-based approaches would improve these results. Similarly, the centrifugal filtration purification approach employed here only separates free ssDNA from conjugates, not unmodified QDs, which we confirm to be present in solution based on fluorescence and electrophoresis results. Thus, these results could be improved by alternative separation schemes that enhance purification. Nonetheless, these data show that compact coating methods, such as those provided by PC3, combined with click chemistry-enabled ssDNA modification provide a robust approach for QD energy transfer materials.

ssDNA-QD attachment and templating on DNA origami materials

Next, we examined the ability of ssDNA QDs to be integrated with DNA origami materials. DNA origami can serve as a scaffold to precisely assemble NPs into complex 3D arrangements for potential applications in energy and photonics.[147] However, most DNA

origami studies using NPs have been limited to AuNPs[147], most likely because of their ease of ssDNA modification and stability at high ionic strength conditions (i.e., 5-20 mM divalent Mg) required to stabilize origamis.[112] Few reports demonstrate QD attachment to DNA origami[119,148], despite their obvious potential in opto-electrical devices. Some of these studies employ thick streptavidin coatings for composite formation that strongly limit distance-dependent emergent interactions between NPs and fail to provide the highly-specific programmability achievable via DNA hybridization[148]. Thus, as a second model system, we evaluated ability of compact ssDNA-QDs to hybridize with sterically complex DNA origami platforms.

In these experiments, ssDNA-QDs were incubated with DNA origami hinges[128] that have previously been used for AuNP templating[149] with binding sites (complementary overhangs) on the top and bottom arms (Figure 19a). QDs integrated with these platforms, as indicated by their position between hinge vertex arms in TEM images (Figure 19b). In most cases, QD binding resulted in hinges changing to a closed configuration, indicating a single QD is bound to both hinge arms. Although in some cases, QDs were bound to only one hinge arm. This may result from only 1 ssDNA/QD, which would enable only one complementary DNA pair to form. These data are similar to reports using the DNA embedding approach for QD templating on DNA origami platforms[111,119]; however, our method does not require a large excess of ssDNA for successful conjugation because of the specificity of click chemistry reactions. Combined with compact PC3 coatings that augment NP emergent interactions through reduced separation distances, this approach

may provide a more feasible, less expensive route to macroscale materials with energy applications.

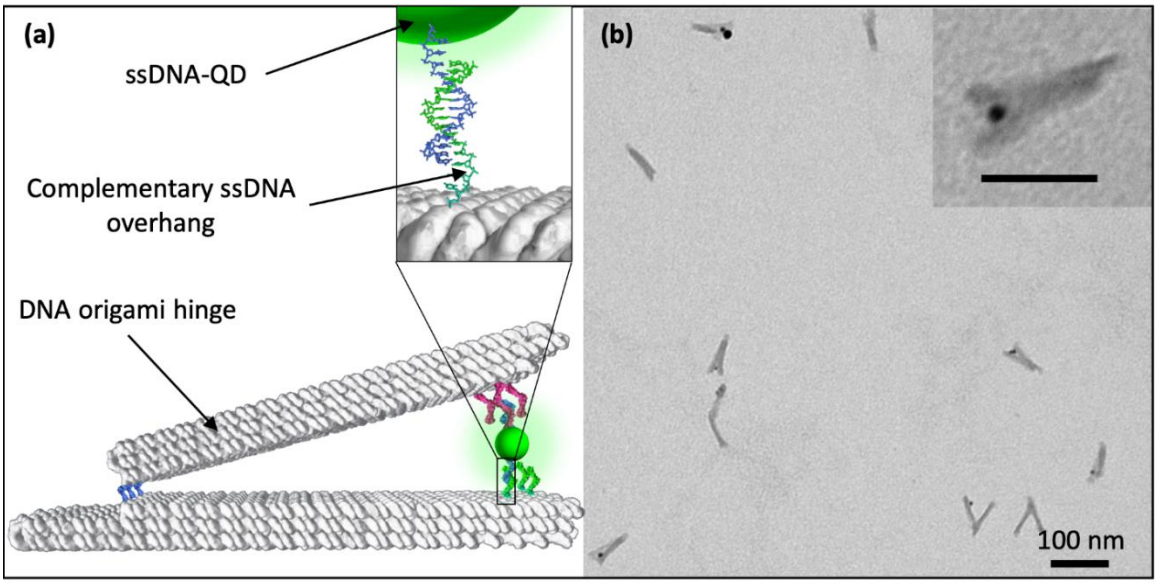

Figure 19 (a) Schematic of DNA origami hinges indicating locations of ssDNA overhangs on the top and bottom hinge arms for complementary ssDNA-QD binding. (b) TEM image of ssDNA-QD-DNA origami composites formed via hybridization with complementary ssDNA overhangs at distal locations on the top and bottom hinge arms (Inset scale: 100 nm).

Conclusions

Here, we present a novel method for conjugation of ssDNA to QDs that combines a compact, multivalent coating methodology with mild, strain-promoted alkyne-azide cycloaddition click reactions to yield stable conjugates at high yield. This approach enhances potential for emergent interactions between QDs by reducing the thickness of coatings required to transfer QDs to the aqueous phase, while minimizing loss of

fluorescence and colloidal stability. Additionally, this method provides an alternative to popular carbodiimide chemistry approaches that are inefficient and non-specific, particularly when large, monovalent, charged molecules (e.g., ssDNA) are employed. Successful conjugation was confirmed by evaluating ssDNA hybridization in two platforms: fluorescence quenching with AuNP conjugates and conjugation to DNA origami materials. The resulting compact ssDNA-QDs hybridized with complementary ssDNA-AuNPs (2:1 QD:AuNP ratio) resulting in 84% hybridized pairs and a quenching efficiency of 89% per hybridized pair. Further, enhanced colloidal stability of ssDNA-QDs enabled ready incorporation with DNA origami templating platforms despite the requirement of high ionic strength buffers to stabilize these systems. Improved control of conjugation reactions and subsequent separation steps would enhance these methods, enabling modification with specified numbers of DNA strands for highly controlled reaction. These results demonstrate ssDNA-PC3-QDs generated using click chemistry approaches as strong candidates for applications that leverage emergent NP interactions, such as FRET and optoelectronic devices.

References

107. Dehankar, A., Porter, T., Johnson, J. A., Castro, C. E. & Winter, J. O. Compact quantum dot surface modification to enable emergent behaviors in quantum dot-DNA composites. *J. Chem. Phys.* **151**, (2019).
108. Zhang, Y. & Wang, T. H. Quantum dot enabled molecular sensing and diagnostics. *Theranostics* **2**, 631–654 (2012).
109. Shi, J., Tian, F., Lyu, J. & Yang, M. Nanoparticle based fluorescence resonance energy transfer (FRET) for biosensing applications. *Journal of Materials Chemistry B* **3**, 6989–7005 (2015).
110. Petryayeva, E., Algar, W. R. & Medintz, I. L. Quantum dots in bioanalysis: a review of applications across various platforms for fluorescence spectroscopy and imaging. *Appl. Spectrosc.* **67**, 215–52 (2013).

111. Samanta, A., Zhou, Y., Zou, S., Yan, H. & Liu, Y. Fluorescence quenching of quantum dots by gold nanoparticles: A potential long range spectroscopic ruler. *Nano Lett.* **14**, 5052–5057 (2014).
112. Ponnuswamy, N. *et al.* Oligolysine-based coating protects DNA nanostructures from low-salt denaturation and nuclease degradation. *Nat. Commun.* **8**, 1–9 (2017).
113. Bui, H. *et al.* Programmable periodicity of quantum dot arrays with DNA origami nanotubes. *Nano Lett.* **10**, 3367–3372 (2010).
114. Wang, G., Li, Z. & Ma, N. Next-Generation DNA-Functionalized Quantum Dots as Biological Sensors. *ACS Chemical Biology* **13**, 1705–1713 (2018).
115. Algar, W. R. *et al.* The controlled display of biomolecules on nanoparticles: A challenge suited to bioorthogonal chemistry. *Bioconjugate Chemistry* **22**, 825–858 (2011).
116. Li, M. *et al.* Size-Dependent Energy Transfer between CdSe/ZnS Quantum Dots and Gold Nanoparticles. *J. Phys. Chem. Lett.* **2**, 2125–2129 (2011).
117. Samanta, A., Deng, Z., Liu, Y. & Yan, H. A perspective on functionalizing colloidal quantum dots with DNA. *Nano Research* **6**, 853–870 (2013).
118. Blanco-Canosa, J. B. *et al.* Recent progress in the bioconjugation of quantum dots. *Coordination Chemistry Reviews* **263**–**264**, 101–137 (2014).
119. Deng, Z., Samanta, A., Nangreave, J., Yan, H. & Liu, Y. Robust DNA-functionalized core/shell quantum dots with fluorescent emission spanning from UV-vis to near-IR and compatible with DNA-directed self-assembly. *J. Am. Chem. Soc.* **134**, 17424–17427 (2012).
120. Parak, W. J. *et al.* Cell Motility and Metastatic Potential Studies Based on Quantum Dot Imaging of Phagokinetic Tracks. *Adv. Mater.* **14**, 882–885 (2002).
121. Sun, D. & Gang, O. DNA-functionalized quantum dots: Fabrication, structural, and physicochemical properties. *Langmuir* **29**, 7038–7046 (2013).
122. Medintz, I. L. *et al.* A reactive peptidic linker for self-assembling hybrid quantum dot-DNA bioconjugates. *Nano Lett.* **7**, 1741–1748 (2007).
123. Banerjee, A., Pons, T., Lequeux, N. & Dubertret, B. Quantum dots-DNA bioconjugates: Synthesis to applications. *Interface Focus* **6**, 20160064 (2016).
124. Pinaud, F., King, D., Moore, H. P. & Weiss, S. Bioactivation and Cell Targeting of Semiconductor CdSe/ZnS Nanocrystals with Phytochelatin-Related Peptides. *J. Am. Chem. Soc.* **126**, 6115–6123 (2004).
125. Wang, W. *et al.* Multifunctional and High Affinity Polymer Ligand that Provides Bio-Orthogonal Coating of Quantum Dots. *Bioconjug. Chem.* **27**, 2024–2036 (2016).
126. Xu, J., Ruchala, P., Ebenstain, Y., Li, J. J. & Weiss, S. Stable, Compact, Bright Biofunctional Quantum Dots with Improved Peptide Coating. *J. Phys. Chem. B* **116**, 11370–11378 (2012).
127. Zhang, X., Servos, M. R. & Liu, J. Instantaneous and quantitative functionalization of gold nanoparticles with thiolated DNA using a pH-assisted and surfactant-free route. *J. Am. Chem. Soc.* **134**, 7266–7269 (2012).
128. Marras, A. E., Zhou, L., Su, H. J. & Castro, C. E. Programmable motion of DNA origami mechanisms. *Proc. Natl. Acad. Sci. U. S. A.* **112**, 713–718 (2015).

129. Grabolle, M. *et al.* Determination of the fluorescence quantum yield of quantum dots: Suitable procedures and achievable uncertainties. *Anal. Chem.* **81**, 6285–6294 (2009).
130. Castro, C. E. *et al.* A primer to scaffolded DNA origami. *Nat. Methods* **8**, 221–229 (2011).
131. Green, M. The nature of quantum dot capping ligands. *Journal of Materials Chemistry* **20**, 5797–5809 (2010).
132. Hermanson, G. T. *Bioconjugate Techniques*. *Bioconjugate Techniques* (Elsevier Inc., 2008). doi:10.1016/B978-0-12-370501-3.X0001-X
133. Thorek, D. L. J., Elias, ew R. & Tsourkas, A. Comparative Analysis of Nanoparticle-Antibody Conjugations: Carbodiimide Versus Click Chemistry. *Mol. Imaging* **8**, 7290.2009.00021 (2009).
134. Martin, T. G. & Dietz, H. Magnesium-free self-assembly of multi-layer DNA objects. *Nat. Commun.* **3**, 1–6 (2012).
135. Zhang, D. & Nettles, C. B. A Generalized Model on the Effects of Nanoparticles on Fluorophore Fluorescence in Solution. *J. Phys. Chem. C* **119**, 7941–7948 (2015).
136. Zhang, X. *et al.* Experimental and theoretical investigation of the distance dependence of localized surface plasmon coupled förster resonance energy transfer. *ACS Nano* **8**, 1273–1283 (2014).
137. Song, J. H., Atay, T., Shi, S., Urabe, H. & Nurmikko, A. V. Large enhancement of fluorescence efficiency from CdSe/ZnS quantum dots induced by resonant coupling to spatially controlled surface plasmons. *Nano Lett.* **5**, 1557–1561 (2005).
138. Algar, W. R. & Krull, U. J. Adsorption and hybridization of oligonucleotides on mercaptoacetic acid-capped CdSe/ZnS quantum dots and quantum dot-oligonucleotide conjugates. *Langmuir* **22**, 11346–11352 (2006).
139. Kubista, M., Sjöback, R., Eriksson, S. & Albinsson, B. Experimental correction for the inner-filter effect in fluorescence spectra. *Analyst* **119**, 417–419 (1994).
140. Härtling, T., Reichenbach, P. & Eng, L. M. Near-field coupling of a single fluorescent molecule and a spherical gold nanoparticle. *Opt. Express* **15**, 12806 (2007).
141. Albani, J. R. *Principles and Applications of Fluorescence Spectroscopy*. *Principles and Applications of Fluorescence Spectroscopy* (Blackwell Publishing Ltd, 2007). doi:10.1002/9780470692059
142. Zhang, C. Y. & Johnson, L. W. Quantum dot-based fluorescence resonance energy transfer with improved FRET efficiency in capillary flows. *Anal. Chem.* **78**, 5532–5537 (2006).
143. Zhou, D. *et al.* Fluorescence resonance energy transfer between a quantum dot donor and a dye acceptor attached to DNA. *Chem. Commun.* 4807–4809 (2005). doi:10.1039/b508911e
144. Kim, Y. P. *et al.* Energy transfer-based multiplexed assay of proteases by using gold nanoparticle and quantum dot conjugates on a surface. *Anal. Chem.* **80**, 4634–4641 (2008).
145. Gueroui, Z. & Libchaber, A. Single-molecule measurements of gold-quenched

quantum dots. *Phys. Rev. Lett.* **93**, 166108 (2004).
146. Chou, K. F. & Dennis, A. M. Förster resonance energy transfer between quantum dot donors and quantum dot acceptors. *Sensors (Switzerland)* **15**, 13288–13325 (2015).
147. Daksh, D., Rawtani, D. & Agrawal, Y. K. Recent developments in bio-nanoelectronics devices: A review. *Journal of Bionanoscience* **10**, 81–93 (2016).
148. Du, K. *et al.* Quantum dot-DNA origami binding: A single particle, 3D, real-time tracking study. *Chem. Commun.* **49**, 907–909 (2013).
149. Fan, Q., Nabar, G., Miller, C., Castro, C. & Winter, J. Photo-switchable quantum dots based on reversible FRET. *Proc. SPIE* **8954**, (2014).

Chapter 6. Conclusions and Future Directions

Conclusions

Overall, these studies identified and addressed several major considerations that must be made when developing QDs for biosensing applications, covering alternative nontoxic materials for QD synthesis, the effect of preparation steps on fluorescence properties, a QD-based sensing and manipulation platform, and a novel bioconjugation strategy for QD-ssDNA conjugates. In the toxicity studies of Chapter 2, the toxicity of Mn-doped ZnSe QDs water solubilized via ligand exchange or micelle encapsulation was compared to the toxicity of CdSe/ZnS QDs water solubilized via the same methods in liver cancer cells. Overall, both samples of Mn-doped ZnSe QDs, as well as the micelle encapsulated CdSe/ZnS QDs were found to be non-toxic. This study demonstrated that micelle encapsulation may be a better alternative to ligand exchange for studies where toxicity may be of concern, and also demonstrated the promise of Mn-doped ZnSe QDs for biological applications.

In Chapter 3, the effects of common steps employed during QD bioconjugation on QD quantum yield were investigated. Centrifugal filtration and buffer exchange with a low pH buffer commonly used in bioconjugation protocols were the two steps that resulted in the most significant QD stability issues (either colloidal stability or photostability) for QDs from multiple vendors. This study indicates that QD supplier conditions and processing procedures need to be carefully considered when designing experiments with biological

labeling applications in mind, and that universal procedures in bioconjugation chemistries should not be blindly followed without understanding their effects on QD stability.

The applicability of the unique optical properties of QDs were demonstrated in the QD-magnetic nanoparticle detection platform described in Chapter 4. In this platform, magnetic and fluorescent nanoparticles were encapsulated in separate micelles and mixed with analytes to form a sandwich assay. The multiplexing capabilities of QDs were utilized to simultaneously observe DNA and protein analytes with red and green fluorescent QDs, respectively. Furthermore, QD photostability enabled real-time visualization of the movement and sequential separation of analytes from solution via the magnetic nanoparticles. By conjugating proteins and ssDNA molecules onto the nanoparticle-containing micelle surfaces, this self-assembly based assay achieved molecular-level detection and separations.

Finally, in Chapter 5, a novel QD-DNA conjugation scheme was described. QDs with thin surface coatings were used in this study, facilitating their application in fluorescence resonance energy transfer-based sensing assays. These QDs demonstrated superior energy transfer compared to similar energy transfer systems involving QDs. Additionally, the broad utility of DNA as a building block nanomaterial was demonstrated by incorporating these QDs into DNA origami hinges.

Future Directions

Focusing on the QD conjugates discussed in Chapter 5, the broad flexibility of DNA nanomaterials opens avenues for several future directions. Regarding the QD-DNA conjugates themselves, improved conjugation steps may enable control over labeling

density (number of DNA strands per particle). In the methods described in Chapter 5, the QD-DNA conjugates averaged only ~1 DNA strand per particle. Whereas this is suitable for studies requiring monovalent binding of QDs, it is desirable to achieve a higher DNA labeling density for applications requiring multivalent binding of QDs. An example of when the former may be useful is an application involving fluorescence resonance energy transfer, where energy transfer efficiency is affected by the ratio of donors to quenchers. In this case, having only one binding site on the QD could make the analysis easier for a basic science study. On the other hand, an example of when the latter is useful could be a biosensing sandwich assay similar to the one described in Chapter 4, where additional binding sites on the QDs could provide higher detection sensitivity. To achieve better control over DNA conjugation to the QDs, it may be beneficial to employ a different click chemistry functional group than dibenzocyclooctyne-amine (DBCO). It was observed that QDs conjugated with DBCO were unstable because of the large hydrophobic moieties on DBCO (data not shown). As a result, QDs in this intermediate step often stick to the walls of their containers. Furthermore, the number of DBCO molecules that can be conjugated to a single QD is limited, as the QDs lose colloidal stability when their surface is saturated with the relatively hydrophobic DBCO molecules. As an alternative, it may be beneficial to conjugate an azide-containing molecule such as 3-azidoproplyamine or azido-PEG3-amine, which does not contain such large hydrophobic groups. This would likely eliminate the issue of colloidal instability from oversaturating the QD surface and yield more consistent results. Then, reaction parameters could potentially be tuned to allow for control over DNA labeling density on the QDs. Furthermore, this reaction design is quite practical,

as DBCO-modified DNA is commercially available, as are the azide containing chemicals mentioned above.

Beyond modifying the reaction parameters, additional functionality can be introduced to these QD conjugates using modified DNA. In particular, recent work in the Winter Lab has focused on the use of DNA with covalently linked photo-responsive azobenzene moieties. Light-responsive materials are desirable because they can be non-invasively manipulated without chemical contamination or heat input. Azobenzene undergoes isomerization between *cis* and *trans* conformations under different wavelengths of light irradiation. In its *cis* form (under ultraviolet irradiation, $300<\lambda_{ex}<400$ nm), azobenzene sterically hinders DNA duplex formation, thereby lowering the melting temperature (T_m) and preventing QDs from binding to other objects.[150] In its *trans* form (under visible irradiation, $\lambda_{ex}>400$ nm), azobenzene stabilizes DNA duplexes through favorable stacking interactions, enabling QDs to bind other objects. Using gold nanoparticles (AuNPs) with complementary ssDNA as fluorescence quenchers (as described in Chapter 5), reversible quenching of QD fluorescence may be possible. The efficiency of this quenching effect is extremely sensitive to the interparticle distance, so modulating the excitation source to control DNA hybridization between the particles could be used to manipulate the energy transfer efficiency (Figure 20).

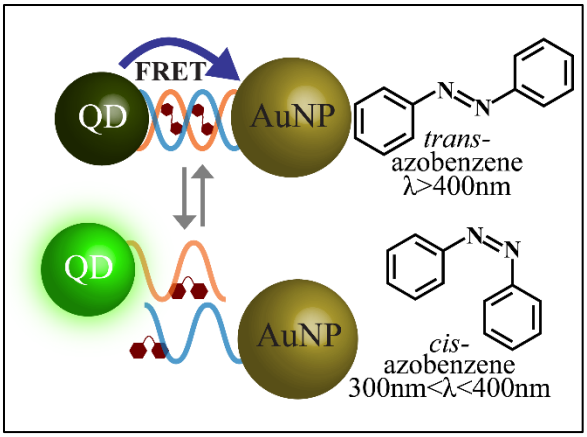

Figure 20 QD-AuNP photoswitchable probe design.

Within this system, several opportunities for exploring the design space exist. For instance, DNA hybridization and dehybridization kinetics can be tuned by exploring the DNA sequence design. To achieve photoswitching at room temperature, DNA containing *trans* azobenzene should have T_m > room temperature, whereas DNA containing *cis* azobenzene should have T_m < room temperature. If photoswitching experiments are conducted in the same buffer conditions (e.g., phosphate buffered saline, pH=7.2), the T_m will depend most strongly on DNA sequence and length. However, the incorporation of azobenzene moieties into the DNA introduces several complexities that will need to be resolved. For instance, Liang et al. demonstrated that incorporating alternating azobenzene groups into each strand of the DNA yields a stable and symmetric DNA structure compared to having all azobenzene groups in one strand.[151] By increasing the total number of azobenzene groups in a DNA strand of a given length, the difference in T_m between DNA containing *cis* and *trans* azobenzene groups increases. For further optimization, DNA sequence modifications of bases adjacent to the azobenzene groups may be adjusted. The *cis* to *trans* isomerization of azobenzene in DNA is believed to require free volume.[152] By introducing base pair

mismatches and abasic sites adjacent to azobenzene groups, Yan et al. demonstrated increased azobenzene isomerization efficiency.[153] By optimizing the DNA sequence design, the consistency of reversible photoswitching and quenching efficiency may be enhanced. In early studies in the Winter Lab, the DNA design with the greatest T_m difference from the study conducted by Liang et al. has been used to demonstrate reversible QD photoswitching (Figure 21).[151] However, beyond demonstrating proof-of-concept, this system has yet to be explored and optimized. Interesting parameters to investigate could include quenching efficiency and the kinetics and number of photoswitching cycles achievable.

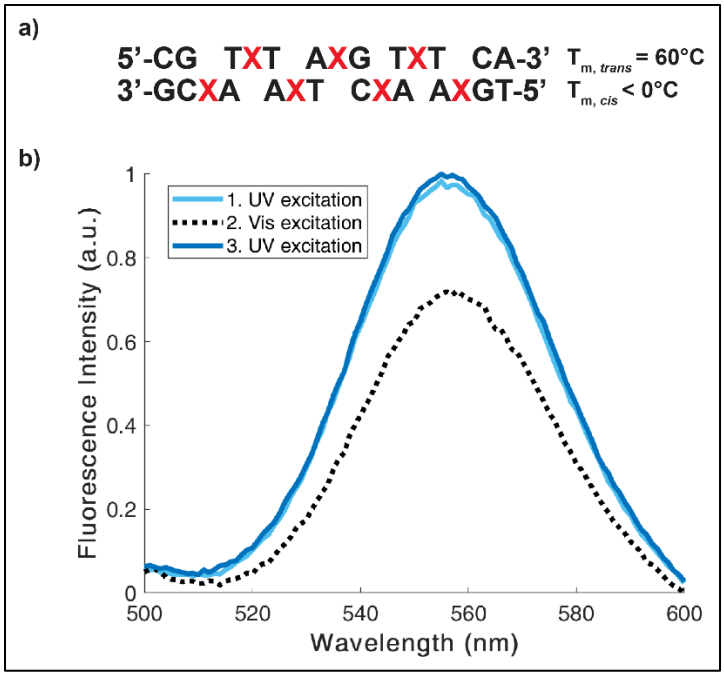

Figure 21 Demonstration of reversible photoswitching of QD-AuNP probes linked by complementary ssDNA containing azobenzene groups. (a) DNA sequence design (X=azobenzene). The top strand is conjugated to the QDs and the bottom strand is conjugated to the AuNPs. (b) UV excitation results in an "on" state in which the particles diffuse apart (blue), whereas visible excitation results in an "off" state where the particles are bound together (black). All three fluorescence spectra are from the same sample. The numbers in the legend correspond to the order in which measurements were taken.

These photoswitchable QDs lend themselves to a vast range of potential applications. Within the Winter Lab, where biological imaging is a focus, these QDs could find use in super-resolution microscopy as part of an ongoing collaboration with The Kner Imaging Lab at the University of Georgia. Fluorescence microscopy is an immensely important tool

for elucidating the forms and functions of subcellular structures because of its labeling specificity and *in vivo* compatibility. However, fluorescence microscopy is limited in resolution. Two points that are close together (e.g., < ~500 nm) will appear as a single point because of light diffraction. One technique to overcome this limitation is stochastic optical reconstruction microscopy (STORM). STORM accomplishes single molecule localization by using photoswitchable probes that can be randomly turned on/off so that individual particles can be imaged exclusive of their nearest neighbors. Thousands of optically resolvable images with random on/off fluorophore cycles are reconstructed into a single image, enabling fluorophore positions to be determined with high precision, thereby increasing resolution.[154]

An important factor in achieving high resolution in STORM is localization accuracy of the fluorescent probes, which is related to their rate of photon emission. The higher photon emission rate of QDs compared to typically employed molecular dyes can improve signal-to-noise ratio. Additionally, QD resistance to photobleaching maximizes the total number of photons that can be collected, improving imaging resolution and speed. However, because QDs are not inherently photoswitchable, they have found limited application in super-resolution microscopy.

Past approaches in utilizing QDs for single molecule localization microscopy have attempted to use QD blinking and photodegradation to achieve photoswitchability. QD blinking, random fluctuations in photoluminescence resulting from Auger recombination or hot electrons, achieves only limited contrast between "on" and "off" states, and therefore only limited improvements in resolution.[155] In photodegradation based approaches, QDs

were photo-oxidized, resulting in shrinkage of the QD core. This caused a gradual blue shift in emission that eventually entered the range of a collection window. However, this method is restricted by the degradation rate of QDs and the number of photons collected in a blue-shifted collection window.[61] It is therefore imperative to develop photoswitchable QDs that are more suitable for STORM. However, additional modifications would be necessary to facilitate these QDs use in imaging. For example, DNA-conjugated antibodies would be needed to give the QDs labeling specificity. Methods for cell entry would also be required, such as cell-penetrating peptides conjugated to the QD surface.[156]

Overall, further development of these QD-DNA conjugates could enable exploration of novel cellular mechanisms, potentially impacting healthcare by improving our understanding of biology. Beyond imaging, several additional applications of these versatile QD-DNA conjugates can be envisioned. Other photo-responsive materials have found uses in a variety of applications including molecular logic gates, data recording and storage, multi-photon devices, and optoelectronics.[157] In addition to conjugating these QDs with other nanoparticles, they may also be incorporated into DNA origami structures like those briefly discussed in Chapter 5 that enable elaborate three-dimensional spatial arrangements for investigating fundamental nanoscale physics.[158] QDs have demonstrated immense potential for a broad range of applications owing to their unique size-dependent electronic and optical properties. Here, we showed initial steps toward the development of stimuli-responsive QDs for biological imaging and sensing applications.

150. Asanuma, H., Ito, T., Yoshida, T., Liang, X. & Komiyama, M. Photoregulation of the formation and dissociation of a DNA duplex by using the cis-trans isomerization of azobenzene. *Angew. Chemie - Int. Ed.* **38**, 2393–2395 (1999).
151. Liang, X., Mochizuki, T. & Asanuma, H. A Supra-photoswitch Involving Sandwiched DNA Base Pairs and Azobenzenes for Light-Driven Nanostructures and Nanodevices. *Small* **5**, 1761–1768 (2009).
152. Samai, S., Bradley, D. J., Choi, T. L. Y., Yan, Y. & Ginger, D. S. Temperature-Dependent Photoisomerization Quantum Yields for Azobenzene-Modified DNA. *J. Phys. Chem. C* **121**, 6997–7004 (2017).
153. Yan, Y., Wang, X., Chen, J. I. L. & Ginger, D. S. Photoisomerization Quantum Yield of Azobenzene-Modified DNA Depends on Local Sequence. *J. Am. Chem. Soc.* **135**, 8382–8387 (2013).
154. Huang, B., Babcock, H. & Zhuang, X. Breaking the diffraction barrier: Super-resolution imaging of cells. *Cell* **143**, 1047–1058 (2010).
155. Lidke, K. A., Rieger, B., Jovin, T. M. & Heintzmann, R. Superresolution by localization of quantum dots using blinking statistics. *Opt. Express* **13**, 7052 (2005).
156. Xu, J. *et al.* Cell penetrating peptide mediated quantum dot delivery and release in live mammalian cells. in *2014 36th Annual International Conference of the IEEE Engineering in Medicine and Biology Society, EMBC 2014* 4260–4263 (Institute of Electrical and Electronics Engineers Inc., 2014). doi:10.1109/EMBC.2014.6944565
157. Zhang, J., Zou, Q. & Tian, H. Photochromic materials: More than meets the eye. *Advanced Materials* **25**, 378–399 (2013).
158. Johnson, J. A. *et al.* The path towards functional nanoparticle-DNA origami composites. *Materials Science and Engineering R: Reports* **138**, 153–209 (2019).

Bibliography

1. Murray, C. B., Kagan, C. R. & Bawendi, M. G. Synthesis and Characterization of Monodisperse Nanocrystals and Close-Packed Nanocrystal Assemblies. *Annu. Rev. Mater. Sci.* **30**, 545–610 (2000).
2. Chan, W. C. W. *et al.* Luminescent quantum dots for multiplexed biological detection and imaging. *Current Opinion in Biotechnology* **13**, 40–46 (2002).
3. Alivisatos, A. P. Semiconductor clusters, nanocrystals, and quantum dots. *Science (80-.).* **271**, 933–937 (1996).
4. Owens, F. J. & Poole, C. P. *The Physics and Chemistry of Nanosolids*. (John Wiley & Sons, 2008).
5. Martínez-Duart, J. M., Martín-Palma, R. J. & Agulló-Rueda, F. *Nanotechnology for Microelectronics and Optoelectronics*. *Nanotechnology for Microelectronics and Optoelectronics* (Elsevier Inc., 2006). doi:10.1016/B978-0-08-044553-3.X5000-0
6. Kalyanasundaram, K., Borgarello, E., Duonghong, D. & Grätzel, M. Cleavage of Water by Visible-Light Irradiation of Colloidal CdS Solutions; Inhibition of Photocorrosion by RuO2. *Angew. Chemie Int. Ed. English* **20**, 987–988 (1981).
7. Murray, C. B., Norris, D. J. & Bawendi, M. G. Synthesis and Characterization of Nearly Monodisperse CdE (E = S, Se, Te) Semiconductor Nanocrystallites. *J. Am. Chem. Soc.* **115**, 8706–8715 (1993).
8. Hines, M. A. & Guyot-Sionnest, P. Synthesis and characterization of strongly luminescing ZnS-capped CdSe nanocrystals. *J. Phys. Chem.* **100**, 468–471 (1996).
9. Reiss, P., Protière, M. & Li, L. Core/Shell Semiconductor Nanocrystals. *Small* **5**, 154–168 (2009).
10. Medintz, I. L., Uyeda, H. T., Goldman, E. R. & Mattoussi, H. Quantum dot bioconjugates for imaging, labelling and sensing. *Nature Materials* **4**, 435–446 (2005).
11. Chan, W. C. W. & Nie, S. Quantum Dot Bioconjugates for Ultrasensitive Nonisotopic Detection. *Science (80-.).* **281**, 2016–2018 (1998).
12. Bruchez, M., Moronne, M., Gin, P., Weiss, S. & Alivisatos, A. P. Semiconductor nanocrystals as fluorescent biological labels. *Science (80-.).* **281**, 2013–2016 (1998).
13. Banerjee, A., Pons, T., Lequeux, N. & Dubertret, B. Quantum dots-DNA bioconjugates: Synthesis to applications. *Interface Focus* **6**, (2016).
14. Hedi Mattoussi, *,† *et al.* Self-Assembly of CdSe−ZnS Quantum Dot Bioconjugates Using an Engineered Recombinant Protein. (2000). doi:10.1021/JA002535Y
15. Hermanson, G. T. *Bioconjugate Techniques: Third Edition*. *Bioconjugate Techniques: Third Edition* (Elsevier Inc., 2013). doi:10.1016/C2009-0-64240-9
16. Waalkes, M. P. Cadmium carcinogenesis. *Mutation Research - Fundamental and Molecular Mechanisms of Mutagenesis* **533**, 107–120 (2003).

17. Carey, G. H. *et al.* Colloidal Quantum Dot Solar Cells. *Chemical Reviews* **115**, 12732–12763 (2015).
18. Shirasaki, Y., Supran, G. J., Bawendi, M. G. & Bulović, V. Emergence of colloidal quantum-dot light-emitting technologies. *Nature Photonics* **7**, 13–23 (2013).
19. Biju, V. Chemical modifications and bioconjugate reactions of nanomaterials for sensing, imaging, drug delivery and therapy. *Chemical Society Reviews* **43**, 744–764 (2014).
20. Hildebrandt, N. *et al.* Energy transfer with semiconductor quantum dot bioconjugates: A versatile platform for biosensing, energy harvesting, and other developing applications. *Chemical Reviews* **117**, 536–711 (2017).
21. Resch-Genger, U., Grabolle, M., Cavaliere-Jaricot, S., Nitschke, R. & Nann, T. Quantum dots versus organic dyes as fluorescent labels. *Nature Methods* **5**, 763–775 (2008).
22. Hardman, R. A toxicologic review of quantum dots: Toxicity depends on physicochemical and environmental factors. *Environmental Health Perspectives* **114**, 165–172 (2006).
23. Kirchner, C. *et al.* Cytotoxicity of colloidal CdSe and CdSe/ZnS nanoparticles. *Nano Lett.* **5**, 331–338 (2005).
24. Derfus, A. M., Chan, W. C. W. & Bhatia, S. N. Probing the Cytotoxicity of Semiconductor Quantum Dots. *Nano Lett.* **4**, 11–18 (2004).
25. Hoshino, A. *et al.* Physicochemical properties and cellular toxicity of nanocrystal quantum dots depend on their surface modification. *Nano Lett.* **4**, 2163–2169 (2004).
26. Lewinski, N., Colvin, V. & Drezek, R. Cytotoxicity of nanopartides. *Small* **4**, 26–49 (2008).
27. Tsoi, K. M., Dai, Q., Alman, B. A. & Chan, W. C. W. Are quantum dots toxic? Exploring the discrepancy between cell culture and animal studies. *Acc. Chem. Res.* **46**, 662–671 (2013).
28. Yong, K. T. *et al.* Nanotoxicity assessment of quantum dots: From cellular to primate studies. *Chemical Society Reviews* **42**, 1236–1250 (2013).
29. Manshian, B. B. *et al.* Cell type-dependent changes in CdSe/ZnS quantum dot uptake and toxic endpoints. *Toxicol. Sci.* **144**, 246–58 (2015).
30. Nagy, A. *et al.* Comprehensive analysis of the effects of CdSe quantum dot size, surface charge, and functionalization on primary human lung cells. *ACS Nano* **6**, 4748–4762 (2012).
31. Rani, A., Kumar, A., Lal, A. & Pant, M. Cellular mechanisms of cadmium-induced toxicity: A review. *International Journal of Environmental Health Research* **24**, 378–399 (2014).
32. Chen, N. *et al.* The cytotoxicity of cadmium-based quantum dots. *Biomaterials* **33**, 1238–1244 (2012).
33. Pelley, J. L., Daar, A. S. & Saner, M. A. State of academic knowledge on toxicity and biological fate of quantum dots. *Toxicol. Sci.* **112**, 276–96 (2009).
34. Rocha, T. L., Mestre, N. C., Sabóia-Morais, S. M. T. & Bebianno, M. J. Environmental behaviour and ecotoxicity of quantum dots at various trophic

levels: A review. *Environment International* **98**, 1–17 (2017).
35. Brunetti, V. *et al.* InP/ZnS as a safer alternative to CdSe/ZnS core/shell quantum dots: In vitro and in vivo toxicity assessment. *Nanoscale* **5**, 307–317 (2013).
36. Lin, G. *et al.* In vivo toxicity assessment of non-cadmium quantum dots in BALB/c mice. *Nanomedicine Nanotechnology, Biol. Med.* **11**, 341–350 (2015).
37. Liu, J. *et al.* Aqueous synthesis and bio-imaging application of highly luminescent and low cytotoxicity Mn2+-doped ZnSe nanocrystals. *Mater. Lett.* **65**, 2139–2141 (2011).
38. Zhou, R. *et al.* Low-toxic Mn-doped ZnSe@ZnS quantum dots conjugated with nano-hydroxyapatite for cell imaging. *Nanoscale* **6**, 14319–14325 (2014).
39. Plumley, J. B. *et al.* Noncytotoxic Mn-doped ZnSe/ZnS quantum dots for biomedical applications. in *Colloidal Nanoparticles for Biomedical Applications IX* **8955**, 895513 (SPIE, 2014).
40. Drobintseva, A. O. *et al.* Colloidal CdSe and ZnSe/Mn quantum dots: Their cytotoxicity and effects on cell morphology. *St. Petersbg. Polytech. Univ. J. Phys. Math.* **1**, 272–277 (2015).
41. Swift, B. J. F. & Baneyx, F. Microbial uptake, toxicity, and fate of biofabricated ZnS:Mn nanocrystals. *PLoS One* **10**, e0124916 (2015).
42. Yang, Y. *et al.* Hepatotoxicity assessment of Mn-doped ZnS quantum dots after repeated administration in mice. *Int. J. Nanomedicine* **10**, 5787 (2015).
43. Mohammad, F. & Al-Lohedan, H. A. Toxicity assessment of engineered Mn–ZnS quantum dots in vitro. *J. Mater. Sci.* **51**, 9207–9216 (2016).
44. Chang, E., Thekkek, N., Yu, W. W., Colvin, V. L. & Drezek, R. Evaluation of quantum dot cytotoxicity based on intracellular uptake. *Small* **2**, 1412–1417 (2006).
45. Clift, M. J. D. *et al.* The impact of different nanoparticle surface chemistry and size on uptake and toxicity in a murine macrophage cell line. *Toxicol. Appl. Pharmacol.* **232**, 418–427 (2008).
46. Peng, L. *et al.* Cellular uptake, elimination and toxicity of CdSe/ZnS quantum dots in HepG2 cells. *Biomaterials* **34**, 9545–9558 (2013).
47. Lovrić, J. *et al.* Differences in subcellular distribution and toxicity of green and red emitting CdTe quantum dots. *J. Mol. Med.* **83**, 377–385 (2005).
48. Soo Choi, H. *et al.* Renal clearance of quantum dots. *Nat. Biotechnol.* **25**, 1165–1170 (2007).
49. Xu, J. *et al.* Micelle-templated composite quantum dots for super-resolution imaging. *Nanotechnology* **25**, 195601 (2014).
50. Pradhan, N. & Peng, X. Efficient and color-tunable Mn-doped ZnSe nanocrystal emitters: Control of optical performance via greener synthetic chemistry. *J. Am. Chem. Soc.* **129**, 3339–3347 (2007).
51. Pradhan, N., Battaglia, D. M., Liu, Y. & Peng, X. Efficient, stable, small, and water-soluble doped ZnSe nanocrystal emitters as non-cadmium biomedical labels. *Nano Lett.* **7**, 312–317 (2007).
52. Ross, J. H. A Color Test for Chloroform and Chloral Hydrate. *J. Biol. Chem.* **58**, 641–642 (1923).

53. Anderson, N. C., Hendricks, M. P., Choi, J. J. & Owen, J. S. Ligand exchange and the stoichiometry of metal chalcogenide nanocrystals: Spectroscopic observation of facile metal-carboxylate displacement and binding. *J. Am. Chem. Soc.* **135**, 18536–18548 (2013).
54. Shen, Y., Tan, R., Gee, M. Y. & Greytak, A. B. Quantum yield regeneration: Influence of neutral ligand binding on photophysical properties in colloidal core/shell quantum dots. *ACS Nano* **9**, 3345–3359 (2015).
55. Oh, N. & Park, J. H. Endocytosis and exocytosis of nanoparticles in mammalian cells. *International Journal of Nanomedicine* **9**, 51–63 (2014).
56. Salin, K. *et al.* Individuals with higher metabolic rates have lower levels of reactive oxygen species in vivo. *Biol. Lett.* **11**, (2015).
57. Lovrić, J., Cho, S. J., Winnik, F. M. & Maysinger, D. Unmodified cadmium telluride quantum dots induce reactive oxygen species formation leading to multiple organelle damage and cell death. *Chem. Biol.* **12**, 1227–1234 (2005).
58. Ipe, B. I., Lehnig, M. & Niemeyer, C. M. On the generation of free radical species from quantum dots. *Small* **1**, 706–709 (2005).
59. Lee, K. H., Porter, T. & Winter, J. O. Fluorescence loss of commercial aqueous quantum dots during preparation for bioimaging. *MRS Commun.* **9**, 702–709 (2019).
60. Chan, W. C. W. & Nie, S. Quantum dot bioconjugates for ultrasensitive nonisotopic detection. *Science (80-.).* **281**, 2016–2018 (1998).
61. van Sark, W. G. J. H. M., Frederix, P. L. T. M., Bol, A. A., Gerritsen, H. C. & Meijerink, A. Blueing, Bleaching, and Blinking of Single CdSe/ZnS Quantum Dots. *ChemPhysChem* **3**, 871–879 (2002).
62. Wu, X. *et al.* Immunofluorescent labeling of cancer marker Her2 and other cellular targets with semiconductor quantum dots. *Nat. Biotechnol.* **21**, 41–46 (2003).
63. Dubertret, B. *et al.* In vivo imaging of quantum dots encapsulated in phospholipid micelles. *Science (80-.).* **298**, 1759–1762 (2002).
64. Shiohara, A., Hoshino, A., Hanaki, K. I., Suzuki, K. & Yamamoto, K. On the cyto-toxicity caused by quantum dots. *Microbiol. Immunol.* **48**, 669–675 (2004).
65. Ye, L. *et al.* A pilot study in non-human primates shows no adverse response to intravenous injection of quantum dots. *Nat. Nanotechnol.* **7**, 453–458 (2012).
66. Grim, J. Q., Manna, L. & Moreels, I. A sustainable future for photonic colloidal nanocrystals. *Chem. Soc. Rev.* **44**, 5897–5914 (2015).
67. Banerjee, A. *et al.* Fast, Efficient, and Stable Conjugation of Multiple DNA Strands on Colloidal Quantum Dots. *Bioconjug. Chem.* **26**, 1582–1589 (2015).
68. Aldana, J., Wang, Y. A. & Peng, X. Photochemical instability of CdSe nanocrystals coated by hydrophilic thiols. *J. Am. Chem. Soc.* **123**, 8844–8850 (2001).
69. Zhang, Y., Chen, Y., Westerhoff, P. & Crittenden, J. C. Stability and removal of water soluble CdTe quantum dots in water. *Environ. Sci. Technol.* **42**, 321–325 (2008).
70. Hermanson, G. T. *Bioconjugate techniques*. (Academic Press, 1996).
71. Kubin, R. F. & Fletcher, A. N. Fluorescence quantum yields of some rhodamine

dyes. *J. Lumin.* **27**, 455–462 (1982).
72. Velapoldi, R. A. Considerations on organic compounds in solution and inorganic ions in glasses as fluorescent Standard Reference Materials. *J. Res. Natl. Bur. Stand. (1934).* **76A**, 641 (1972).
73. Wu, Y. *et al.* The development of quantum dot calibration beads and quantitative multicolor bioassays in flow cytometry and microscopy. *Anal. Biochem.* **364**, 180–192 (2007).
74. Gaigalas, A. K. & Wang, L. Measurement of the fluorescence quantum yield using a spectrometer with an integrating sphere detector. *J. Res. Natl. Inst. Stand. Technol.* **113**, 17–28 (2008).
75. Deerinck, T. J. The Application of Fluorescent Quantum Dots to Confocal, Multiphoton, and Electron Microscopic Imaging. *Toxicol. Pathol.* **36**, 112–116 (2008).
76. Winter, J. O., Liu, T. Y., Korgel, B. A. & Schmidt, C. E. Recognition Molecule Directed Interfacing Between Semiconductor Quantum Dots and Nerve Cells. *Adv. Mater.* **13**, 1673–1677 (2001).
77. Pfeiffer, C. *et al.* Interaction of colloidal nanoparticles with their local environment: The (ionic) nanoenvironment around nanoparticles is different from bulk and determines the physico-chemical properties of the nanoparticles. *Journal of the Royal Society Interface* **11**, 20130931–20130931 (2014).
78. Moore, T. L. *et al.* Nanoparticle colloidal stability in cell culture media and impact on cellular interactions. *Chem. Soc. Rev.* **44**, 6287–6305 (2015).
79. Wang, F., Tang, R. & Buhro, W. E. The trouble with TOPO; identification of adventitious impurities beneficial to the growth of cadmium selenide quantum dots, rods, and wires. *Nano Lett.* **8**, 3521–3524 (2008).
80. Van Sark, W. G. J. H. M. *et al.* Photooxidation and photobleaching of single CdSe/ZnS quantum dots probed by room-temperature time-resolved spectroscopy. *J. Phys. Chem. B* **105**, 8281–8284 (2001).
81. Rodriguez-Viejo, J. *et al.* Cathodoluminescence and photoluminescence of highly luminescent CdSe/ZnS quantum dot composites. *Appl. Phys. Lett.* **70**, 2132–2134 (1997).
82. Mahajan, K. D. *et al.* Biomolecular detection, tracking, and manipulation using a magnetic nanoparticle-quantum dot platform. *J. Mater. Chem. B* (2020). doi:10.1039/c9tb02481f
83. Gao, X., Chan, W. C. W. & Nie, S. Quantum-dot nanocrystals for ultrasensitive biological labeling and multicolor optical encoding. *J. Biomed. Opt.* **7**, 532 (2002).
84. Clapp, A. R. *et al.* Fluorescence Resonance Energy Transfer between Quantum Dot Donors and Dye-Labeled Protein Acceptors. *J. Am. Chem. Soc.* **126**, 301–310 (2004).
85. Wu, P., Hou, X., Xu, J. J. & Chen, H. Y. Ratiometric fluorescence, electrochemiluminescence, and photoelectrochemical chemo/biosensing based on semiconductor quantum dots. *Nanoscale* **8**, 8427–8442 (2016).
86. Gloag, L., Mehdipour, M., Chen, D., Tilley, R. D. & Gooding, J. J. Advances in the Application of Magnetic Nanoparticles for Sensing. *Advanced Materials* **31**,

e1904385 (2019).
87. Fratzl, M. *et al.* Magnetophoretic induced convective capture of highly diffusive superparamagnetic nanoparticles. *Soft Matter* **14**, 2671–2681 (2018).
88. Wang, J., Li, H., Cho, E. Y., Lefebvere, J. C. & Cybart, S. A. Measurement of Magnetic Nanoparticles Using High Transition Temperature Superconducting Quantum Interference Devices. *IEEE Trans. Appl. Supercond.* **29**, 1–4 (2019).
89. Yeap, S. P., Leong, S. S., Ahmad, A. L., Ooi, B. S. & Lim, J. On size fractionation of iron oxide nanoclusters by low magnetic field gradient. *J. Phys. Chem. C* **118**, 24042–24054 (2014).
90. Nabar, G. M., Winter, J. O. & Wyslouzil, B. E. Nanoparticle packing within block copolymer micelles prepared by the interfacial instability method. *Soft Matter* **14**, 3324–3335 (2018).
91. Rong, G., Tuttle, E. E., Neal Reilly, A. & Clark, H. A. Recent Developments in Nanosensors for Imaging Applications in Biological Systems. *Annu. Rev. Anal. Chem.* **12**, 109–128 (2019).
92. Li, L. *et al.* Facile synthesis of magnetic fluorescent nanoparticles: adsorption and selective detection of Hg(ii) in water. *J. Mater. Chem. C* **6**, 2360–2369 (2018).
93. Wu, L. *et al.* Detection of malachite green in fish based on magnetic fluorescent probe of CdTe QDs/nano-Fe3O4@MIPs. *Spectrochim. Acta Part A Mol. Biomol. Spectrosc.* **196**, 117–122 (2018).
94. Ruan, G. & Winter, J. O. Alternating-color quantum dot nanocomposites for particle tracking. *Nano Lett.* **11**, 941–945 (2011).
95. Ruan, G. *et al.* Simultaneous magnetic manipulation and fluorescent tracking of multiple individual hybrid nanostructures. *Nano Lett.* **10**, 2220–2224 (2010).
96. Lee, K. H., Yang, G., Wyslouzil, B. E. & Winter, J. O. Electrohydrodynamic Mixing-Mediated Nanoprecipitation for Polymer Nanoparticle Synthesis. *ACS Appl. Polym. Mater.* **1**, 691–700 (2019).
97. Meijering, E., Dzyubachyk, O. & Smal, I. Methods for cell and particle tracking. in *Methods in Enzymology* **504**, 183–200 (Academic Press Inc., 2012).
98. Duong, A. D., Ruan, G., Mahajan, K., Winter, J. O. & Wyslouzil, B. E. Scalable, semicontinuous production of micelles encapsulating nanoparticles via electrospray. *Langmuir* **30**, 3939–3948 (2014).
99. Wong, M. H. *et al.* Lipid Exchange Envelope Penetration (LEEP) of Nanoparticles for Plant Engineering: A Universal Localization Mechanism. *Nano Lett.* **16**, 1161–1172 (2016).
100. Vieira, G. *et al.* Magnetic Wire Traps and Programmable Manipulation of Biological Cells. *Phys. Rev. Lett.* **103**, 128101 (2009).
101. Schrittwieser, S. *et al.* Homogeneous Biosensing Based on Magnetic Particle Labels. *Sensors* **16**, 828 (2016).
102. Stanisavljevic, M., Krizkova, S., Vaculovicova, M., Kizek, R. & Adam, V. Quantum dots-fluorescence resonance energy transfer-based nanosensors and their application. *Biosensors and Bioelectronics* **74**, 562–574 (2015).
103. Neuman, K. C. & Nagy, A. Single-molecule force spectroscopy: Optical tweezers, magnetic tweezers and atomic force microscopy. *Nature Methods* **5**, 491–505

(2008).
104. Bissell, R. A., Córdova, E., Kaifer, A. E. & Stoddart, J. F. A chemically and electrochemically switchable molecular shuttle. *Nature* **369**, 133–137 (1994).
105. Rosenthal, S. J., Chang, J. C., Kovtun, O., McBride, J. R. & Tomlinson, I. D. Biocompatible quantum dots for biological applications. *Chem. Biol.* **18**, 10–24 (2011).
106. Geiss, G. K. *et al.* Direct multiplexed measurement of gene expression with color-coded probe pairs. *Nat. Biotechnol.* **26**, 317–325 (2008).
107. Dehankar, A., Porter, T., Johnson, J. A., Castro, C. E. & Winter, J. O. Compact quantum dot surface modification to enable emergent behaviors in quantum dot-DNA composites. *J. Chem. Phys.* **151**, (2019).
108. Zhang, Y. & Wang, T. H. Quantum dot enabled molecular sensing and diagnostics. *Theranostics* **2**, 631–654 (2012).
109. Shi, J., Tian, F., Lyu, J. & Yang, M. Nanoparticle based fluorescence resonance energy transfer (FRET) for biosensing applications. *Journal of Materials Chemistry B* **3**, 6989–7005 (2015).
110. Petryayeva, E., Algar, W. R. & Medintz, I. L. Quantum dots in bioanalysis: a review of applications across various platforms for fluorescence spectroscopy and imaging. *Appl. Spectrosc.* **67**, 215–52 (2013).
111. Samanta, A., Zhou, Y., Zou, S., Yan, H. & Liu, Y. Fluorescence quenching of quantum dots by gold nanoparticles: A potential long range spectroscopic ruler. *Nano Lett.* **14**, 5052–5057 (2014).
112. Ponnuswamy, N. *et al.* Oligolysine-based coating protects DNA nanostructures from low-salt denaturation and nuclease degradation. *Nat. Commun.* **8**, 1–9 (2017).
113. Bui, H. *et al.* Programmable periodicity of quantum dot arrays with DNA origami nanotubes. *Nano Lett.* **10**, 3367–3372 (2010).
114. Wang, G., Li, Z. & Ma, N. Next-Generation DNA-Functionalized Quantum Dots as Biological Sensors. *ACS Chemical Biology* **13**, 1705–1713 (2018).
115. Algar, W. R. *et al.* The controlled display of biomolecules on nanoparticles: A challenge suited to bioorthogonal chemistry. *Bioconjugate Chemistry* **22**, 825–858 (2011).
116. Li, M. *et al.* Size-Dependent Energy Transfer between CdSe/ZnS Quantum Dots and Gold Nanoparticles. *J. Phys. Chem. Lett.* **2**, 2125–2129 (2011).
117. Samanta, A., Deng, Z., Liu, Y. & Yan, H. A perspective on functionalizing colloidal quantum dots with DNA. *Nano Research* **6**, 853–870 (2013).
118. Blanco-Canosa, J. B. *et al.* Recent progress in the bioconjugation of quantum dots. *Coordination Chemistry Reviews* **263**–**264**, 101–137 (2014).
119. Deng, Z., Samanta, A., Nangreave, J., Yan, H. & Liu, Y. Robust DNA-functionalized core/shell quantum dots with fluorescent emission spanning from UV-vis to near-IR and compatible with DNA-directed self-assembly. *J. Am. Chem. Soc.* **134**, 17424–17427 (2012).
120. Parak, W. J. *et al.* Cell Motility and Metastatic Potential Studies Based on Quantum Dot Imaging of Phagokinetic Tracks. *Adv. Mater.* **14**, 882–885 (2002).
121. Sun, D. & Gang, O. DNA-functionalized quantum dots: Fabrication, structural,

and physicochemical properties. *Langmuir* **29**, 7038–7046 (2013).
122. Medintz, I. L. *et al.* A reactive peptidic linker for self-assembling hybrid quantum dot-DNA bioconjugates. *Nano Lett.* **7**, 1741–1748 (2007).
123. Banerjee, A., Pons, T., Lequeux, N. & Dubertret, B. Quantum dots-DNA bioconjugates: Synthesis to applications. *Interface Focus* **6**, 20160064 (2016).
124. Pinaud, F., King, D., Moore, H. P. & Weiss, S. Bioactivation and Cell Targeting of Semiconductor CdSe/ZnS Nanocrystals with Phytochelatin-Related Peptides. *J. Am. Chem. Soc.* **126**, 6115–6123 (2004).
125. Wang, W. *et al.* Multifunctional and High Affinity Polymer Ligand that Provides Bio-Orthogonal Coating of Quantum Dots. *Bioconjug. Chem.* **27**, 2024–2036 (2016).
126. Xu, J., Ruchala, P., Ebenstain, Y., Li, J. J. & Weiss, S. Stable, Compact, Bright Biofunctional Quantum Dots with Improved Peptide Coating. *J. Phys. Chem. B* **116**, 11370–11378 (2012).
127. Zhang, X., Servos, M. R. & Liu, J. Instantaneous and quantitative functionalization of gold nanoparticles with thiolated DNA using a pH-assisted and surfactant-free route. *J. Am. Chem. Soc.* **134**, 7266–7269 (2012).
128. Marras, A. E., Zhou, L., Su, H. J. & Castro, C. E. Programmable motion of DNA origami mechanisms. *Proc. Natl. Acad. Sci. U. S. A.* **112**, 713–718 (2015).
129. Grabolle, M. *et al.* Determination of the fluorescence quantum yield of quantum dots: Suitable procedures and achievable uncertainties. *Anal. Chem.* **81**, 6285–6294 (2009).
130. Castro, C. E. *et al.* A primer to scaffolded DNA origami. *Nat. Methods* **8**, 221–229 (2011).
131. Green, M. The nature of quantum dot capping ligands. *Journal of Materials Chemistry* **20**, 5797–5809 (2010).
132. Hermanson, G. T. *Bioconjugate Techniques*. *Bioconjugate Techniques* (Elsevier Inc., 2008). doi:10.1016/B978-0-12-370501-3.X0001-X
133. Thorek, D. L. J., Elias, ew R. & Tsourkas, A. Comparative Analysis of Nanoparticle-Antibody Conjugations: Carbodiimide Versus Click Chemistry. *Mol. Imaging* **8**, 7290.2009.00021 (2009).
134. Martin, T. G. & Dietz, H. Magnesium-free self-assembly of multi-layer DNA objects. *Nat. Commun.* **3**, 1–6 (2012).
135. Zhang, D. & Nettles, C. B. A Generalized Model on the Effects of Nanoparticles on Fluorophore Fluorescence in Solution. *J. Phys. Chem. C* **119**, 7941–7948 (2015).
136. Zhang, X. *et al.* Experimental and theoretical investigation of the distance dependence of localized surface plasmon coupled förster resonance energy transfer. *ACS Nano* **8**, 1273–1283 (2014).
137. Song, J. H., Atay, T., Shi, S., Urabe, H. & Nurmikko, A. V. Large enhancement of fluorescence efficiency from CdSe/ZnS quantum dots induced by resonant coupling to spatially controlled surface plasmons. *Nano Lett.* **5**, 1557–1561 (2005).
138. Algar, W. R. & Krull, U. J. Adsorption and hybridization of oligonucleotides on mercaptoacetic acid-capped CdSe/ZnS quantum dots and quantum dot-

oligonucleotide conjugates. *Langmuir* **22**, 11346–11352 (2006).
139. Kubista, M., Sjöback, R., Eriksson, S. & Albinsson, B. Experimental correction for the inner-filter effect in fluorescence spectra. *Analyst* **119**, 417–419 (1994).
140. Härtling, T., Reichenbach, P. & Eng, L. M. Near-field coupling of a single fluorescent molecule and a spherical gold nanoparticle. *Opt. Express* **15**, 12806 (2007).
141. Albani, J. R. *Principles and Applications of Fluorescence Spectroscopy*. *Principles and Applications of Fluorescence Spectroscopy* (Blackwell Publishing Ltd, 2007). doi:10.1002/9780470692059
142. Zhang, C. Y. & Johnson, L. W. Quantum dot-based fluorescence resonance energy transfer with improved FRET efficiency in capillary flows. *Anal. Chem.* **78**, 5532–5537 (2006).
143. Zhou, D. *et al.* Fluorescence resonance energy transfer between a quantum dot donor and a dye acceptor attached to DNA. *Chem. Commun.* 4807–4809 (2005). doi:10.1039/b508911e
144. Kim, Y. P. *et al.* Energy transfer-based multiplexed assay of proteases by using gold nanoparticle and quantum dot conjugates on a surface. *Anal. Chem.* **80**, 4634–4641 (2008).
145. Gueroui, Z. & Libchaber, A. Single-molecule measurements of gold-quenched quantum dots. *Phys. Rev. Lett.* **93**, 166108 (2004).
146. Chou, K. F. & Dennis, A. M. Förster resonance energy transfer between quantum dot donors and quantum dot acceptors. *Sensors (Switzerland)* **15**, 13288–13325 (2015).
147. Daksh, D., Rawtani, D. & Agrawal, Y. K. Recent developments in bio-nanoelectronics devices: A review. *Journal of Bionanoscience* **10**, 81–93 (2016).
148. Du, K. *et al.* Quantum dot-DNA origami binding: A single particle, 3D, real-time tracking study. *Chem. Commun.* **49**, 907–909 (2013).
149. Fan, Q., Nabar, G., Miller, C., Castro, C. & Winter, J. Photo-switchable quantum dots based on reversible FRET. *Proc. SPIE* **8954**, (2014).
150. Asanuma, H., Ito, T., Yoshida, T., Liang, X. & Komiyama, M. Photoregulation of the formation and dissociation of a DNA duplex by using the cis-trans isomerization of azobenzene. *Angew. Chemie - Int. Ed.* **38**, 2393–2395 (1999).
151. Liang, X., Mochizuki, T. & Asanuma, H. A Supra-photoswitch Involving Sandwiched DNA Base Pairs and Azobenzenes for Light-Driven Nanostructures and Nanodevices. *Small* **5**, 1761–1768 (2009).
152. Samai, S., Bradley, D. J., Choi, T. L. Y., Yan, Y. & Ginger, D. S. Temperature-Dependent Photoisomerization Quantum Yields for Azobenzene-Modified DNA. *J. Phys. Chem. C* **121**, 6997–7004 (2017).
153. Yan, Y., Wang, X., Chen, J. I. L. & Ginger, D. S. Photoisomerization Quantum Yield of Azobenzene-Modified DNA Depends on Local Sequence. *J. Am. Chem. Soc.* **135**, 8382–8387 (2013).
154. Huang, B., Babcock, H. & Zhuang, X. Breaking the diffraction barrier: Super-resolution imaging of cells. *Cell* **143**, 1047–1058 (2010).
155. Lidke, K. A., Rieger, B., Jovin, T. M. & Heintzmann, R. Superresolution by

localization of quantum dots using blinking statistics. *Opt. Express* **13**, 7052 (2005).
156. Xu, J. *et al.* Cell penetrating peptide mediated quantum dot delivery and release in live mammalian cells. in *2014 36th Annual International Conference of the IEEE Engineering in Medicine and Biology Society, EMBC 2014* 4260–4263 (Institute of Electrical and Electronics Engineers Inc., 2014). doi:10.1109/EMBC.2014.6944565
157. Zhang, J., Zou, Q. & Tian, H. Photochromic materials: More than meets the eye. *Advanced Materials* **25**, 378–399 (2013).
158. Johnson, J. A. *et al.* The path towards functional nanoparticle-DNA origami composites. *Materials Science and Engineering R: Reports* **138**, 153–209 (2019).
159. Barton, A. F. M. *CRC handbook of solubility parameters and other cohesion parameters*.
160. Wu, C.-S., Cupps, J. M. & Fan, X. Compact quantum dot probes for rapid and sensitive DNA detection using highly efficient fluorescence resonant energy transfer. *Nanotechnology* **20**, 305502 (2009).
161. Zhou, D. *et al.* A compact functional quantum dot-DNA conjugate: Preparation, hybridization, and specific label-free DNA detection. *Langmuir* **24**, 1659–1664 (2008).
162. Wu, J., Wang, H., Zhu, A. & Long, F. Adsorption Kinetics of Single-Stranded DNA on Functional Silica Surfaces and Its Influence Factors: An Evanescent-Wave Biosensor Study. *ACS Omega* **3**, 5605–5614 (2018).
163. Lee, J., Choi , Y., Kim, J., Park, E. & Song, R. Positively Charged Compact Quantum Dot-DNA Complexes for Detection of Nucleic Acids. *ChemPhysChem* **10**, 806–811 (2009).
164. Sedighi, A. & Krull, U. J. Rapid Immobilization of Oligonucleotides at High Density on Semiconductor Quantum Dots and Gold Nanoparticles. *Langmuir* **32**, 13500–13509 (2016).
165. Dommerholt, J., Rutjes, F. P. J. T. & van Delft, F. L. Strain-Promoted 1,3-Dipolar Cycloaddition of Cycloalkynes and Organic Azides. *Top. Curr. Chem.* **374**, 20–40 (2016).
166. Hao, J., Huang, L. L., Zhang, R., Wang, H. Z. & Xie, H. Y. A mild and reliable method to label enveloped virus with quantum dots by copper-free click chemistry. *Anal. Chem.* **84**, 8364–8370 (2012).
167. Zhang, X., Servos, M. R. & Liu, J. Instantaneous and quantitative functionalization of gold nanoparticles with thiolated DNA using a pH-assisted and surfactant-free route. *J. Am. Chem. Soc.* **134**, 7266–7269 (2012).
168. Lakowicz, J. R. *Principles of Fluorescence Spectroscopy*. (2005).

Appendix A

Chapter 2 Supplementary Information: Toxicity Assessment of Micelle encapsulated Mn-doped ZnSe Quantum dots

Supplementary Figures

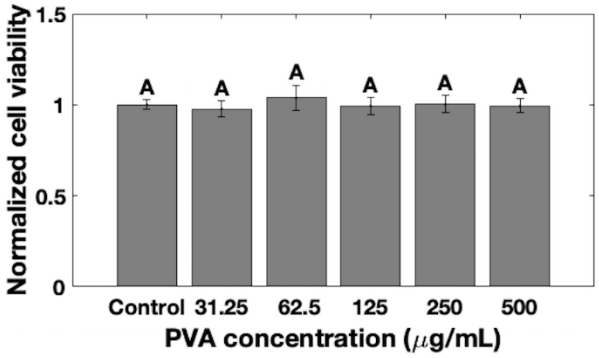

Figure 22 MTT assay cell viability of PVA treated cells

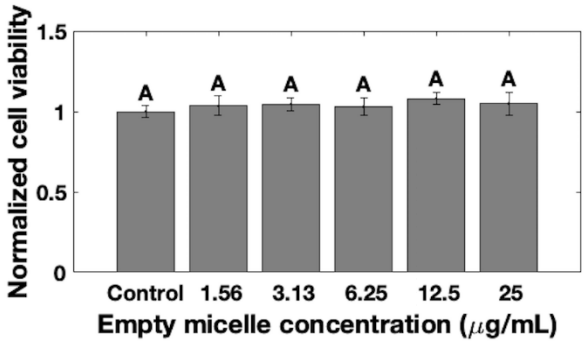

Figure 23 MTT assay cell viability of empty micelle treated cells (the concentration represents the concentration of QDs that these micelles would encapsulate with the standard recipe)

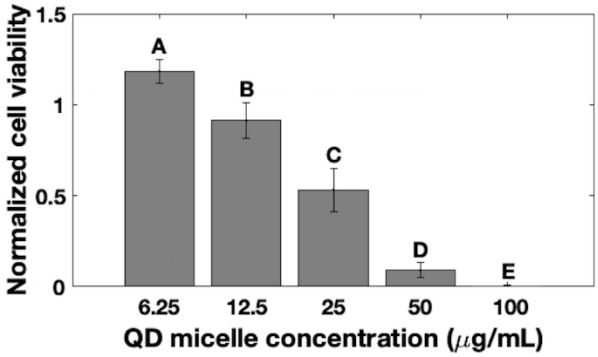

Figure 24 MTT assay cell viability of QD-micelle (concentrated) treated cells

Chloroform concentration assay

300 µl of the unknown sample or the standard calibration samples were mixed with 200 µl of 50% NaOH solution in a 1.5 ml centrifuge tube, followed by adding 250 µl of pyridine. Since PS-PEO has a much higher solubility in pyridine than in water, most of the polymers would be transferred into the pyridine phase, leaving no chloroform molecules trapped in the micelles. The mixture was then vortexed at 2000 rpm for 1 min, and incubated in 90°C

water bath for 2 min. The mixture was swiftly transferred to a cooling water bath to stop the reaction. Then, the vial was centrifuged briefly to cause water/pyridine phase separation, and 50 µl of pyridine was transferred to another vial. 150 µl of pyridine was added to the pyridine solution, and the solution was centrifuged at 20,000 rcf for 1 min. The supernatant was transparent with a pink to dark red color depending on the chloroform concentration in the sample. This supernatant solution has an absorbance peak at 540 nm, and the chloroform concentration is linearly proportional to the absorbance.

Live-Dead flow-cytometry assay

Live-Dead flow cytometry assay was performed with the LIVE/DEAD™ Cell Vitality Assay Kit, C12 Resazurin/SYTOX™ Green (L34951, Invitrogen). Briefly, cells were seeded in a 12 well plates at 80,000 cells per well with 3 replicas for each sample/control. After 24 h incubation, cell medium was removed from sample wells, and 1 mL of desired concentration nanoparticle solution was added to the plate and incubated with the cells for 24 h. Next, the cells were harvested in a 15 mL centrifuge tube and washed with PBS to remove the NPs. Finally, washed cells at 1 x 10^6 cell/mL were treated with C_{12}-resazurin (50 nM) and SYTOX Green (10 nM) stain for 15 minutes at 37°C. Cells were then analyzed by flow cytometry after dilution by exciting at 488 nm and measuring the fluorescence emission at 530 nm and 585 nm. The Live stain, C_{12}-resazurin, changed structure in a metabolically active cell by reduction to generate red emission, whereas the green nucleic acid SYTOX stain only entered the nucleus of cells with damaged/compromised membranes observed in dead or injured cells. Flow-cytometry measures the fluorescence emission of each dye per cell. Thus, high red and low green emissions are observed in live

cells, high green and low red emission are observed in dead cells, and low red and green emissions are observed in unstained cells. The cells that display both stains at high-levels are considered injured cells that display lower metabolic activity and the beginnings of membrane destruction.

Appendix B

Chapter 3 Supplementary Information: Fluorescence Loss of Commercial Aqueous Quantum Dots during Preparation for Bioimaging

Supplementary Figures

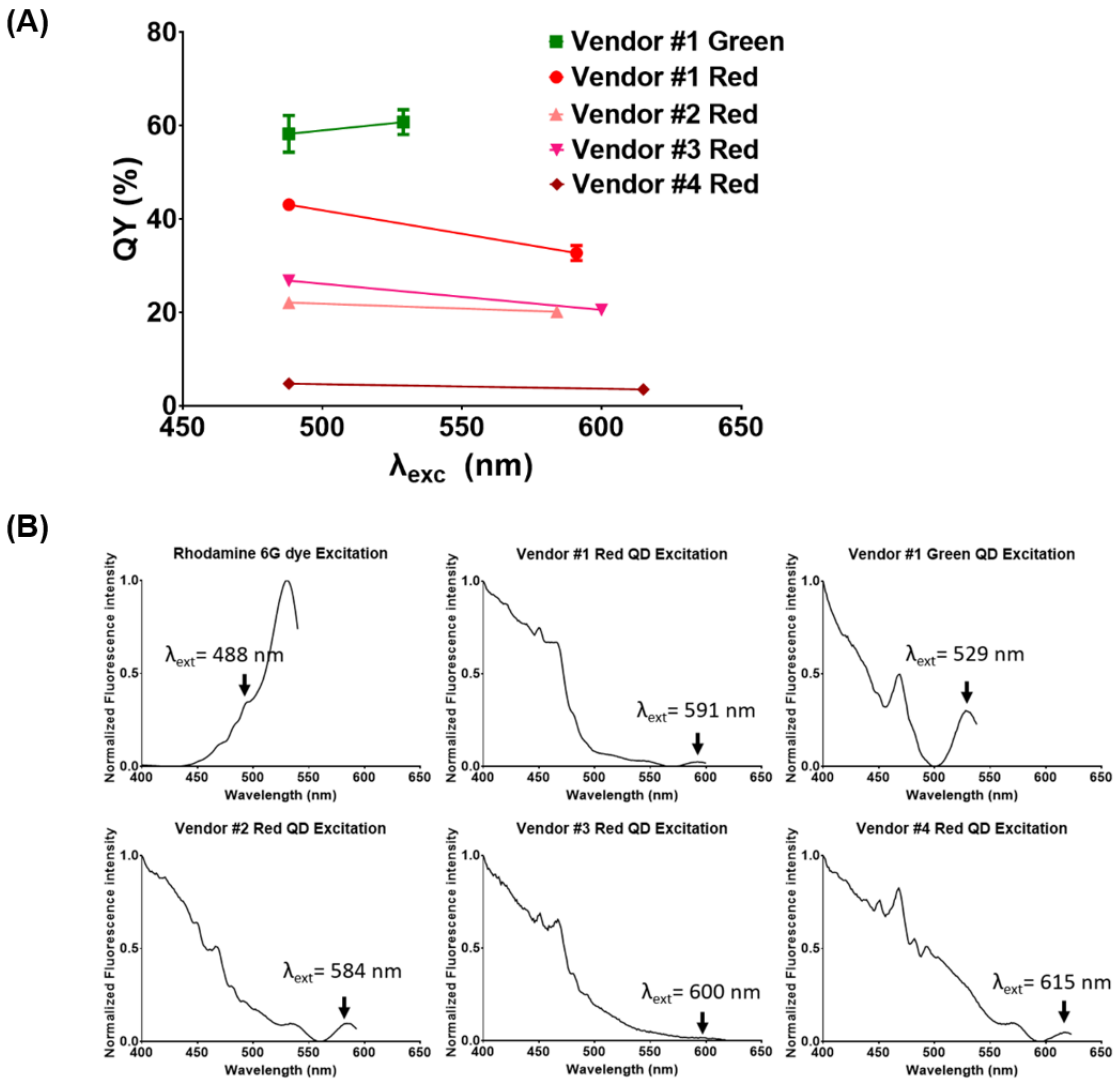

Figure 25 (a) Photoluminescence QY wavelength dependence for QDs from 4 vendors excited at 488 nm and at the first exciton wavelength. (b) Excitation spectra for Rhodamine 6G and QDs from 4 vendors.

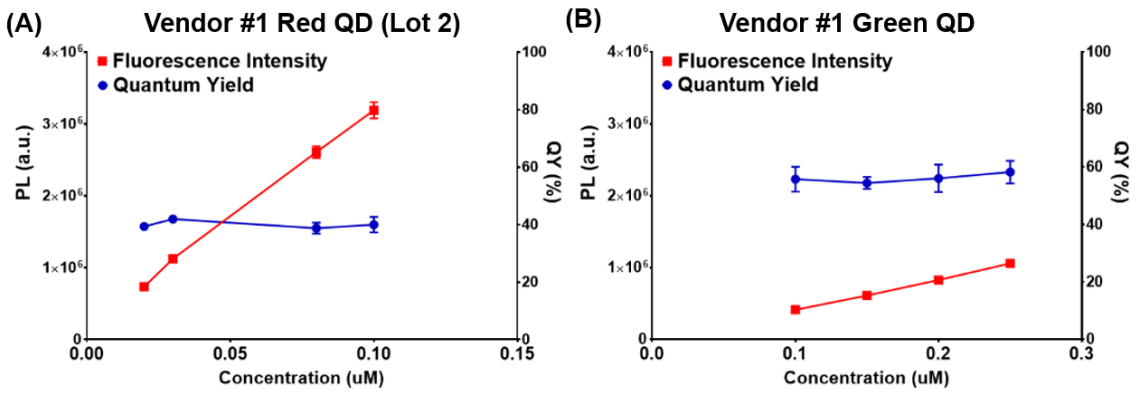

Figure 26 Photoluminescence intensity (PL) and QY of QDs from Vendor 1 as a function of diluted concentration: (A) red QDs, Lot 2 and (B) green QDs.

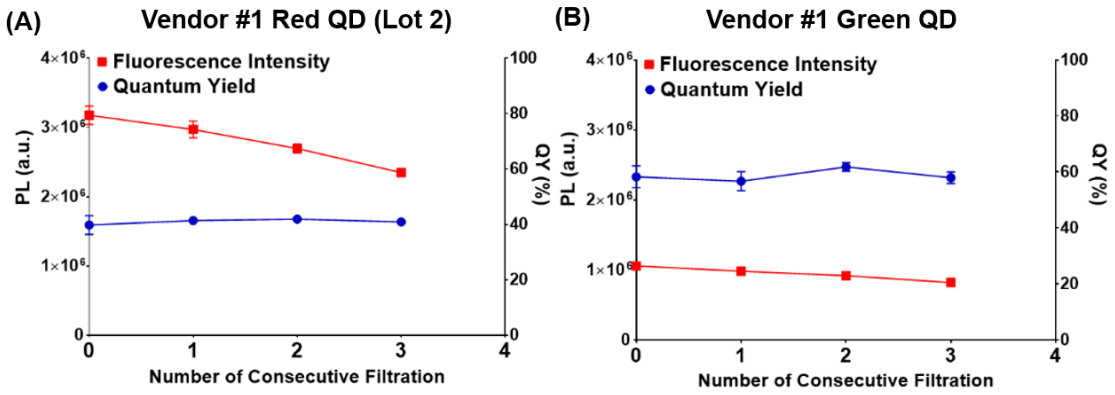

Figure 27 Photoluminescence (PL) intensity and QY of QDs from Vendor 1 after centrifugal filtration repeated up to 3 times (fixed concentration): (A) red QDs, lot 2, and (B) green QDs.

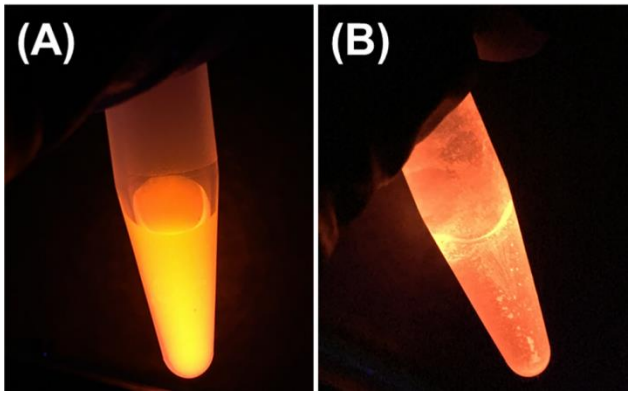

Figure 28 Representative images of QDs (0.1 µM) from Vendor #1 show substantial aggregation in pH 4.7, 0.1 M MES buffer. QDs from Vendor 1 (Lot 1) dispersed in (A) a compatible buffer (i.e., pH 9, 50 mM borate buffer) and (B) in an incompatible buffer (i.e., pH 4.7, 0.1 M MES buffer). QDs from Vendor #1, regardless of lot number or color, aggregated and precipitated in MES buffer.

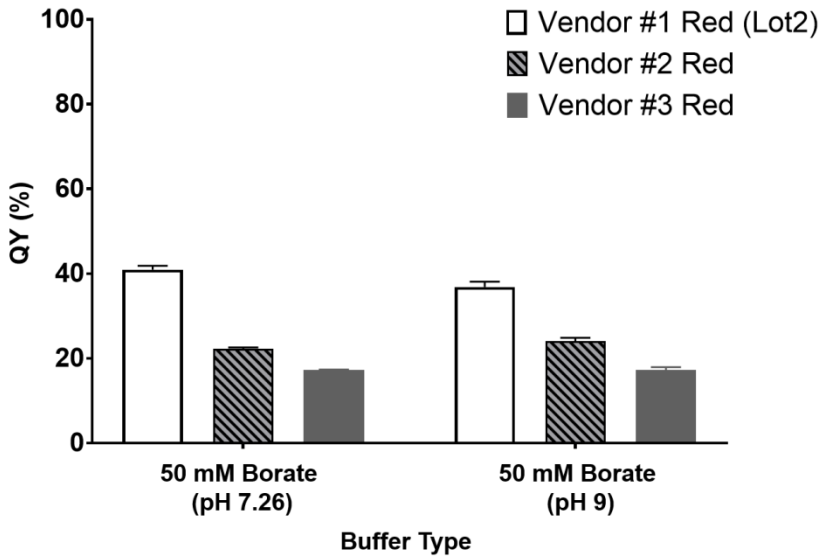

Figure 29 QY of QDs from Vendor 1 (Lot 2) (0.1 µM), Vendor 2 (0.1 µM), and Vendor 3 (0.15 µM) in pH 7.26 and pH 9, 50 mM borate buffer.

Appendix C

Chapter 4 Supplementary Information: Biomolecular Detection, Tracking, and Manipulation using a Magnetic Nanoparticle-Quantum Dot Platform

Supplementary Figures

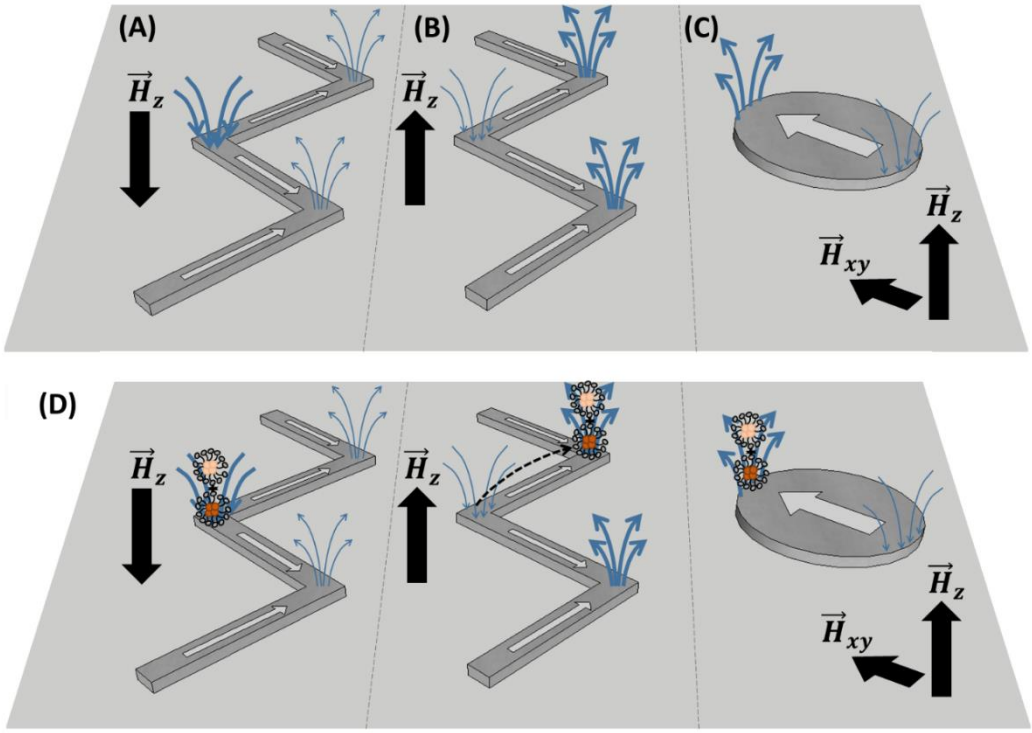

Figure 30 Illustration of magnetic zigzag wire and disk patterns used in trapping experiments. For zigzag wires (A) and (B), magnetic domains form along wire segments (light gray arrows), resulting in locations of strong magnetic fields at wire vertices (blue arrows). These localized fields (and resulting field gradients) act as traps for magnetic nanoparticles. Upon applying a field $\vec{H}_z$ perpendicular to the platform (indicated by black block arrows), the trap strength can be tuned. Relative trapping forces are indicated by the thickness of the blue arrows at wire vertices. (C) An in-plane applied field ($\vec{H}_{xy}$) creates a magnetic domain in a disk and trapping locations at opposite edges of the disk. This domain can be rotated by rotating $\vec{H}_{xy}$. In the presence of an out-of-plane applied field $\vec{H}_z$, the trap strengths can be tuned, as with the zigzag wires. (D) Schematic illustrating trapping and transport of micelle aggregates.

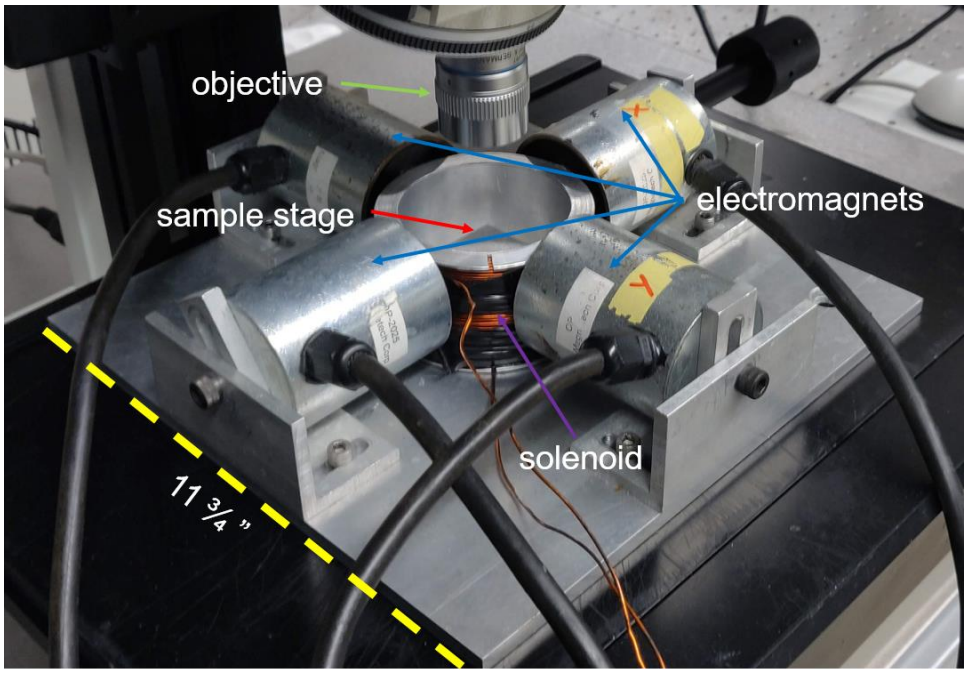

Figure 31 Typical electromagnet setup used for this experiment. Electromagnets produce in-plane magnetic field $\vec{H}_{xy}$ while the solenoid coil produces the out-of-plane field $\vec{H}_z$. These fields are tunable by adjusting the current (and current direction) through the electromagnets or solenoid.

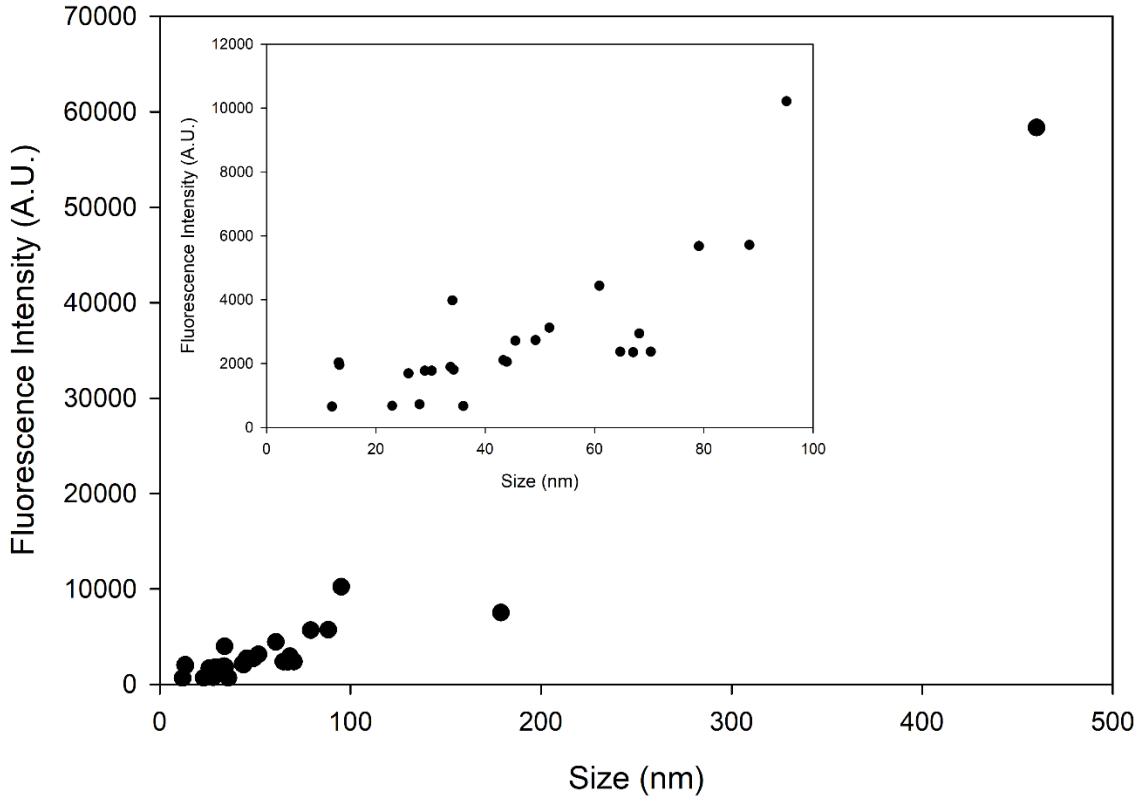

Figure 32 Single particle tracking (SPT) analysis of micelle "nanobrick" aggregate size (diameter) vs. total fluorescent intensity as measured by fluorescence microscopy. A positive correlation between fluorescent intensity and QD-micelle cluster diameter was evidenced. Because aggregate fluorescence intensity depends on the number of micelles in the aggregate, a volumetric, or r^3, correlation between intensity and size would be expected. Also, particle sizes were clustered in the 10-100 nm range (inset), with few large aggregates formed. [Note, the fluorescence intensity here does not correspond with that of Figure 12, as different gains were used to capture larger aggregates. Fluorescence intensity is therefore reported in arbitrary units. For each experiment, QD micelles in the absence of analyte were first observed to obtain a baseline signal and aggregates were measured with reference to this baseline.]

Appendix D

Chapter 5 Supplementary Information: Compact Quantum Dot Surface Modification to Enable Emergent Behaviors in Quantum Dot-DNA composites

Supplementary Methods and Discussion

PC3 Phase Transfer

Initially, we followed the protocol of Xu et al. in which precipitation and re-dissolution of QDs in pyridine was employed.[126] However, substantial losses were observed during phase transfer, attributed to incomplete dissolution of octadecylamine (ODA)-capped QDs in pyridine. ODA ligands have reduced affinity for pyridine compared to TOPO ligands originally employed in this protocol, which may hinder dissolution. The similarity of Hildebrandt solubility parameters ($\boldsymbol{\delta}$) for non-polar molecules is known to provide a reasonable estimate of their miscibility.[159] In this case, calculated $\boldsymbol{\delta}$ for TOPO (20 $J^{1/2}.cm^{-3/2}$), ODA (15 $J^{1/2}.cm^{-3/2}$), and pyridine (22 $J^{1/2}.cm^{-3/2}$) indicate higher miscibility of TOPO compared to ODA in pyridine. Thus, higher losses can be attributed to reduced solubility of ODA-QDs in pyridine during phase transfer. These observations indicate the importance of establishing ligand-solvent compatibility in phase transfer processes.

Carbodiimide Conjugation

ssDNA conjugation to PC3-QD -COOH groups was attempted via carbodiimide chemistry, the most commonly employed approach. However, carbodiimide chemistries manifest poor conjugation efficiencies (< 30%) that are highly sensitive to reaction conditions, including concentration, time, pH, and ratio of NH_2: COOH.[121,138,160] Therefore, reaction

conditions were first optimized using NH_2-terminated cyanine-5 (Cy-5) dye molecules and then translated to NH_2-terminated ssDNA molecules, which present larger steric and electrostatic considerations.

PC3-QDs were exchanged into 2-(N-morpholino)ethanesulfonic acid (MES, ThermoFisher Scientific Cat # 28390) buffer (0.1 M, pH 5) using a 7K MWCO Zeba spin column (Pierce, IL) according to manufacturer's protocol. PC3-QDs (70 µL, 2.5 µM) in MES were mixed with large excess of 1-Ethyl-3-(3-dimethylaminopropyl) carbodiimide (EDC, Thermo Fisher Scientific, catalog No. 77149) and sulfo-N-hydroxysuccinimide (sulfo-NHS, Thermo Fisher Scientific, catalog No. 24525) (EDC:sulfo-NHS:QD = 50,000:50,000:1, final EDC and sulfo-NHS concentration = 100 mM) and incubated for 25 minutes. Next, activated QDs were exchanged into PBS (0.1 M, pH 7.2) using a 40K MWCO Zeba spin column and mixed with NH_2-terminated Cy-5 dye (Customized from IDT DNA Technologies) (QD:dye = 1: 5000) and vortexed for 4 hours at room temperature. Excess Cy-5 dye was separated from Cy-5-QD conjugates using a 40K MWCO Zeba spin column equilibrated with PBS buffer (0.1 M, pH 7.2).

Although previous work reported successful conjugation of PC3-QDs to streptavidin[126], NH_2-terminated dye molecules failed to generate Cy-5-QD conjugates via the same protocol. This may be a consequence of the lower number of functional groups present in conjugates, just one for NH_2-dyes versus many for streptavidin. To increase reaction efficiency, we increased either the number of NH_2-terminated dye molecules (dye:QD ratio increased from 40:1 to 400:1) or the number of EDC molecules (EDC:QD increased from

3000:1 to 50000:1), achieving modest success via both approaches (Figure 33); however, the latter is less expensive and therefore preferred.

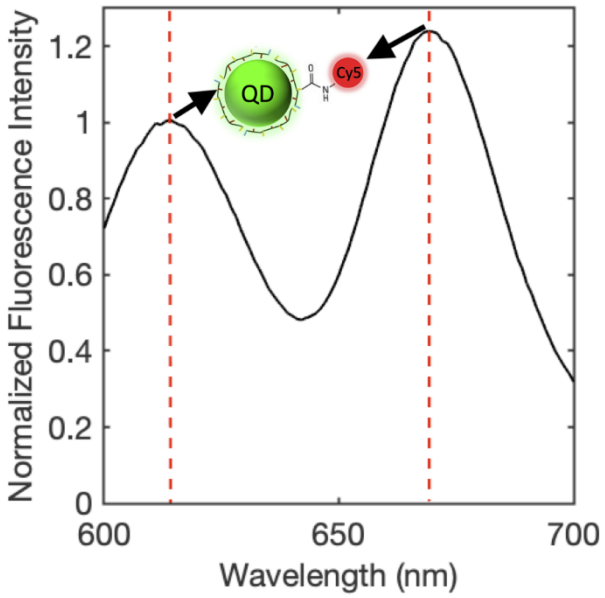

Figure 33 Fluorescence spectra of purified Cy-5-QD conjugates formed via carbodiimide chemistry at EDC:QD= 50000 (λ_{ex}: 580 nm; $\lambda_{em,QD}$: 615 nm, $\lambda_{em,ssDNA}$: 669 nm).

Next, we optimized several conjugation parameters (Table 6), identifying optimal reaction conditions of QD activation pH 5, EDC: sulfo-NHS: QD Ratio = 50000:50000:1, activated QD reaction concentration (2 µM), carbodiimide reaction time of 4 hours and, target : QD ratio= 5000 (used in sDBCO-QD conjugation). This optimized protocol was used to conjugate ssDNAs to PC3-QDs. However, fluorescence peaks corresponding to cy-5-ssDNA were not observed (not shown), indicating failure of the conjugation process. This may result from charge interactions. PC3 and ssDNAs can possess both positive and negative charges depending on pH, result from their -NH_2 and -COOH groups and -NH_2

and $–PO_4$ groups, respectively[138,160–162], although generally both molecules are negatively-charged. Thus, charge repulsion between PC3 and ssDNA or even between ssDNAs[163,164] would be expected. Further, ssDNA molecules are much larger than dye molecules employed (although similar to or smaller than streptavidin molecules previously employed[126]), thus steric considerations may play a role as well. To address these concerns, PC3 -COOH and $-NH_2$ groups were partially passivated with small poly(ethylene glycol) PEG molecules (MW = 2000, PEG-NH_2: Fisher Scientific Cat# NC1462405 and PEG-COOH: Cat# NC1504091) modified with $-NH_2$ and -COOH groups, respectively using the optimized carbodiimide chemistry to block charge at PEG:QD ratios = 100), and solution ionic strength was increased to 0.15-1.2 M. However, these attempts were unsuccessful.

Table 6 Carbodiimide reaction parameters optimized and effect on conjugation yield for the Cy-5 dye-NH_2 PC3-QD system.

Variable	Range	Effect on Conjugation Yield
Activation pH	4.7-5	↑ with ↑ pH
Reaction time	2-4 hrs	↑ with ↑ time
QD concentration	0.75-2 µM	↑ with ↑ concentration
EDC:sulfo-NHS:QD Ratio	3000:3000:1 to 10^5:10^5:1	50000:50000:1 worked best[a]
Dye:QD Ratio	15:1 to 500:1	↑ with ↑ ratio

[a]Precipitation was observed at the highest ratios (10^5:10^5:1).

ssDNA Conjugation to PC3-QDs using Click Chemistry

Initially, we attempted QD modification with dibenzocyclooctyne (DBCO), as reported previously[165,166] (Figure 34); however, decreased colloidal stability, resulting in QD precipitation, was observed at high DBCO conjugation efficiency. This most likely

originated from the hydrophobic nature of DBCO functional groups. Thus, DBCO was replaced with sDBCO, which is charged and therefore more hydrophilic. However, although colloidal stability was improved, it was still lower than desired at high conjugation yields, possibly as a result of non-specific charge interactions arising from the charged sulfo- groups. Stability was easily restored by addition of high molecular weight PEG molecules (MW 20 kDa) that enabled long-range repulsive depletion stabilization.[167] Alternatively, stability could also be improved by decreasing the sDBCO:QD ratio or by replacing the alkyne functionality on QDs with N_3.

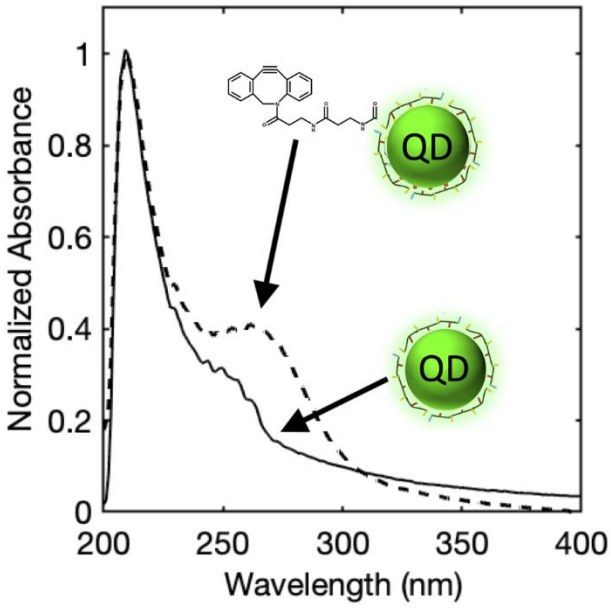

Figure 34 Absorbance spectra of PC3-QDs (solid) and DBCO-PC3-QDs (--) formed via carbodiimide chemistry (DBCO peak = ~260 nm).

Supplementary Calculations

Theoretical quenching efficiency calculation

Quenching efficiency (E) via FRET (i.e., Förster resonance energy transfer) mechanism was calculated as follows:

$$\boldsymbol{E} = \frac{\boldsymbol{R_o^6}}{\boldsymbol{s^6 + R_o^6}} \quad \text{Equation D.1}$$

where $\boldsymbol{R_o}$ is the Förster radius and d is the interparticle spacing.

$\boldsymbol{R_o}$ was calculated as follows:

$$\boldsymbol{R_o = 0.211 \times [\kappa^2 \emptyset_{QD} \eta^{-4} J(\lambda)]^{1/6}} \quad \text{Equation D.2}$$

where $\boldsymbol{\kappa^2}$ is relative orientation of transition dipoles of the donor and acceptor (assumed 2/3 as an average of randomly fluctuating dipoles), $\boldsymbol{\emptyset_{QD}}$ is QD quantum yield (measured at 0.17 for QDs with $\boldsymbol{\lambda_{em} = 540}$ nm), $\boldsymbol{\eta}$ is the medium refractive index (i.e., 1.33) and $\boldsymbol{J(\lambda)}$ is the calculated spectral overlap integral of donor fluorescence spectra and acceptor absorbance spectra ($\boldsymbol{1.34 \times 10^{19}}$ $M^{-1}.cm^{-1}.nm^4$).[168] The calculated $\boldsymbol{R_o}$ was 16.6 nm. Interparticle spacing(s) was calculated as follows:

$$\boldsymbol{s = L_{DNA} + L_{PC3} + L_{C6}} \text{ Equation D.3}$$

where $\boldsymbol{L_{DNA}}$ is the DNA length, (i.e., for 16 bp DNA, $\boldsymbol{16 \times 0.33\ nm = 5.33\ nm}$), $\boldsymbol{L_{PC3}}$ is the thickness of the PC3 coating, 0.9 nm, and $\boldsymbol{L_{C6}}$ is the calculated size of the C6 linker, 0.5 nm. Therefore, $\boldsymbol{s = 6.7\ nm}$. Plugging s and R_o into Equation 1 gives E = 0.99.

Additional Supplementary Figures

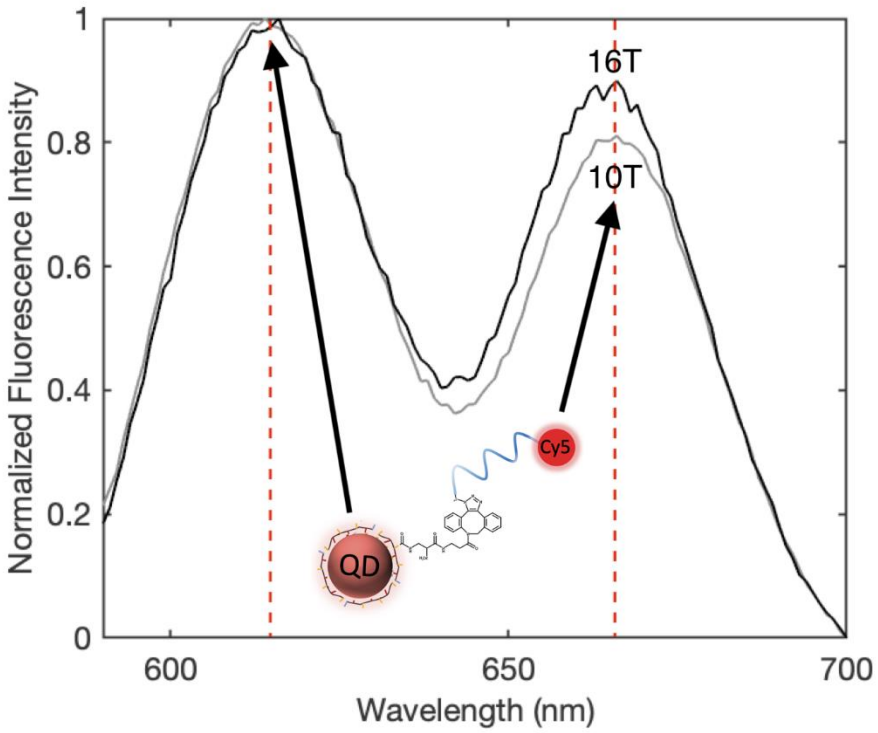

Figure 35 Fluorescence spectra of ssDNA-QDs formed via click chemistry using red QDs (λ_{em} = 618 nm) and poly-T ssDNA of different lengths: T_{16} (solid) and T_{10} (grey). ssDNA was terminated with Cy-5 reporter dyes to enable detection. (λ_{ex} = 580 nm, QDs: λ_{em} = 618 nm, Cy5-ssDNA: λ_{em} = 664 nm).

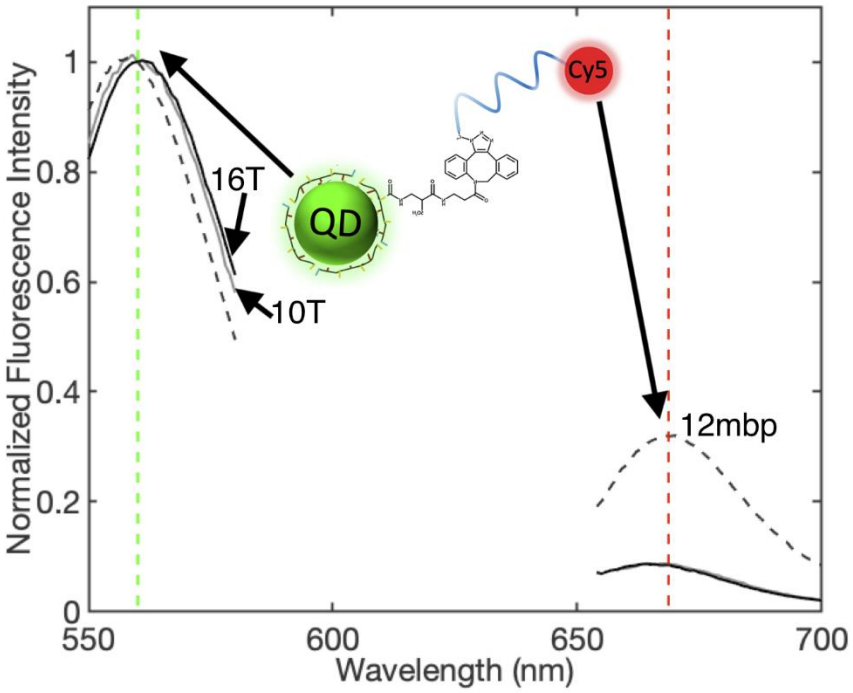

Figure 36 Fluorescence spectra of ssDNA-QDs formed via click chemistry using green QDs (λ_{em} = 560 nm) and ssDNAs of different lengths and sequences: T_{16} (solid), T_{10} (grey) and 12mbp (grey-dashed). ssDNA was terminated with Cy-5 reporter dyes to enable detection. (QDs: λ_{ex} = 350 nm, λ_{em} = 561 nm, Cy5-ssDNA: λ_{ex} = 649 nm, λ_{em} = 664 nm).

References

159. Barton, A. F. M. *CRC handbook of solubility parameters and other cohesion parameters*.
160. Wu, C.-S., Cupps, J. M. & Fan, X. Compact quantum dot probes for rapid and sensitive DNA detection using highly efficient fluorescence resonant energy transfer. *Nanotechnology* **20**, 305502 (2009).
161. Zhou, D. *et al.* A compact functional quantum dot-DNA conjugate: Preparation, hybridization, and specific label-free DNA detection. *Langmuir* **24**, 1659–1664 (2008).
162. Wu, J., Wang, H., Zhu, A. & Long, F. Adsorption Kinetics of Single-Stranded DNA on Functional Silica Surfaces and Its Influence Factors: An Evanescent-Wave Biosensor Study. *ACS Omega* **3**, 5605–5614 (2018).

163. Lee, J., Choi , Y., Kim, J., Park, E. & Song, R. Positively Charged Compact Quantum Dot-DNA Complexes for Detection of Nucleic Acids. *ChemPhysChem* **10**, 806–811 (2009).
164. Sedighi, A. & Krull, U. J. Rapid Immobilization of Oligonucleotides at High Density on Semiconductor Quantum Dots and Gold Nanoparticles. *Langmuir* **32**, 13500–13509 (2016).
165. Dommerholt, J., Rutjes, F. P. J. T. & van Delft, F. L. Strain-Promoted 1,3-Dipolar Cycloaddition of Cycloalkynes and Organic Azides. *Top. Curr. Chem.* **374**, 20–40 (2016).
166. Hao, J., Huang, L. L., Zhang, R., Wang, H. Z. & Xie, H. Y. A mild and reliable method to label enveloped virus with quantum dots by copper-free click chemistry. *Anal. Chem.* **84**, 8364–8370 (2012).
167. Zhang, X., Servos, M. R. & Liu, J. Instantaneous and quantitative functionalization of gold nanoparticles with thiolated DNA using a pH-assisted and surfactant-free route. *J. Am. Chem. Soc.* **134**, 7266–7269 (2012).
168. Lakowicz, J. R. *Principles of Fluorescence Spectroscopy*. (2005).

Appendix E

Chapter 4 Supplementary Videos: Biomolecular Detection, Tracking, and Manipulation using a Magnetic Nanoparticle-Quantum Dot Platform

Supplementary Videos

Supplementary videos are reproduced from K. D. Mahajan, G. Ruan, G. Vieira, T. Porter, J. J. Chalmers, R. Sooryakumar and J. O. Winter, *J. Mater. Chem. B*, 2020, Advance Article, https://doi.org/10.1039/C9TB02481F with permission from The Royal Society of Chemistry. The videos may be accessed using the following link: https://kb.osu.edu/handle/1811/91555.

Descriptions:

Supplementary Video 1: Nanoassembly transport around a microdisc. Control is demonstrated by magnetic trapping of the nanoassembly. A reverse motion around the disk is shown from 11-16 seconds, and then the particle continues its clockwise trajectory. After 33 seconds the nanoassembly is released from the microdisc.

Supplementary Video 2: Nanoassembly transport on nanowires via vertex-to-vertex hopping.

Supplementary Video 3: Simultaneous magnetic transport of red protein (avidin) and green DNA (p53 ssDNA) nanoassemblies via vertex to vertex hopping on magnetic nanowire arrays.

Supplementary Video 4: Red, magnetic protein nanoassemblies (i.e., avidin as the molecular target, containing SPIONs) are trapped and transported from vertex-to-vertex,

whereas green, non-magnetic DNA nanoassemblies (p53 ssDNA as the molecular target, containing no SPIONs) are not trapped and display motion resulting from Brownian motion or liquid flow.

Supplementary Video 5: Following addition of DNA-targeting SPION micelles, green, magnetic DNA nanoassemblies (p53 ssDNA as the molecular target, containing QDs and SPIONs) are transported, showing rapid conjugation of SPIONs to green micelle structures.